

POLITECNICO DI MILANO

Facoltà di Ingegneria dei Sistemi
Corso di Studio in Ingegneria Biomedica



EVALUATION OF STEREO-PHOTOGRAMMETRY TO ASSESS FULL-FIELD VESSEL STRAIN MEASUREMENTS FOLLOWING STENT IMPLANTATION

Relatore: Prof. Francesco Migliavacca

Correlatore: Dr. Andrew James Narracott

Autori:

Francesca Colombo matricola 765766

Sandra Buzzago matricola 765448

Anno Accademico 2011/2012

Index

Index	2
Indice delle figure	6
Indice delle tabelle	6
Indice dei grafici	6
List of figures	7
List of tables	11
List of graphs	13
Abstract	15
Sommario	16
Summary	29
Introduction	41
1. Stenting methodology and problems	41
2. Analyses techniques	42
3. Report structure	45
State of the art	46
1. Photogrammetry	46
2. Image registration and Digital Image Correlation	50
3. Virtual methods	52
3.1 ANSYS	52
3.2 Realsoft 3D	52
4. Current project	54
4.1 Description and aims	54

Materials and methods.....	56
1. Evaluation process.....	56
2. Geometric models.....	59
2.1 Strip	59
2.2 Vessel	59
2.3 Stent.....	61
2.4 Balloon	62
3. Material models	62
3.1 Isotropic linear elastic.....	63
3.2 Isotropic hyperelastic.....	63
4. Camera set-up.....	64
5. Calibration	67
6. Reconstruction.....	72
7. Image registration.....	74
8. Strain measurement	76
8.1 Engineering and true strain.....	76
8.2 Global strain	78
8.3 Green-Lagrange tensor	79
9. Strip test protocol	81
9.1 Simulations	81
9.2 Noise Test.....	82
9.3 Resolution Test.....	83
9.4 Global strain	83
9.5 Reconstruction and image registration	85
10. Vessel test protocol.....	86
10.1 Simulations	86

10.2 Expected strain	87
10.3 Mesh sensitivity test	89
10.4 Reconstruction and image registration	90
11. Stented vessel test protocol	91
11.1 Simulations	91
11.2 Bending Problem	92
11.3 Mesh sensitivity test	93
11.4 Strain distribution	94
11.5 Symmetry	95
11.6 Reconstruction and image registration	95
Results	97
1. Strip	97
1.1 Preliminary tests	97
1.2 Reconstruction and image registration	103
2. Vessel	110
2.1 Preliminary tests	110
2.2 Reconstruction and image registration	113
3. Stented vessel	121
3.1 Preliminary tests	121
3.2 Reconstruction and image registration	129
Discussion.....	135
1. Strip	135
1.1 Noise.....	135
1.2 Resolution test	136
1.3 Global strain	137
1.4 Reconstruction and image registration	138

2. Vessel	143
2.1 Expected values	143
2.2 Mesh sensitivity	144
2.3 Reconstruction and image registration	145
3. Stented vessel	149
3.1 Bending problem	149
3.2 Mesh sensitivity	149
3.3 Strain distribution	150
3.4 Reconstruction and image registration	150
Conclusions	153
Potential error sources	159
Future work	161
Appendix A	164
1. Error values	164
Appendix B.....	165
1. Noise test	165
2. Resolution test	167
3. Global strain	168
4. Reconstruction and image registration	169
Appendix C.....	174
1. Reconstruction and image registration	174
Appendix D	177
1. Reconstruction and image registration	177
Acknowledgements	178
Bibliography	180

Indice delle figure

Figura 1 Modelli geometrici utilizzati nelle analisi.....	17
Figura 2 Ambiente virtuale realizzato con il software Realsoft3D	18
Figura 3 Distribuzione della deformazione circonferenziale sulla superficie del vaso, dopo completa espansione dello stent	24

Indice delle tabelle

Tabella 1 Modelli di Materiale utilizzati nelle analisi.....	19
--	----

Indice dei grafici

Grafico 1 Errore sulla deformazione della striscia calcolato tra i dati estratti dai test e quelli derivanti da ANSYS in direzione trasversale e longitudinale	22
Grafico 2 Confronto tra i valori di deformazione circonferenziale calcolati senza e tenendo in considerazione le non linearità	23
Grafico 3 Errore sulla deformazione del vaso calcolato tra i dati estratti dai test e quelli derivanti da ANSYS in direzione assiale e circonferenziale	24
Grafico 4 Errore sulla deformazione del vaso stentato calcolato tra i dati estratti dai test e quelli derivanti da ANSYS in direzione assiale e circonferenziale.....	25

List of figures

Figure 1 Geometry models used in the analyses	30
Figure 2 Virtual environment in Realsoft3D.....	31
Figure 3 Circumferential strain distribution on the vessel surface, after complete stent expansion.....	37
Figure 4 Stereovision set-up.....	47
Figure 5 Strain measurement of an elastic sheet	49
Figure 6 ANSYS is a finite element analysis package used to define a virtual object, apply a simulated force and calculate the strain.....	52
Figure 7 Realsoft 3D is a modelling and ray tracing program allowing specification of virtual cameras, modelling of virtual object and rendering of a scene from each camera. .	53
Figure 8 Process to evaluate the stereoscopic strain measurement technique.....	58
Figure 9 Strip geometry.....	59
Figure 10 Vessel thickness measurement set-up.....	60
Figure 11 VIEW screenshot	60
Figure 12 Stent dimensions: length, inner and outer diameters	62
Figure 13 Parameters of a single lens optical system.....	64
Figure 14 Realsoft 3D stereo camera set-up.....	65
Figure 15 Translation (T) and rotation vector (R) linked two different frames	67
Figure 16 Camera aiming to a point in the space	68
Figure 17 Possible translations and rotations of the checkerboards in the 3D space	70
Figure 18 Calibration checkerboards.....	70
Figure 19 Extrinsic parameters image from Calibration Toolbox	71
Figure 20 Triangulations processes based on the stereoscopic vision and photogrammetry theory.....	73
Figure 21 a) green grid points shown on undeformed (fixed) image b) red grid points shown in deformed (registered) image c) combined intensities of fixed (green) and registered (red) images	75
Figure 22 Example of grids overlapped with fixed and registered images after failed registration.....	75

Figure 23 Triplet of points.....	77
Figure 24 Configuration of vectors to obtain the normal and the tangent lines to the triangular surface.	80
Figure 25 Flowchart illustrating Strip test protocol	81
Figure 26 First and last tensile test step.....	82
Figure 27 Central points picked for the noise test.....	82
Figure 28 Two column reconstructed for global strain test.....	84
Figure 29 Graphical illustration of method 1 and 2 for Global strain evaluation	84
Figure 30 Simulation and test protocol on the vessel.....	86
Figure 31 Cylinder used to modelling the vessel in the simulation procedure.....	87
Figure 32 Stress components acting on a infinitesimal portion of vessel	88
Figure 33 Left and right camera views of cylinder in Realsoft 3D showing region that can be reconstructed.	90
Figure 34 Simulation and test on the Stented vessel	91
Figure 35 Realization of Stented vessel geometry step by step: the first panel shows the balloon surface, in the second there is the contact between the balloon and the stent and finally, in third one, balloon, stent and vessel are presented together.	92
Figure 36 Half vessel and stent model used to do faster mesh analysis.....	94
Figure 37 Location of circumferential rings used to assess symmetry of strain distribution within the stented region (Ring 1 – Ring 9) and in the unstented region (un_Ring1 – un_Ring3).....	94
Figure 38 Left and right camera views of Stented vessel geometry in Realsoft 3D showing region that can be reconstructed.	96
Figure 39 ANSYS longitudinal strain	101
Figure 40 Transversal strain results (direction shown by arrow) for test 1: a) ANSYS strain; b) - d) reconstruction results; e) – g) image registration results; b) and e) Green strain; c) and f) Local strain; d) and g) Global strain.	104
Figure 41 Longitudinal strain results (direction shown by arrow) for test 1: a) ANSYS strain; b) - d) reconstruction results; e) – g) image registration results; b) and e) Green strain; c) and f) Local strain; d) and g) Global strain.	104

Figure 42 Transversal strain results (direction shown by arrow) for test 2: a) ANSYS strain; b) - d) reconstruction results; e) – g) image registration results; b) and e) Green strain; c) and f) Local strain; d) and g) Global strain 105

Figure 43 Longitudinal strain results (direction shown by arrow) for test 2: a) ANSYS strain; b) - d) reconstruction results; e) – g) image registration results; b) and e) Green strain; c) and f) Local strain; d) and g) Global strain. 105

Figure 44 Transversal strain results (direction shown by arrow) for test 3: a) ANSYS strain; b) - d) reconstruction results; e) – g) image registration results; b) and e) Green strain; c) and f) Local strain; d) and g) Global strain. 106

Figure 45 Longitudinal strain results (direction shown by arrow) for test 3: a) ANSYS strain; b) - d) reconstruction results; e) – g) image registration results; b) and e) Green strain; c) and f) Local strain; d) and g) Global strain. 106

Figure 46 Transversal strain results (direction shown by arrow) for test 4: a) ANSYS strain; b) - d) reconstruction results; e) – g) image registration results; b) and e) Green strain; c) and f) Local strain; d) and g) Global strain. 107

Figure 47 Longitudinal strain results (direction shown by arrow) for test 4: a) ANSYS strain; b) - d) reconstruction results; e) – g) image registration results; b) and e) Green strain; c) and f) Local strain; d) and g) Global strain. 107

Figure 48 Circumferential strain results (direction shown by arrow) for test 1: a) ANSYS strain; b) and c) reconstruction results; d) and e) image registration results; b) and d) Green strain; c) and e) Local strain. 115

Figure 49 Axial strain results (direction shown by arrow) for test 1: a) ANSYS strain; b) and c) reconstruction results; d) and e) image registration results; b) and d) Green strain; c) and e) Local strain. 115

Figure 50 Circumferential strain results (direction shown by arrow) for test 2: a) ANSYS strain; b) and c) reconstruction results; d) and e) image registration results; b) and d) Green strain; c) and e) Local strain. 116

Figure 51 Axial strain results (direction shown by arrow) for test 2: a) ANSYS strain; b) and c) reconstruction results; d) and e) image registration results; b) and d) Green strain; c) and e) Local strain. 116

Figure 52 Circumferential strain results (direction shown by arrow) for test 3: a) ANSYS strain; b) and c) reconstruction results; d) and e) image registration results; b) and d) Green strain; c) and e) Local strain.	117
Figure 53 Axial strain results (direction shown by arrow) for test 3: a) ANSYS strain; b) and c) reconstruction results; d) and e) image registration results; b) and d) Green strain; c) and e) Local strain.	117
Figure 54 Circumferential strain results (direction shown by arrow) for test 4: a) ANSYS strain; b) and c) reconstruction results; d) and e) image registration results; b) and d) Green strain; c) and e) Local strain.	118
Figure 55 Axial strain results (direction shown by arrow) for test 4: a) ANSYS strain; b) and c) reconstruction results; d) and e) image registration results; b) and d) Green strain; c) and e) Local strain.	118
Figure 56 ANSYS circumferential strain on the entire geometry and selected patch.	129
Figure 57 Circumferential strain results (direction shown by arrow) for test 1: a) ANSYS strain; b) and c) reconstruction results; d) and e) image registration results; b) and d) Green strain; c) and e) Local strain.	130
Figure 58 Axial strain results (direction shown by arrow) for test 1: a) ANSYS strain; b) and c) reconstruction results; d) and e) image registration results; b) and d) Green strain; c) and e) Local strain.	131
Figure 59 Potential sources of error flowchart	160

List of tables

Table 1 Material models	32
Table 2 Geometry configuration tested	59
Table 3 Measurement tests of thickness and the diameter of the vessel	61
Table 4 Vessel geometry dimensions	61
Table 5 Stent bilinear isotropic hardening material parameters	62
Table 6 Linear elastic material properties	63
Table 7 Hyperelastic material properties.....	64
Table 8 Applied parameters of stereo set-ups camera.....	66
Table 9 Light source project specifications	66
Table 10 Checkerboard sets' features	69
Table 11 Calibrations realized.....	71
Table 12 Protocol code	82
Table 13 Protocol code	83
Table 14 Protocol code	83
Table 15 Protocol code	85
Table 16 Protocol code	85
Table 17 Protocol code	87
Table 18 Protocol code	89
Table 19 First stage mesh refinement in radial and circumferential direction; second stage mesh refinement in axial direction	90
Table 20 Protocol code	90
Table 21 Protocol code	93
Table 22 First stage mesh refinement in radial and circumferential direction; second stage mesh refinement in axial direction	93
Table 23 Protocol code	94
Table 24 Protocol code	95
Table 25 Axial location of the nine rings analyzed in the symmetry test	95
Table 26 Protocol code	95

Table 27 Absolute and percentage error on the strain after applying a random error on the position	99
Table 28 Summary of Strip geometry tests	103
Table 29 Summary of Vessel geometry tests	113
Table 30 Protocol code	129
Table 31 Percentage error on strain at middle step of deformation for noise test.....	165
Table 32 Percentage error on strain at final step of deformation for noise test.....	166
Table 33 Absolute error on strain at middle step of deformation for noise test.....	166
Table 34 Absolute error on strain at final step of deformation for noise test.....	167
Table 35 Absolute error on strain for resolution test.....	167
Table 36 Percentage error on strain for resolution test.....	168
Table 37 Absolute error on longitudinal strain for the Global strain test.....	168
Table 38 Percentage error on longitudinal strain for the Global strain test.....	169
Table 39 Summary of the tests conducted on the Strip geometry	169
Table 40 Absolute error on transversal strain for test 1	170
Table 41 Absolute error on longitudinal strain for test 1	170
Table 42 Absolute error on transversal strain for test 2	171
Table 43 Absolute error on longitudinal strain for test 2	171
Table 44 Absolute error on transversal strain for test 3	172
Table 45 Absolute error on longitudinal strain for test 3	172
Table 46 Absolute error on transversal strain for test 4	173
Table 47 Absolute error on longitudinal strain for test 4	173
Table 48 Summary of the tests conducted on the Vessel geometry	174
Table 49 Absolute error on circumferential and axial strain for test 1.....	175
Table 50 Absolute error on circumferential and axial strain for test 2.....	175
Table 51 Absolute error on circumferential and axial strain for test 3.....	176
Table 52 Absolute error on circumferential and axial strain for test 4.....	176
Table 53 Protocol code	177
Table 54 Absolute error on circumferential and axial strain for Stented vessel test.....	177

List of graphs

Graph 1 Error on strain on the strip between test data and ANSYS reported data in transversal and longitudinal direction.	34
Graph 2 Error on strain on the vessel between test data and ANSYS reported data in axial and circumferential direction.....	36
Graph 3 Comparison between circumferential strains obtain with and without taking into account non-linear effects.....	36
Graph 4 Error on strain on the stented vessel between test data and ANSYS reported data in axial and circumferential direction.	37
Graph 5 Displacement against initial position.....	79
Graph 6 Strain results after random noise applied to position data: a-d) longitudinal strain; e-h) transverse strain; a,b,e,f) Local strain measure; c,d,g,h) Green strain measure; a,c,e,g) middle stage of deformation; b,d,f,h) final stage of deformation.....	99
Graph 7 Transversal strain at a) middle step and b) final step	100
Graph 8 Longitudinal strain at a) middle step and b) final step	100
Graph 9 a) Absolute error on transversal strain b) Absolute error on longitudinal strain.	101
Graph 10 Longitudinal ANSYS strain and Global strain calculated with the four methods	102
Graph 11 Absolute error on longitudinal strain a) at middle step b) at final step.	102
Graph 12 Error on transversal strain: a) test data vs. ANSYS reported data; b) test data vs. ANSYS derived data; c) ANSYS derived data vs. ANSYS reported data.....	109
Graph 13 Error on longitudinal strain: a) test data vs. ANSYS reported data; b) test data vs. ANSYS derived data; c) ANSYS derived data vs. ANSYS reported data.....	109
Graph 14 a) Variation in applied pressure with analysis time. Variation of strain results with applied pressure: b) radial strain; c) circumferential strain; d) axial strain.	111
Graph 15 ANSYS circumferential strain against theta coordinate. The strain is plotted for each one of the four meshes with different numbers of elements in the circumferential and radial direction.....	112
Graph 16 ANSYS hoop strain against theta coordinate. The strain is plotted at different mesh refinements in the axial direction.....	113

Graph 17 Error on circumferential strain: a) test data vs. ANSYS reported data; b) test data vs. ANSYS derived data; c) ANSYS derived data vs. ANSYS reported data.	120
Graph 18 Error on axial strain: a) test data vs. ANSYS reported data; b) test data vs. ANSYS derived data; c) ANSYS derived data vs. ANSYS reported data.....	120
Graph 19 Comparison between enhanced strain and default element formulation a) ANSYS radial displacement b) ANSYS hoop strain	121
Graph 20 ANSYS hoop strain against theta coordinate. The strain is plotted for each one of the four meshes with different numbers of elements in the circumferential and radial direction.....	123
Graph 21 Mean error on ANSYS hoop strain between each mesh and the reference mesh D. Axis x represents mesh type: 1=A, 2=B, 3=C, 4=D.....	123
Graph 22 Absolute error between ANSYS hoop strains computed with: a) mesh D and mesh A; b) mesh D and mesh B; c) mesh D and mesh C; d) mesh D and mesh D.....	124
Graph 23 ANSYS hoop strain against theta coordinate. The strain is plotted for each one of the four meshes with an increasing number of elements in the axial direction.....	125
Graph 24 Absolute error between ANSYS hoop strain calculated with: a) mesh C3 and mesh C1; b) mesh C3 and mesh C2.....	125
Graph 25 Hoop strain plots against theta coordinate on different rings at different simulation substeps.....	126
Graph 26 Variation in hoop strain distribution along z direction.....	127
Graph 27 Circumferential strain comparison between correspondent axial locations.	128
Graph 28 Error on circumferential strain: a) test data vs. ANSYS reported data; b) test data vs. ANSYS derived data; c) ANSYS derived data vs. ANSYS reported data.	133
Graph 29 Error on axial strain: a) test data vs. ANSYS reported data; b) test data vs. ANSYS derived data; c) ANSYS derived data vs. ANSYS reported data.....	133

Abstract

This work aimed to determine the accuracy of a stereo-photogrammetric technique for the full-field strain measurement employed in *in-vitro* analyses on stented vessels. To investigate the optical system an evaluation process based on a virtual reality environment was developed. The softwares and the support for this study were provided by the Department of Cardiovascular Science of the University of Sheffield.

The evaluation procedure consisted of several steps involving the use of the finite element software ANSYS Mechanical, a modelling application capable of simulating physical objects (Realsoft 3D), different Matlab toolboxes and finally an image registration toolkit developed by the University of Sheffield called ShIRT. A virtual stereo-camera rig was reproduce using these softwares and the 2D images of the object of interest were captured by each camera. Then nodal coordinates of the surface were extracted employing the manual reconstruction or the image registration method and the strain distribution was derived. Finally the values of strain were compared to the data computed by ANSYS to assess the goodness of the measurement.

To obtain a complete characterisation of the system a 2D strip, a 3D vessel and a 3D stented vessel geometries were defined and the material properties were varied to quantify the sensitivity to different tissue behaviour. Some preliminary tests were performed to examine the influence of the system parameters on the strain measure and fix the principle tests' features.

The results showed an error on strain of less than 0.01 in case of simple geometry. More complex geometries were affected by errors of the order of 0.02 which suggest a reliable accuracy for large deformation application. The tests also demonstrated that the image registration improved the strain agreement. The evaluation method has confirmed as an effective and convenient technique which can be predict the accuracy of photogrammetric strain measurements in advance. This application is a powerful tool for the *in-vitro* approach to reduce the effort in terms of time and funds, and could be used both in the academic and industrial research field.

Sommario

I. INTRODUZIONE

Le malattie coronariche sono universalmente riconosciute come la causa di morte più frequente sia nei paesi sviluppati che in quelli in via di sviluppo. Responsabile dell'occlusione di una o più arterie coronariche è nella quasi totalità dei casi la formazione di una placca aterosclerotica [1] che comporta la riduzione del flusso ematico. Nel 1985 Palmaz e colleghi proposero, come soluzione a questo problema, l'utilizzo di un palloncino montato su uno stent per mantenere pervio il lume del vaso interessato. Questi stent intravascolari hanno una struttura cilindrica di piccolo calibro e hanno lo scopo di ripristinare la perfusione sanguigna fisiologica dei tessuti sottostanti una volta espansi [2]. Attualmente, l'impianto di stent è una procedura comune avente un alto tasso di successo se comparata con il solo intervento di angioplastica [3]. Tuttavia sono presenti degli svantaggi: per esempio, durante l'espansione lo stent interagisce con l'arteria provocando sforzi e deformazioni alla parete vascolare. A questo fenomeno è associata un'eccessiva

proliferazione del tessuto vascolare conosciuta come *in-stent* restenosi [4].

La consapevolezza che la riuscita dell'impianto è legata al design dello stent, e quindi all'interazione dello stesso con la parete vascolare, ha incoraggiato la ricerca a focalizzarsi sugli sforzi e le deformazioni che si generano durante l'espansione del dispositivo. Per affrontare queste problematiche sono stati condotti sia esperimenti *in-vitro* che computazionali.

In particolare, negli ultimi anni, diverse analisi strutturali computazionali sono state utilizzate per studiare la risposta della parete vascolare all'angioplastica e all'impianto di stent ([5]; [6]; [7]; [8]). Le analisi sperimentali *in-vitro* includono tecniche di misurazione ottica che utilizzano una o più telecamere per acquisire immagini 2D, che successivamente vengono ricostruite come superfici tridimensionali. Questa tecnica è stata utilizzata dal dipartimento di *Cardiovascular Science* dell'università di Sheffield ([9]; [10]).

Il lavoro svolto vuole essere la continuazione di questi studi precedenti, focalizzandosi in particolare sulla validazione di un metodo stereoscopico per la misura della deformazione dei vasi in seguito a impianto di stent. Per

quantificare l'incertezza associata ad un sistema stereoscopico sperimentale, sono stati eseguiti degli esperimenti in un ambiente virtuale usando un set-up di telecamere simile a quello utilizzato in esperimenti di laboratorio e i dati estrapolati sono stati confrontati con quelli ricavati da simulazioni agli elementi finiti (ANSYS Mechanical). Questo processo è stato applicato su tre geometrie che gradualmente si avvicinavano al modello desiderato: una striscia 2D, un vaso 3D ed infine un vaso 3D in cui è stato espanso uno stent. Le proprietà del materiale sono state variate in modo da quantificare la sensibilità del sistema a differenti comportamenti del tessuto. I risultati dello studio mirano a determinare l'accuratezza della tecnica, indipendentemente dalla sorgente di errore sperimentale, per esempio distorsione delle lenti o rifrazione. Questo procedimento può essere poi impiegato per valutare metodi di analisi delle deformazioni delle superfici e per definire delle specifiche per future applicazioni sperimentali. La possibilità di utilizzare un ambiente virtuale per eseguire dei test ha la potenzialità di ridurre lo sforzo in termini di tempo e di costo durante esperimenti

in-vitro. Infatti si può determinare l'accuratezza sulla deformazione data dalla fotogrammetria senza dover compiere prove preliminari sul sistema fisico.

II. MATERIALI E METODI

La tecnica stereofotogrammetrica di misura della deformazione è stata valutata simulando un esperimento *in-vitro* in un ambiente virtuale (Figura 2). Per ottenere una valutazione completa del set-up di telecamere sono state acquisite da ciascuna telecamera immagini 2D di tre oggetti: una striscia 2D, un vaso 3D e un vaso 3D in cui è stato espanso uno stent. Successivamente le coordinate tridimensionali dei punti sulla superficie sono state ricostruite e i valori di deformazione sono stati calcolati e

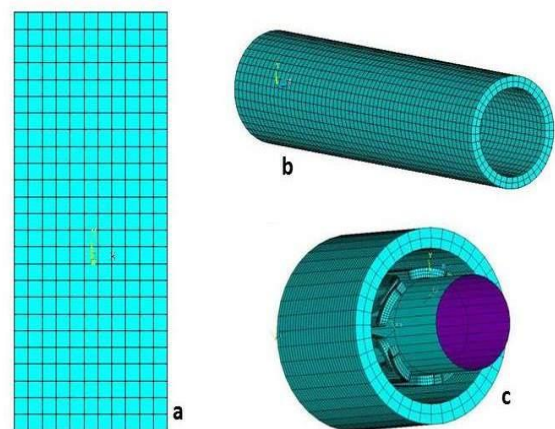


Figura 1 Modelli geometrici utilizzati nelle analisi

confrontati con i valori ottenuti tramite la simulazione agli elementi finiti, eseguita con ANSYS.

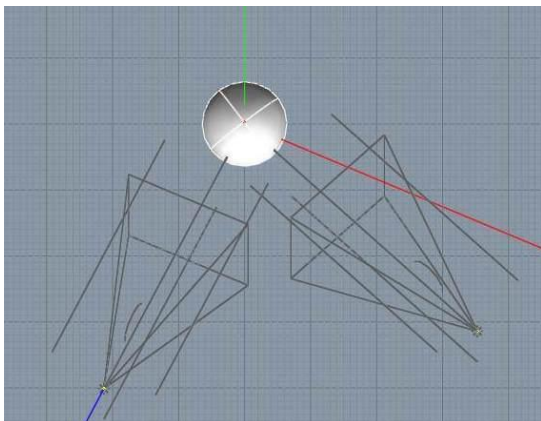


Figura 2 Ambiente virtuale realizzato con il software Realsoft3D

A. Processo di valutazione

Il processo di valutazione applicato al setup fotogrammetrico si è sviluppato in diversi passi: inizialmente sono state fissate la geometria e le proprietà del materiale, poi è stato scritto un input file per la simulazione agli elementi finiti (ANSYS 12.0 Mechanical APDL) che definisce la geometria, la *mesh*, i carichi e le condizioni al contorno del modello e la modalità di elaborazione dei dati ottenuti. Successivamente è stato definito un set up di telecamere virtuali in Realsoft 3D, applicazione capace di modellizzare oggetti e di rappresentare la scena virtuale catturata da una o più telecamere. Il sistema stereo è stato infine calibrato usando un set di immagini di una

scacchiera e un toolbox di Matlab, sviluppato da Bouquet [11].

E' stato possibile importare nel sistema virtuale la geometria creata da ANSYS poichè si conosceva la posizione di ogni nodo della *mesh*. I dati di posizione sono stati forniti da ANSYS e convertiti attraverso un codice Matlab in file JavaScript che definiva la geometria analizzata a tutti gli step di deformazione. I file JavaScript sono stati poi importati nell'ambiente virtuale di Realsoft3D e sono state acquisite l'immagine destra e sinistra dell'oggetto in esame, per replicare il sistema stereogrammetrico sperimentale.

Le immagini sono state poi processate usando due differenti metodi: nel primo caso l'oggetto è stata ricostruito con una funzione che richiede la selezione manuale dei punti di interesse. Il secondo metodo applicato è *l'image registration* eseguita sulle immagini 2D, tramite Shirt (Sheffield Image Registration Toolkit). In entrambi i casi lo scopo era identificare particolari punti corrispondenti sull'immagine destra e sinistra. Infine le coordinate tridimensionali così ricavate sono state utilizzate per calcolare la deformazione sulla superficie, che è stata poi confrontata con i risultati computazionali.

Per stimare l'influenza che il metodo di calcolo ha sull'accuratezza della tecnica sono stati utilizzati tre diversi approcci per determinare la deformazione: la deformazione locale, la deformazione globale calcolata come interpolazione dello spostamento di più nodi sulla posizione, e il tensore delle deformazioni di Green-Lagrange.

Sono state svolte anche analisi preliminari per determinare l'influenza dei parametri del sistema, per esempio risoluzione delle immagini e bontà delle mesh sul valore di deformazione calcolato.

B. Modelli geometrici e di materiale

Sono stati scelti diversi modelli geometrici e di materiale per rappresentare i vari livelli di complessità che possono essere coinvolti in esperimenti reali. Le geometrie utilizzate includono un modello di striscia coerente con il lavoro di Goude [10] e di Zwierzak [9] (Figura 1a), un vaso cilindrico dimensionato con dati reperiti in letteratura (Figura 1b) e per finire lo stesso vaso in cui è stato espanso un modello di stent coronarico MAC4-like fornito dal Politecnico di Milano (Figura 1c). A queste geometrie sono stati applicati diversi modelli di materiale per

verificare la robustezza della tecnica (Tabella 1).

Tabella 1 Modelli di Materiale utilizzati nelle analisi

Materiale	Parametri	Modello
Elastico Lineare (1)	$E = 1 \text{ MPa}$ $\nu = 0.4999$	Striscia
Elastico Lineare(2) [12]	$E = 1.75 \text{ MPa}$ $\nu = 0.49$	Striscia/ Vaso/ Vaso stentato
Iperelastico [13]	$C_1 = 0.020 \text{ MPa}$ $C_2 = 0.003 \text{ MPa}$ $C_3 = 0.175 \text{ MPa}$ $C_4 = 0.090 \text{ MPa}$	Striscia/ Vaso

C. Protocollo di test sulla striscia

La striscia è stata utilizzata per esaminare i dettagli del processo e per eseguire test preliminari utili per identificare parametri utilizzati nelle prove successive. Sulla striscia sono state eseguite due differenti simulazioni con ANSYS: la prima consisteva nell'applicare uno spostamento di 2.5 mm a tutti i nodi, per simulare un test a deformazione nulla, utile per quantificare l'errore assoluto introdotto unicamente dalla selezione manuale dei punti; nella seconda prova, il bordo superiore della striscia è stata fissato ed è stato applicato uno spostamento di 5 mm a tutti i nodi all'estremità inferiore, per realizzare una prova a trazione. E' stato effettuato un primo studio su come un eventuale rumore dovuto alla selezione manuale dei punti, possa propagarsi sul

valore finale di deformazione calcolata. Per simulare questo tipo di inconveniente è stato applicato un errore casuale alle coordinate di 16 punti, estratte dopo aver effettuato il test di trazione. Successivamente la deformazione reale è stata calcolata e confrontata con il valore dato da ANSYS, preso sempre come *gold standard*.

Per studiare come i parametri della telecamera possano influenzare la ricostruzione e l'analisi dei dati, sono state svolte delle prove usando immagini a diversa risoluzione (1020x1020 pixels, 1200x1200 pixels e 2400x2400 pixels). In ciascuna immagine il calcolo della deformazione è stato eseguito su sedici punti e i risultati sono stati confrontati con i valori computazionali.

Sono stati poi valutati diversi metodi di calcolo della deformazione a partire dalle coordinate nodali. In particolare è stato condotto uno studio sulla deformazione globale per ottimizzare il numero di nodi su cui mediare lo spostamento per avere un valore di deformazione accurato. L'interpolazione è stata realizzata su un numero limitato di punti (quarantotto nodi) appartenenti a due colonne della striscia. La deformazione longitudinale globale è stata stimata interpolando un numero sempre crescente di punti

raggruppati in maniera differenziata. Questa prova è stata compiuta usando la simulazione della prova a trazione.

In seguito a questi test preliminari alla striscia è stato applicato il processo di valutazione completo. I punti di interesse sono stati selezionati con i due metodi precedentemente illustrati: ricostruzione manuale delle immagini al primo e ultimo istante di deformazione e *image registration* con le immagini catturate a ciascun istante. Applicare entrambe le tecniche è stato importante per valutare come il metodo di selezione dei punti influenzi l'errore sulla deformazione calcolata e se l'introduzione di approcci alternativi potesse aumentare l'accuratezza del sistema. In questa fase dello studio sono state usate sia la simulazione della prova a deformazione nulla, sia quella a trazione.

D. Protocollo di test sul vaso

Per modellare un vaso sanguigno biologico è stata usata una geometria cilindrica. Sono state condotte tre simulazioni ANSYS in cui la geometria presentava le stesse condizioni al contorno, ovvero è stato impedito lo spostamento dei nodi in direzione assiale e la rotazione attorno all'asse centrale. Nella prima simulazione il vaso è stato

espanso applicando una pressione di 0.016 MPa (120 mmHg) alla superficie interna. Nella seconda è stato applicato uno spostamento di 0.5 mm in direzione radiale ai nodi della superficie interna del vaso, mentre nella terza il vaso è stato iperespanso con una pressione di 0.058 MPa (435 mmHg). Sono stati eseguiti test iniziali per confrontare la deformazione estratta da ANSYS con la teoria dei vasi cilindrici a parete spessa; la simulazione a 0.058 MPa è stata ripetuta per vedere quali fossero le differenze tra i risultati ottenuti considerando le non linearità, dovute alle larghe deformazioni, e quelli ottenuti qualora esse fossero state trascurate. E' stato inoltre realizzato un test di sensitività sulla *mesh* in modo da determinare il miglior compromesso tra densità della *mesh*, tempo di calcolo e numero di punti da selezionare nella ricostruzione manuale. Sono state create quattro *mesh* con un diverso numero di elementi in direzione radiale e circonferenziale. La deformazione è stata studiata su un anello in corrispondenza della metà del vaso. Successivamente la *mesh* è stata rifinita anche in direzione assiale, seguendo lo stesso procedimento sopra descritto. Infine anche a questa geometria è stato applicato l'intero processo stereoscopico

virtuale. In particolare, il vaso è stato testato usando un modello di materiale lineare elastico (2) e uno iperelastico (Tabella 1) che hanno comportano una diversa risposta del vaso. Come per la striscia, anche in questo caso sono stati applicati entrambi i metodi di selezione dei punti di interesse.

E. Protocollo di test sul vaso con stent

Per simulare il caso più realistico che si possa dover affrontare in un esperimento *in-vitro*, è stata analizzata una geometria cilindrica al cui interno è stato espanso uno stent. La dilatazione dello stent è stata simulata tramite il contatto con una superficie rigida che mimava l'azione di un palloncino da angioplastica. Sulla superficie rigida è stato applicato uno spostamento radiale di 0.5 mm e il vaso è stato vincolato alle estremità in modo che non potesse ruotare, nè muoversi in direzione longitudinale.

Inizialmente è stato condotto un test di sensitività della *mesh*, come riportato nel paragrafo precedente per il vaso semplice. In primo luogo sono state realizzate quattro *mesh* con un diverso numero di elementi in direzione radiale, assiale e circonferenziale. Successivamente i valori di deformazione di ciascuna di esse sono stati confrontati

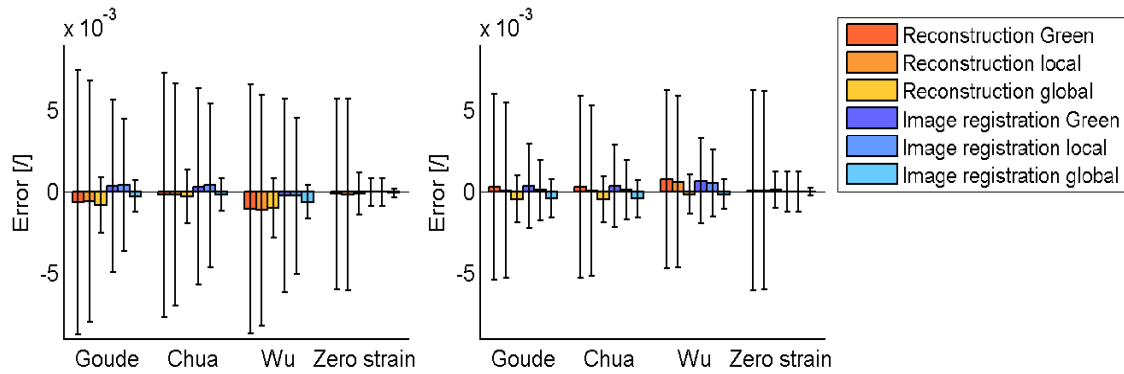


Grafico 1 Errore sulla deformazione della striscia calcolato tra i dati estratti dai test e quelli derivanti da ANSYS in direzione trasversale e longitudinale

con quelli estratti dalla simulazione con la *mesh* più fine, assunta come *gold standard*.

Inoltre è stata infine analizzata la deformazione calcolata da ANSYS su circonferenze del vaso a differenti posizioni assiali, per verificarne la simmetria rispetto alla mezzeria del vaso.

In seguito ai test preliminari, è stato applicato l'intero processo stereoscopico virtuale.

Come per i precedenti modelli, sono stati utilizzati entrambi gli approcci per l'acquisizione dei punti di interesse.

III. RISULTATI

A. Striscia

L'analisi sulla propagazione dell'errore, dalle coordinate dei punti, al valore di deformazione calcolata, mostra che l'accuratezza della selezione dei punti ha un grande impatto sul risultato finale, indipendentemente dal metodo usato per

calcolarla. I risultati suggeriscono che applicando un errore random sulla posizione nodale estratta dopo una completa trazione del provino, può essere prodotto un errore sulla deformazione longitudinale di 0.022, se viene calcolata con la formula di Green e di 0.021, se si utilizza quella della deformazione locale. L'indagine sull'influenza della risoluzione dell'immagine mostra che l'errore sulla deformazione calcolata si riduce notevolmente con l'incremento della risoluzione dell'immagine, indipendentemente dal livello di deformazione della geometria. Questo errore in direzione trasversale decresce da uno 0.0103 ad uno 0.004 mentre in direzione longitudinale passa da 0.0069 a 0.0016 quando la risoluzione cambia da 1020 a 2400 pixel. Questo suggerisce che acquisire immagini ad alta risoluzione è importante per fare un'accurata valutazione della deformazione. Per

quanto concerne l'analisi attraverso la deformazione globale, il miglior compromesso tra smorzamento dell'errore sulla posizione e perdita di informazioni, è stato ottenuto con l'interpolazione tra gruppi di cinque punti, presi in serie. In particolare l'errore sulla deformazione longitudinale è di 0.0011 allo step intermedio di deformazione e di 0.0014 alla fine della prova di trazione. Sebbene questo metodo smussa l'errore sulla deformazione, introduce una perdita di informazione sulla distribuzione della stessa.

I risultati della valutazione completa del processo applicato all'intera geometria, con modifica delle proprietà del materiale e utilizzo di diverse tecniche di acquisizione delle posizioni dei nodi, sono riportati sotto forma di errori tra le deformazioni calcolate da ANSYS e quelle calcolate analiticamente.

Il livello di deformazione in direzione longitudinale è di circa 19% mentre in quella trasversale è di -9%. Nel Grafico 1 sono riportati i valori medi dell'errore in direzione trasversale e longitudinale tra i dati di ANSYS e quelli calcolati, per i tre modelli di materiale studiati.

Le barre rappresentano la dispersione dell'errore intorno al valore medio e sono calcolate come deviazione standard. La

differenza tra il valore di deformazione calcolato a partire dalle posizioni ricostruite e quello calcolato con le coordinate fornite da ANSYS mostra un errore sulla deformazione trasversale di 0.0087 e su quella longitudinale di 0.0062. Questo dimostra che l'errore introdotto dal processo di elaborazione dei dati è più piccolo dell'imprecisione introdotta dal metodo di acquisizione dei punti.

Le barre di errore relative all'acquisizione tramite *image registration* sono più piccole di quelle associate ai valori calcolati a partire da dati provenienti dalla ricostruzione manuale in tutti i casi.

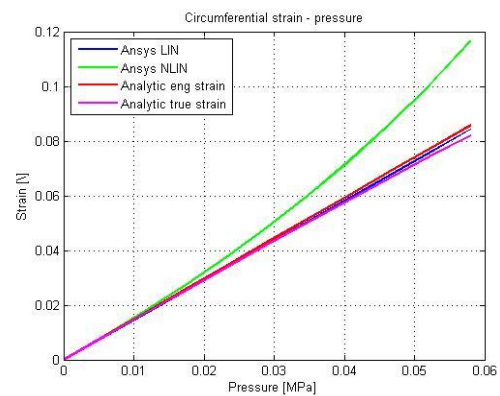


Grafico 2 Confronto tra i valori di deformazione circonferenziale calcolati senza e tenendo in considerazione le non linearità

B. Vaso

I test preliminari suggeriscono che la miglior mesh che ottimizza la simulazione computazionale è composta da 40 elementi in direzione

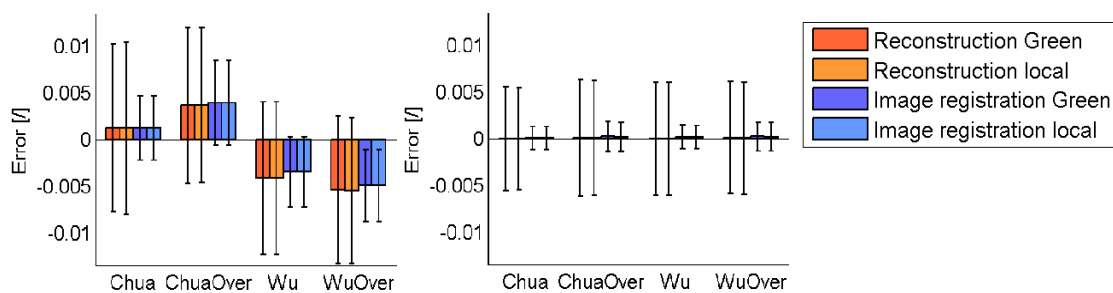


Grafico 3 Errore sulla deformazione del vaso calcolato tra i dati estratti dai test e quelli derivanti da ANSYS in direzione assiale e circonferenziale

circonferenziale, 60 in direzione assiale e 2 elementi in direzione radiale. Il confronto tra i dati attesi, calcolati attraverso la teoria del vaso spesso, e le deformazioni da ANSYS mostra una buona corrispondenza quando nella simulazione vengono inattivati gli effetti di non linearità. Quando invece le non linearità sono tenute in considerazione, i risultati computazionali seguono quelli attesi solo in piccole deformazioni (2%). Sopra a questo livello, il comportamento della curva pressione-deformazione diventa non lineare (Grafico 2). Nell'applicazione effettiva le non linearità

sono incluse per permettere la simulazione delle grandi deformazioni a cui i tessuti biologici sono effettivamente sottoposti.

I risultati di valutazione dell'intero processo, applicato al vaso, con variazione del modello di materiale e di metodo di acquisizione dei punti sono riportati sotto forma di errore sul valore di deformazione tra i dati di ANSYS e quelli derivati dal metodo di misura (Grafico 3). Date le condizioni al contorno, la deformazione assiale attesa è nulla, mentre quella circonferenziale è di circa 0.025 per il vaso espanso a 120

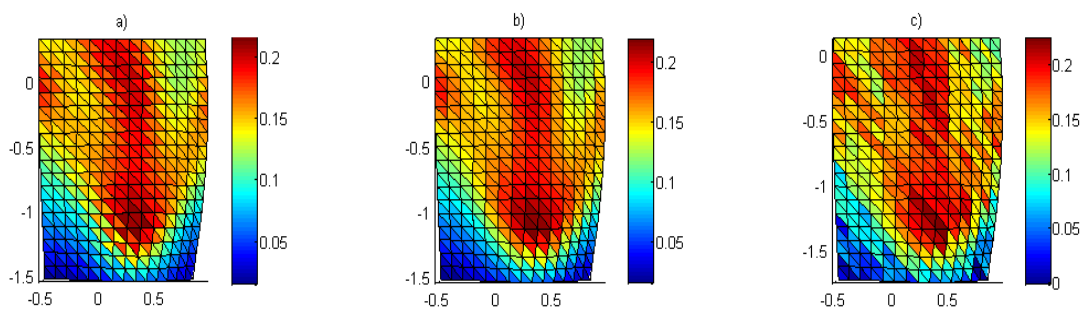


Figura 3 Distribuzione della deformazione circonferenziale sulla superficie del vaso, dopo completa espansione dello stent

mmHg e di 0.290 per quello iperespanso. L'errore medio in direzione circonferenziale è più grande di quello in direzione assiale. Questo è probabilmente dovuto alla presenza di una curvatura nella geometria. Inoltre la differenza tra il valore di deformazione circonferenziale estratto da ANSYS e quello calcolato è di 0.0105 per il primo test e di 0.0133 per l'ultimo, mostrando come l'errore relativo diminuisca con l'aumentare della deformazione. Come osservato per la striscia, le barre di errore relative ai dati provenienti dall'*image registration* sono minori di quelle associate ai dati dalla selezione manuale dei punti.

C. Vaso espanso con stent

Il test di sensitività della mesh suggerisce che la mesh che ottimizza la simulazione computazionale è composta da 80 elementi in direzione circonferenziale, 120 in quella assiale e 4 in quella radiale.

Gli spostamenti e le deformazioni estratte a diverse coordinate assiali lungo il vaso sono simmetrici rispetto alla mezzeria solo nella parte centrale, mentre, nelle porzioni di vaso in corrispondenza alle estremità dello stent, la simmetria viene persa. Questo è dovuto all'effettiva asimmetria della geometria dello stent nelle due estremità. Nell'ultimo test i risultati sono stati valutati solo in una sezione del modello dello stent, al centro del vaso. La Figura 3 mostra la distribuzione della deformazione circonferenziale sulla superficie del vaso quando lo stent è completamente espanso: deformazione valutata da ANSYS (a), deformazione di Green derivata dalle coordinate estratte da ANSYS (b), deformazione di Green derivata dalle coordinate estratte in seguito alla ricostruzione manuale della geometria (c).

Il Grafico 4 riporta l'errore assoluto sulla

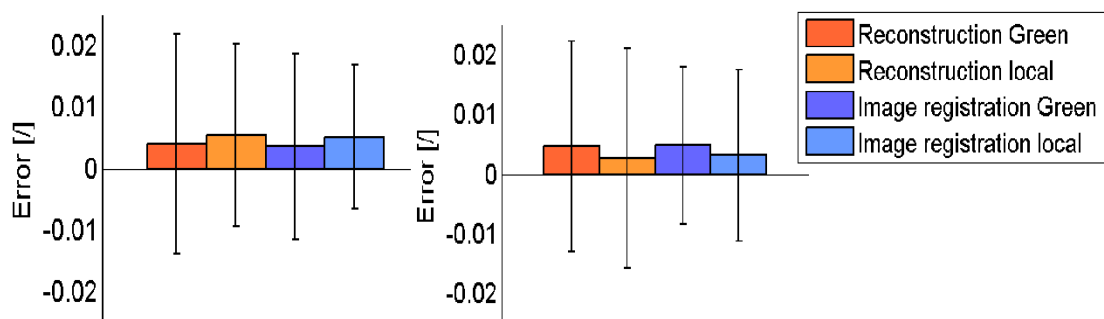


Grafico 4 Errore sulla deformazione del vaso stentato calcolato tra i dati estratti dai test e quelli derivanti da ANSYS in direzione assiale e circonferenziale

deformazione calcolato tra i dati di ANSYS e quelli derivati, in direzione assiale e circonferenziale. Gli errori misurati in entrambe le direzioni sono maggiori di quelli ottenuti dall'analisi delle geometrie più semplici, infatti l'errore raggiunto in direzione assiale è di 0.0218 e quello in direzione circonferenziale è di 0.0222.

Le barre di errore relative all'acquisizione dei punti tramite *image registration* sono leggermente minori di quelle associate ai dati estratti con la ricostruzione manuale.

IV. DISCUSSIONI

L'analisi effettuata sulla striscia presenta un errore sulla deformazione in direzione trasversale di 0.0087, quando i dati sono estratti con la ricostruzione manuale, e di 0.0063, quando sono estratti con l'*image registration*. In direzione longitudinale invece, gli stessi errori sono di 0.0062, se i dati sono estratti con il metodo manuale, e di 0.0033, se sono estratti con quello automatico. Considerando l'applicazione di questo metodo per misurare le deformazioni e prendendo come soglia di accuratezza uno 0.01, la tecnica fotogrammetrica è stata validata in entrambe le direzioni. L'errore in direzione trasversale è più grande di

quello in direzione longitudinale e questo può essere dovuto alla presenza di piccole deformazioni, infatti la differenza percentuale di deformazione tra i dati di ANSYS e quelli derivati è al massimo di 7.74% in direzione trasversale e di 2.31% in quella longitudinale. Analogamente il modello è soggetto a una deformazione massima trasversale di 0.09 e longitudinale di 0.2. Per questa geometria semplice la corrispondenza tra la deformazione di ANSYS e il valore calcolato è buona. Per quanto riguarda il vaso, la direzione di interesse è quella circonferenziale poiché l'espansione dello stent interessa soprattutto la deformazione in quel senso. I risultati derivanti dall'intero processo mostrano che l'errore sulla deformazione raggiunge un massimo sul vaso iperespanso di 0.0133, se i punti sono selezionati manualmente, mentre è di 0.0088, se viene utilizzato il metodo dell'*image registration*. Poiché questi valori massimi corrispondono al test di iperespansione del vaso, è stato valutato che l'accuratezza è sufficiente. Anche in questo caso l'*image registration* opera meglio del metodo di selezione manuale, infatti la dispersione dell'errore risulta sempre minore di quella ottenuta con l'approccio manuale. Prendendo come

soglia di riferimento lo 0.01, la tecnica è stata validata anche utilizzando una geometria di forma cilindrica, con un visibile miglioramento della stessa qualora venga utilizzato il metodo di selezione dei punti automatico (*image registration*).

La validazione, compiuta su un vaso in cui è stato espanso uno stent, mostra un errore alto sia in direzione assiale che in quella circonferenziale: 0.0218 per la prima e 0.0222 per la seconda. L'*image registration* migliora questi valori raggiungendo gli 0.0186 e 0.0180 e, sebbene anche questi ultimi risultati non siano al di sotto della soglia fissata, questa tecnica rappresenta comunque una via sicura verso lo sviluppo di un sistema più accurato. Questi errori possono derivare dalla formula applicata per calcolare la deformazione, per esempio, l'utilizzo di elementi triangolari per calcolare il tensore di Green-Lagrange, ipotizza la deformazione costante, all'interno di ciascuno di questi elementi. Un confronto più generale, tra le tre geometrie e i modelli di materiale utilizzati, dimostra che la misurazione delle deformazioni utilizzando una tecnica stereofotogrammetrica è molto accurato nelle grandi deformazioni e con geometrie semplici e che sono necessari

ulteriori sviluppi per analizzare configurazioni come quella del vaso in cui è stato espanso uno stent, a causa della maggior complessità della struttura. Il paragone tra i dati derivati dalla ricostruzione e i valori calcolati direttamente dalle posizioni fornite da ANSYS presenta sempre una buona corrispondenza e un errore piccolo nella direzione di interesse e nel caso di grandi deformazioni. Questo evidenzia che la differenza tra i risultati è dovuta principalmente al metodo di elaborazione dei dati (per esempio la formula usata per calcolare la deformazione) e meno al metodo di selezione dei punti. La tecnica può essere migliorata usando metodi alternativi per calcolare la deformazione. In ogni caso l'uso dell'*image registration* migliora l'accuratezza della selezione dei punti sulla geometria 3D.

V. CONCLUSIONI

In questo lavoro di tesi è stato sviluppato un metodo per valutare l'accuratezza di un sistema fotogrammetrico per la misurazione delle deformazioni. Questo approccio confronta le deformazioni quantificate dal software ANSYS Mechanical con i valori misurati

attraverso l'utilizzo di un sistema fotogrammetrico virtuale.

In particolare, è stato testato un set-up di due telecamere con una lunghezza focale di 60 mm. I risultati mostrano un errore sulla deformazione minore dello 0.01 in caso di grandi deformazioni e geometrie semplici. Geometrie più complesse sono affette da errori dell'ordine di 0.02, i quali suggeriscono comunque un'accuratezza del sistema adeguata per esperimenti *in-vitro* su vasi semplici o nei quali viene impiantato uno stent. L'espansione dello stent ricade infatti nell'ambito delle grandi deformazioni e può essere studiata attraverso la fotogrammetria. I test dimostrano anche un miglioramento dell'accuratezza dei dati calcolati grazie all'introduzione dell'*image registration*.

L'analisi del metodo fotogrammetrico riportata in questo lavoro prova che questo processo di valutazione è efficace e conveniente. In particolare può essere

utilizzato per predire l'accuratezza di misura della deformazione, senza dover necessariamente eseguire test sperimentali. La possibilità di fare test preliminari utilizzando un ambiente virtuale è uno strumento potente per ridurre lo sforzo in termini di mezzi e di tempi, legati invece all'approccio sperimentale. Per esempio vi è la possibilità di variare un singolo parametro del sistema di telecamere, indipendentemente dalle altre caratteristiche, e valutare l'influenza che questo cambiamento apporta alla misura finale di deformazione. Un simile esame su un sistema fisico comporterebbe un costo elevato in termini di strumentazione e tempo.

La fotogrammetria per la misurazione delle deformazioni è quindi una tecnica utile alla ricerca sperimentale sia in ambito accademico che per applicazioni industriali.

Summary

I. INTRODUCTION

Coronary artery disease has been recognised as the leading cause of mortality in developed as well as developing countries and most commonly involves atherosclerotic occlusion of the coronary arteries [1], causing reduced blood flow in affected vessels due to the presence of a plaque. As a solution for this problem in 1985 Palmaz et al. proposed the use of a balloon mounted stent to maintain the luminal integrity of diseased blood vessels. These intravascular stents are small tube-like structures which are expanded within the stenotic artery to restore blood perfusion to the downstream tissues [2].

Nowadays, stent implantation is a common procedure with a high rate of success when compared with angioplasty alone [3]. However some limitations are still present: for example, stent deployment inside an artery has implications for the stresses and deformation of the arterial wall, which has been associated with the progression of excessive proliferation of the vessel tissue, known as in-stent restenosis [4].

The knowledge that the success of the implantation is linked to stent design, and therefore the interactions of the stent with the vascular wall, has encouraged research to focus on the stresses and the deformations generated during the expansion of the device. This has been addressed both with *in-vitro* experiments and computational simulations.

In particular, computational structural analysis has emerged in recent years to investigate the mechanical response to angioplasty and stent placement in the arterial wall during the device expansion ([5];[6];[7];[8]). *In-vitro* experimental analysis has included stereoscopic measurement, involving the use of two or more cameras to capture two-dimensional images with subsequent reconstruction of a three-dimensional surface. This technique has been used in the Department of Cardiovascular Science, University of Sheffield ([9];[10]).

This study extended the effort of these previous studies by validating a stereoscopic method for the measurement of vessel deformation when a stent is implanted. To reduce the uncertainty associated with an experimental stereoscopic system the whole analysis were performed using a virtual camera set-up and the derived data were

compared with ANSYS finite element simulations. The technique was evaluated with three geometries, gradually moving towards a more realistic model: a 2D strip, a 3D vessel and a 3D stented vessel. The material properties were varied to quantify the sensitivity of the system to different tissue behaviour. The results of the study aimed to determine the accuracy of the technique independently from experimental error sources (e.g. lens distortions or refraction), to assess methods of surface strain analysis and to define recommendations for future experimental application of the technique.

The possibility of doing some photogrammetry preliminary tests, by using a virtual environment, could have the potentiality to reduce the effort in terms of time and money during *in-vitro* experiments and to define an accuracy threshold calculated on the strain through this technique.

II. MATERIALS AND METHODS

A stereo-photogrammetric strain measurement technique was evaluated by simulating an *in-vitro* experiment within a virtual reality environment (Figure 2). To obtain a complete characterisation of the camera set-up the behaviour of three

objects (a 2D strip, a 3D vessel and a 3D stented vessel) were captured in 2D by each camera and reconstructed in 3D to allow comparison of derived surface strain measurements with strain values computed using the ANSYS finite element software.

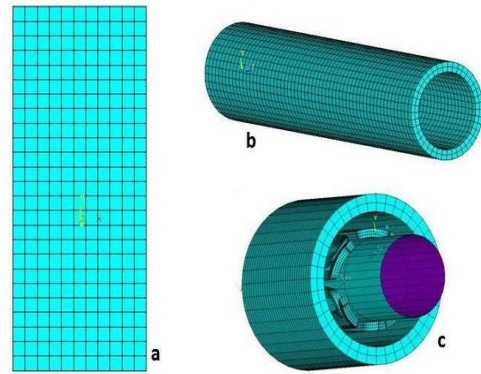


Figure 1 Geometry models used in the analyses

A. Evaluation process

The evaluation process applied to the photogrammetric set-up consisted of several steps: the geometry and material properties of the object were specified, an input file was then written to define the geometry, mesh, loads and boundary conditions of the model and the post-processing of the data in the finite element package, ANSYS 12.0 Mechanical APDL.

A virtual stereo camera set-up was defined in Realsoft3D, a modelling and ray tracing application capable of simulating physical objects and rendering

the virtual scene captured by one or more cameras. The stereo system was calibrated using images of a set of checkerboards and a Matlab calibration toolbox developed by Bouguet [11].

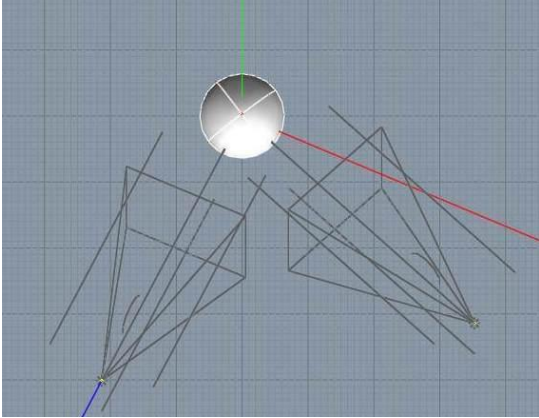


Figure 2 Virtual environment in Realsoft3D

The ANSYS geometry was imported into the virtual rig using the position of each node, extracted from the ANSYS data and converted by Matlab code to generate a JavaScript file with the geometry at every step of deformation. These JavaScript files were imported into the Realsoft3D camera rig and images from the left and right camera were captured, to replicate an experimental stereogrammetric system.

Stereo image data was processed using two methods: in the first case the pictures were reconstructed with a manual function requiring hand-picking of points of interest in both left and right images. The second method applied image registration using the ShIRT software (Sheffield Image Registration Toolkit) to

the two-dimensional images. In both cases the aim was to identify corresponding points in two images and obtain the three-dimensional coordinates. Finally the three-dimensional positions were used to calculate the surface strains and the data were compared with the computational results.

In order to assess the influence of the strain calculation method on the accuracy of the technique three strain measures were derived from the data: a local strain computed as true strain on a segment length, a global strain derived from the interpolation of nodal displacements and the Green-Lagrange strain tensor.

Preliminary analyses were also performed to determine the influence of system parameters (e.g. resolution and refinement mesh) on the calculated strain values.

B. Geometrical and material models

Different geometric and material models were chosen to represent the varying levels of complexity involved in a real experiment. The model geometries included a strip consistent with the work of Goude [10] and Zwierzak [9] (Figure 1a), a cylindrical vessel sized to match experimental and literature data (Figure 1b) and the same vessel stented with a

MAC4-like coronary stent provided by Politecnico di Milano (Figure 1c).

Several material models were applied to these geometries to test the robustness of the technique (Table 1):

Table 1 Material models

Material	Parameters	Model
Linear Elastic (1)	$E = 1 \text{ MPa}$ $\nu = 0.4999$	Strip
Linear Elastic (2) [12]	$E = 1.75 \text{ MPa}$ $\nu = 0.49$	Strip/ vessel/ stented vessel
Hyperelastic [13]	$C_1 = 0.020 \text{ MPa}$ $C_2 = 0.003 \text{ MPa}$ $C_3 = 0.175 \text{ MPa}$ $C_4 = 0.090 \text{ MPa}$	Strip/ vessel

C. Strip test protocol

The strip geometry was used to examine the detail of the process and to perform tests to identify issues relevant to subsequent tests in more complex geometries. Two different ANSYS simulations were undertaken on the strip: the first consisted of 2.5 mm displacement applied to all the nodes of the strip over ten steps to simulate a zero strain condition to quantify the absolute error on strain introduced by manual point picking (zero strain test); in the second trial the geometry was fixed at the upper edge and a displacement of 5 mm was applied to the nodes on the lowest side of the strip, to replicate a tensile test performed over ten steps.

A study of the influence of noise was executed to examine how errors due to manual picking of points would affect the resulting values of strain. A random noise was applied to the position of sixteen points extracted from the ANSYS tensile strip simulation to simulate the error introduced by manual reconstruction. The strain was then calculated and compared to the computational values.

To study how camera parameters affect the reconstruction and the data analysis variation of image resolution was performed. The strain measurement technique was carried out on sixteen points at different levels of resolution (1020x1020 pixels, 1200x1200 pixels and 2400x2400 pixels) and the results were compared to the computational values.

Several methods were evaluated to calculate strain from the surface positions. In particular the global strain was studied to quantify the optimal number of nodes over which averaging of displacement was effective. Averaging was executed on a restricted set of points (forty-eight nodes) lying on two lines on the strip to calculate longitudinal strain values. The global strain was computed by interpolating an increasing number of points using two different methods of choosing this groups of data.

These three trials were carried out using the tensile test simulation.

Following these preliminary tests the complete evaluation process was applied to the whole strip geometry. The comparison of point reconstruction with two different methods was used to assess how the picking-point method influenced the error on the derived strain and if the introduction of alternative approaches could decrease this inaccuracy. The two approaches used to extract the nodal coordinates were the following: a manual reconstruction of the object at the first and final configuration and image registration between images at each step of deformation. Both the zero strain and tensile test were undertaken in this phase of the study.

D. Vessel test protocol

A cylindrical geometry was used to represent the experimental imaging of a biological vessel. Three ANSYS simulations were performed with the same boundary conditions, constraining the nodes in the longitudinal and circumferential direction. In the first case the vessel was expanded by a pressure of 0.016 MPa (120 mmHg) applied to the internal surface of the cylinder over ten steps. The second simulation applied a

radial displacement of 0.5 mm to the internal nodes of the vessel over ten steps and in the third analysis the vessel was over-expanded, applying a pressure of 0.058 MPa (435 mmHg).

Initial tests were executed to compare the ANSYS simulations with thick-walled theory. The simulation at 0.058 MPa was run twice including the non-linearity due to the large deformations and with the non-linearity option deactivated.

A mesh sensitivity test was carried out to determine the best trade-off between mesh density, computational time and effort to undertake manual reconstruction. Four meshes with different numbers of elements in the radial and circumferential direction were set-up and the variation of strains taken on a central ring of the vessel surface was studied. Then, with the same process described before, the mesh was refined also in the axial direction.

Finally the complete virtual stereoscopic process was also applied to this geometry as reported for the strip. In particular, the vessel was tested using two material models (linear elastic 2 and hyperelastic shown in Table 1) inducing different levels of deformation. As for the strip also in this case the two approaches for the picking-point were applied.

E. Stented vessel test protocol

A stented vessel geometry was analysed to simulate the challenges associated with a realistic *in-vitro* experiment. Stent deployment was simulated in ANSYS by expanding the stent within the vessel using a rigid contact surface to mimic balloon inflation. A radial displacement of 0.5mm was applied to the contact surface and at the ends of the model the vessel geometry was constrained in the circumferential and axial directions.

An initial mesh sensitivity test was performed as reported for the simple vessel configuration. Four meshes with different numbers of elements in the radial, circumferential and axial direction were used to compare the resulting strains with those extracted from the finest mesh model.

A comparison between the ANSYS strains on circumferential rings at different axial positions was undertaken

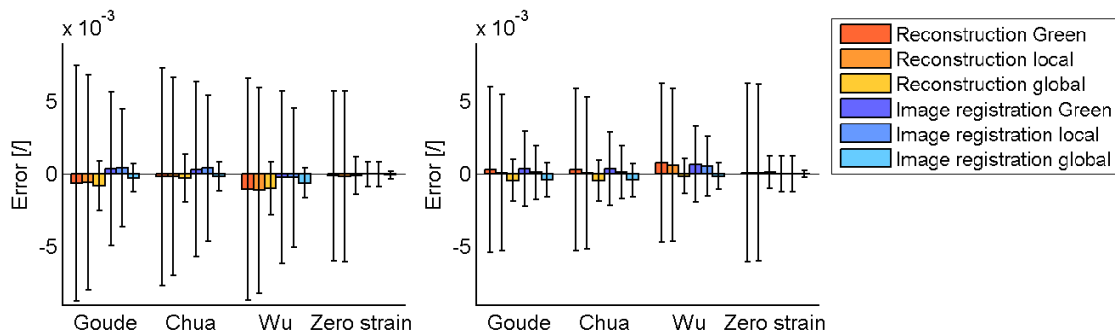
to clarify if the strain generated within the vessel is symmetric with respect to the middle of the geometry.

Following these initial tests the complete virtual stereoscopic process was performed. As for the previous models two approaches for the position acquisition were applied.

III. RESULTS

A. Strip

Analysis of the contribution of noise showed that the accuracy of manual picking has a large impact on strain measurements, independent of the method used to derive strain. The results suggested that, applying a random error on the nodal position extracted after a complete tensile test simulation, an error on the longitudinal strain of 0.022 could be produced, if the deformation was calculated with the Green-Lagrange tensor and of 0.021, if this one was calculated with the local strain formula.



Graph 1 Error on strain on the strip between test data and ANSYS reported data in transversal and longitudinal direction.

The investigation of image resolution indicated that the error on the derived strain significantly reduced with increasing image resolution, independently from the level of deformation. The error on the strain in the transversal direction went from 0.0103 to 0.004 and in the longitudinal direction improved from 0.0069 to 0.0016 when the resolution changed from 1020 to 2400 pixels. This suggested that high resolution image acquisition is important for accurate strain evaluation.

As regards the global strain analysis the optimal trade-off between position error smoothing and loss of information was obtained when interpolation over on five points taken with a serial approach. In particular the error on longitudinal strain was 0.0011 at the medium deformation step and 0.0014 at the final step. Though this method smoothes the strain error, it introduces a loss of information on the strain distribution.

The results of the complete evaluation process applied to the whole geometry with variation in material properties and acquisition technique are reported as the error between the ANSYS and derived strain measurement. The level of strain in the longitudinal direction was about 19%

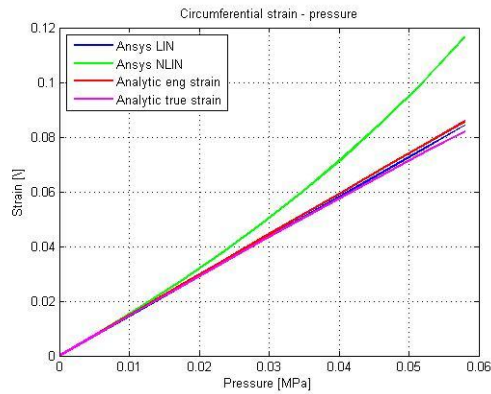
and -9% along the transversal axis. Graph 1 reports the mean values of error in the transversal and longitudinal direction for the three material models between the ANSYS data and the derived values.

The reported error bars represent the scattering of the error around the mean value, reported using the standard deviation. The difference between strain values derived from 3D reconstructed coordinates and processed ANSYS reported data resulted in a maximum error on transversal strain of 0.0087 and on longitudinal strain of 0.0062. This demonstrates that the error introduced by the post-processing was smaller than the inaccuracy introduced by the acquisition method.

The error bars related to the image registration acquisition were smaller than those associated with the manual reconstruction in every case.

B. Vessel

The preliminary tests suggested that the best mesh which optimised the computational simulation was discretised with 40 elements in the circumferential direction, 60 elements in the axial direction and 2 elements in radial direction.

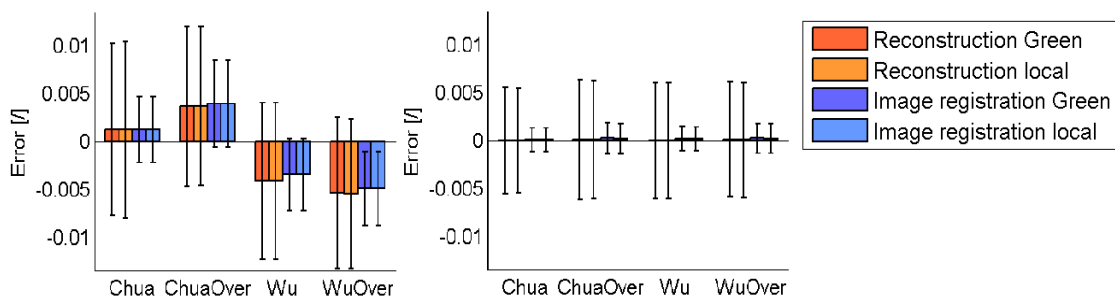


Graph 3 Comparison between circumferential strains obtain with and without taking into account non-linear effects

The comparison between the expected data calculated from the analytic thick-walled vessel formulation and the ANSYS strains showed a good agreement when the non-linearity effects were turned off. When taking into consideration the non-linearity, the computational results followed the expectations only for a low level of deformation (strain of 2%). Above this value of strain the behaviour of the pressure-strain curve became non-linear (Graph 3). In the actual application the non-linearities were included to allow simulation of large deformation of a

biological soft tissue. The complete evaluation process was applied to the vessel with variation of both the material model and acquisition technique. The results are reported in the bar plots as the error on the strain values between the ANSYS strain values and the derived strain measurement (Graph 2). Due to the boundary conditions the axial strain was expected to be zero, while the hoop strains were around 0.025 for the vessel expanded with 120 mmHg and 0.290 for the overexpansion.

The mean errors in the circumferential direction appeared larger than in the axial, possibly due to the bending of the geometry. The deviations of the hoop derived strains with respect the ANSYS values went from a scattered value of 0.0105 for the first test to 0.0133 in the last trial, showing that the absolute error raised with the increasing of the level of deformation. As observed for the strip the error bars related to the image registration



Graph 2 Error on strain on the vessel between test data and ANSYS reported data in axial and circumferential direction.

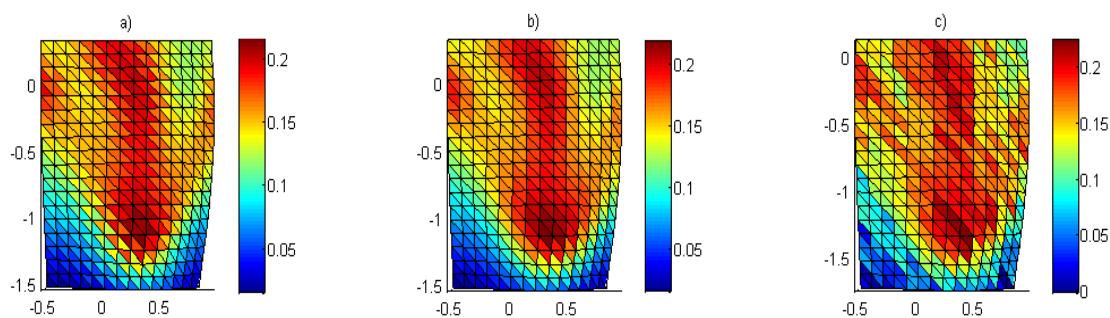


Figure 3 Circumferential strain distribution on the vessel surface, after complete stent expansion

were smaller than those associated with the manual reconstruction in every case.

C. Stented vessel

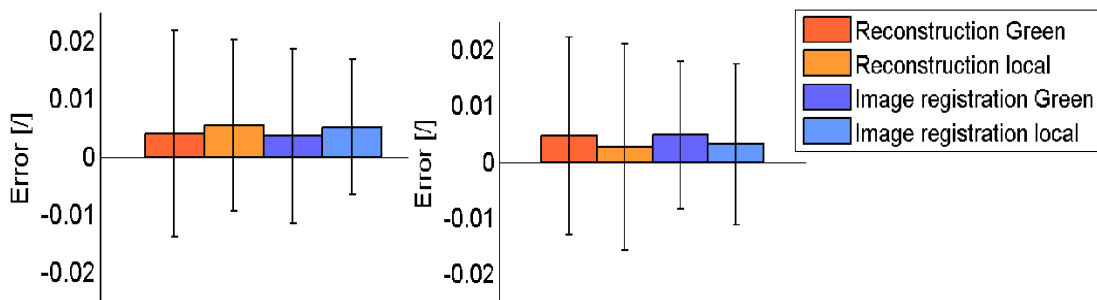
The mesh sensitivity test suggested that the best mesh which optimised the computational simulation was discretised with 80 elements in the circumferential direction, 120 elements in the axial direction and 4 elements in radial direction.

Analysis along the axial direction showed that the displacements and the strains were symmetric in the region local to the center of the stented vessel geometry, whilst symmetry was not maintained in the regions close to the end of the stent.

This is due to the asymmetry of the stent geometry at each end of the stent.

In the final test results were evaluated in a section of the stent model close to the center of the vessel. Figure 3 shows the distribution of circumferential strain on the surface of the stented vessel in the fully deployed configuration: strain reported from ANSYS (a), Green strain derived from ANSYS coordinates (b), Green strain derived from manual-reconstructed geometry (c).

Graph 4 reports the absolute errors on strain between the ANSYS data and the derived strain measurement in the axial and circumferential direction. The errors measured in both direction were greater



Graph 4 Error on strain on the stented vessel between test data and ANSYS reported data in axial and circumferential direction.

than those obtained for simple geometries, in fact the scattered error reached 0.0218 in the axial direction and 0.0222 in the hoop direction.

The error bars related to the image registration acquisition were slightly smaller than those associated with the manual reconstruction.

IV. DISCUSSION

The analysis conducted on the Strip geometry presented a strain error in the transversal direction of 0.0087 for the manual reconstruction and of 0.0063 for the image registration. Instead in the longitudinal direction the strain errors are 0.0062 for the first approach and 0.0033 for the second method. Considering the application of this strain measurement method and taking an absolute accuracy threshold of 0.01, the photogrammetric technique was validated in both directions. Though the error in the transversal direction is larger than in the longitudinal and this could be due to the small level of deformation, in fact the percentage deviation of strain between the ANSYS data and the derived measures is maximum 7.74% in the transversal direction and 2.31% in the longitudinal one. Correspondingly the

specimen is subjected to a maximum transversal strain of 0.09 while in the y direction the maximum strain approaches 0.2. For this simple geometry the agreement between the ANSYS strain and the derived values was good.

Considering the Vessel geometry, the direction of interest is circumferential since stent expansion affects mostly the hoop deformations. The maximum error on circumferential strain extracted with the manual reconstruction was 0.0133 and occurred in the overexpanded vessel, whilst for the image registration that same test had a strain error of 0.0088. Since these higher values of error corresponded to the over-expanded configuration, the accuracy was tested to be sufficient. Also in this instance the image registration performed better than the manual picking method, in fact the scattered errors always resulted lower than those obtained with the manual approach. Taking as reference the 0.01 threshold the technique applied on a cylindrical shape was not validated with the reconstruction technique, while there is a visible improvement with the image registration.

The validation performed on the Stented vessel resulted in higher errors in both axial and circumferential directions, in

fact the error on axial strain was 0.0218 and on circumferential strain was 0.0222. The image registration improved these values to 0.0186 and 0.0180 and although the IR deviation is not within the suggested threshold this is a promising development for a more accurate system. These errors may arise from the formula applied to calculate the strains as the use of triangular elements to calculate the Green-Lagrange tensor assumes constant strain within each element.

The comparison among all the geometries and materials demonstrated that the photogrammetric strain measurement is particularly accurate in case of large deformation with simple geometries, while some further refinements are required in the stented vessel configuration because of the more complex nature of the structure. The comparison between the data derived from the reconstruction and the values derived directly the ANSYS position always showed a good agreement and little error in the direction of interest and under large deformations. This means that the difference in results was caused mainly by the post-processing (e.g. strain measurement relationship) and in lower proportion by the acquisition method. The technique can be improved using

alternative methods to derive the strain from the deformed geometry. The use of image registration improved the accuracy of acquisition of the 3D geometry in all cases.

V. CONCLUSIONS

This study has developed a method to easily evaluate a photogrammetric strain measurement system. The method used comparison between data computed by ANSYS Mechanical software and values derived from a virtual photogrammetric rig.

In particular, a stereo camera set-up with 60 mm focal length was tested and the results showed a strain error of less than 0.01 under large deformations with simple geometries. More complex geometries were affected by errors of the order of 0.02 which suggest reliable accuracy for large deformation stent application. The tests also demonstrated improvement of the agreement with the introduction of image registration using the ShIRT software developed by the University of Sheffield.

The evaluation method reported in the present work is an effective and convenient technique which can be used to validate a camera set-up and predict the accuracy of photogrammetric strain

measurements before performing experimental tests. The possibility of preliminary testing of a photogrammetric rig in a virtual environment is a powerful tool in the *in-vitro* approach to reduce experimental effort and ensure minimal accuracy thresholds for derived strain results. For example there is the possibility of varying one single set-up parameter at a time and study its

influence on the final strain measurement. This investigation on a physical system would demand a lot in terms of instrumentation and time.

The photogrammetry has confirmed as a powerful technique for the strain measurement in the academic applications and it could be used also in the industrial research field.

Introduction

1. Stenting methodology and problems

Coronary artery disease (CAD) has been recognized as the leading cause of mortality in developed as well as developing countries and is most commonly due to atherosclerotic occlusion of the coronary arteries. In more than 90% of cases, the cause of myocardial ischemia is reduction of coronary blood flow owing to atherosclerotic coronary arterial obstruction. Pathologies like angina and coronary ischemia are demonstrated to be the results of regional blood flow differences[1].

Nevertheless atherosclerosis is a process that can involve many of the body's blood vessels with a variety of presentations. When it involves the aorta it results in aortic aneurysms, when it is related to the cerebral arteries then cerebrovascular diseases like transient ischemic attack or stroke can happen, when it concerns peripheral arteries like the ilio-femoral and popliteal or the mesenteric it can respectively emerge in peripheral vascular disease and intestinal ischemia.

Atherosclerotic diseases cause a reduction of the blood flow because of the narrowing or occlusion of the affected vessels due to the presence of a plaque. As a solution for this problem coronary angioplasty was introduced by Grüntzig et al in 1977 and in 1985 Palmaz et al. proposed the use of a balloon mounted stent to maintain the luminal integrity of diseased blood vessel. Intravascular stents are small tube-like structures which are driven and expanded into the stenotic artery to restore blood flow perfusion to the downstream tissues. Schatz et al. subsequently modified the Palmaz stent, which led to the

development of the first commercially successful stent, the Palmaz–Schatz stent. Puel and Sigwart were the first to implant a stent in human body in March 1986[2].

Nowadays, stent implantation is a common procedure with a high rate of success when compared with angioplasty alone[3]. However, some limitations are still present: for example stent deployment inside an artery has many implications on the stresses and deformations in the arterial wall and hence has an impact on the progression of in-stent restenosis. In-stent restenosis is defined as the recurrence of stenosis after a stenting implantation due to neointimal hyperplasia, that is the thickening of the inner layer of the blood vessel as an effect of an abnormal growth of the vascular tissue. The smooth muscle intimal hyperplasia is the ending of a process which consists of various phases, including a thrombosis phase, an inflammatory phase, a granulation or cellular proliferation phase, and a final critical phase of remodeling. Also balloon angioplasty induces a cascade of events that begins with endothelial denudation and culminates in vascular remodeling after a significant phase of smooth muscle proliferation, but the placement of endovascular implants introduces a stimulus of far greater magnitude[14].

It has been shown that configuration-dependent interactions of stent struts with the vessel wall, to a greater extent than arterial enlargement or stent surface material, determine vascular injury and neointimal hyperplasia[4]; this means that the structure of the device and its interaction with the vessel greatly influence the response of the intervention.

2. Analyses techniques

The knowledge that the design and therefore the interactions of the stent with the vascular walls are strictly linked to the success of the implantation that has prompted researches to focus on the stresses and the deformations generated during the expansion of the device. The issue has been addressed both with *in-vitro* experiments and computational simulations.

In particular computational structural analysis has emerged in recent years to investigate the mechanical response to angioplasty and stent placement in the arterial wall. Up to now most studies have concerned the stent behavior and its expansion, or the vessel-stent interaction.

Depending on the aim of the analysis the computational studies have focused on different aspects of the stent expansion and have developed several models of the vascular

environment: Lally et al. elaborated an idealized vessel and plaque geometry to compare the stresses generated by two commercial stents[5]; Gijssen et al. reconstructed a mildly stenosed coronary artery by using a combination of biplane angiography and intravascular ultrasound in order to mimic the *in-vivo* behaviour[6]; Migliavacca et al. concentrated on the modeling of a drug-eluting stent to quantify the stress field in the vascular wall, the tissue prolapse within the stent struts and the drug concentration at any location and time inside the arterial wall[7], in this case the vessel and plaque were modeled with an ideal geometry; as a final example Rogers et al. used a finite element analysis to model how balloon-artery contact stress and area depend on stent-strut geometry, balloon compliance, and inflation pressure[8]. This last study also concerned an *in-vivo* and *ex-vivo* analysis that examined the superficial injury during deployment of stents to show that balloon-induced damage can be modulated by altering stent design. The advantages of testing a computational model are the possibility of changing the characteristics and the parameters (e.g. material or geometry) without the necessity of setting a new experimental system, this reduces costs and allows preliminary tests on devices which need to be optimized before experimental testing. As the finite element method does not include all the complexities associated with the natural environment, physical experiments can also be performed in order to complete the knowledge about a specific object.

As regards the experimental approach, many studies have been undertaken to examine the *in-vivo* and *in-vitro* behaviour of biological vessels and synthetic phantoms. The advantage of using an experimental test is that the real physiological conditions can be better reproduced and arteries maintain their complex mechanical properties, whilst in computational simulations the assumptions made to build the model can cause a loss of realism.

During *in-vivo* analyses the biggest difficulty is reaching the target of the study and obtain information about the reactions to the stenting procedures. As a solution to this problem Carrozza et Al. [15] used a continuous ultrasound imaging (IVUS) during stepwise balloon inflation and deflation with an imaging core positioned within the guidewire lumen of the balloon in order to quantify the stent recoil phenomenon and its effect on stent failure. To assess the impact of the stent symmetry on restenosis Schulz et Al. [16] implanted 30 slotted tube stents in healthy sheep and after euthanasia they performed an histological evaluation on the area of interest. To correlate restenosis with stent geometry

quantitative *in vivo* angiography was made with an automated edge detection system to measure the diameters of the vessel and of the balloon during the expansion.

In vitro studies have used different techniques to understand the mechanics of blood vessels and stents. For instance Zhou et Al. [17] quantified the longitudinal haemodynamic force in a stent-graft model under pulsatile flow conditions by bonding strain gauges on the main trunk. The gauges were connected to a Wheatstone bridge circuit. Another application of strain gauges as a measurement instrument was performed by Flora et al. [18] who used high-elongation foil strain gauges to examine the strains and stress on three latex abdominal aortic aneurysm phantoms in a pulsatile flow model. The aim of the work was to determine the relationship between wall mechanics and risk of failure.

Nevertheless the use of strain gauges and contact methods interferes with the mechanical properties of the vessel or stents, causing imprecision in the result. For this reason non-contact methods have widely spread in the last years because of their capacity of detecting the vessel behaviour without introducing additional deformation or reinforcing the wall structure. Optical methods have gained a particular success for their flexibility and simple usage together with good results, both in biomedical research and in other fields. Applications of photogrammetry for stent analysis include Wang et al. [19] who designed an experimental system based on machine vision technology for *in vitro* stent expansion to investigate the expansion behaviour of a balloon-expandable stent. The system used a CCD camera, an image acquisition device and LabVIEW measurement software for strain calculation. Other examples of optical measurement methods are reported in the State of the Art.

This study focuses on the use of a stereoscopic optical method for the detection of strain on a three-dimensional surface, like a tensile strip or stented vessel. In particular the stereo set-up is implemented within a virtual software environment to allow its accuracy to be examined in detail.

3. Report structure

The *Introduction* section has examined the field of interest of the present work. In particular the stent implantation methodology and the related problems have been illustrated and a brief excursus on the strain measurement technique on soft tissues has been reported.

The *State of the art* section focus on the knowledge already achieved about the photogrammetric systems and the previous works which have used the same technique investigated in this study. A chapter is dedicated to an alternative optical technique, the image registration, and to the softwares which have been used during the project. Finally the aims of the thesis are declared.

The *Material and method* describes the evaluation process applied to the photogrammetry, the procedures employed to derive the strain measurements and the sets of trials made to investigate the system. The protocols are divided by geometry and include the preliminary tests made to examine the set-up parameters and the principle tests whose aim was to quantify the accuracy of the optical technique.

The *Results* chapter reports the numerical and graphic results of the preliminary and main tests described in the previous part. Also this section is divided by geometry and the comments are provided with references to the *Appendices* where all the values have been stored into tables.

The *Discussion* includes the description and comments to the results reported in the previous section. In particular, the remarkable values are highlighted and the response of the system is analysed in detail. The structure of the discussions follow the division by geometry.

Finally the *Conclusion* section collects the observations made above and formulates an overall view on the system behaviour. The potential sources of error detected by the tests are summarized and some developments are suggested as a continuation of the actual study in the *Future work* chapter.

State of the art

1. Photogrammetry

A photogrammetry imaging technique is a non-contact method which involves the use of two or more cameras each acquiring 2D images of an object from different points of view to enable the reconstruction of the surface in three dimensions. From the 3D coordinates it is possible to calculate the strains of the surface at successive step of object deformation.

Optical methods like the photogrammetry are currently considered to be the best option for 3D strain measurement on visible soft tissues because they do not interfere with the mechanical behaviour of the specimen and are suitable in case of the large deformations often observed with biological materials.

Particularly interesting is the use of stereoscopic vision which is based on the fundamental principle of human vision and stereoscopy. From a pair of images, it is possible to compute the 3-D coordinates of a physical point by triangulation assuming that [20]:

1. the geometry of the stereo rig (e.g. the relative position and orientation of the two cameras) is known. This problem is solved by a camera calibration procedure;
2. it is possible to match two image points p_1 and p_2 , that is identifying the two nodes as corresponding to the same physical point P; this is called the stereo-matching problem and it is performed by using a reconstruction method [21].

An example of a stereovision set-up is shown in Figure 4.

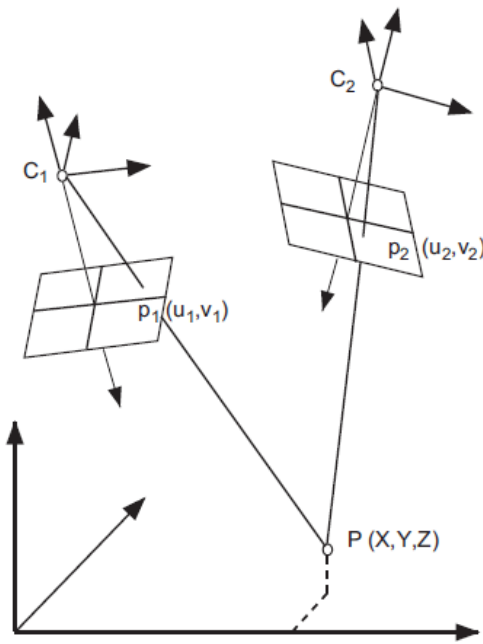


Figure 4 Stereovision set-up

An application of stereoscopic measurement in the biomedical field is the study made by Lujan et al. [22]: in this paper the strains of a stretching ligament were recorded with two high-resolution digital cameras and calculated using dedicated software to assess the precision and accuracy of the optical method. The ligament was marked by contrast markers positioned in a grid and the coordinates of the markers were used to calculate the displacement of the tissue. Moreover, the accuracy of kinematic measurements was assessed by simulating the measurements required for recording knee kinematics.

Gao et al. [23] used stereoscopic photogrammetry to study the motions of a bioprosthetic heart valve leaflet mounted in a bench flow circuit. One leaflet of a trileaflet bovine pericardial valve was marked with ink dots forming a matrix and subsequently recorded by two CCD cameras through an optical window designed to facilitate the BHV imaging. The markers' coordinates and the surface of the valve were reconstructed using triangulation and surface-fitting algorithms.

Photogrammetry is not only applied to dual stereovision, in fact more than two cameras can be used to capture object motions. Narracott et al. [24] implemented an experimental six CCD camera system with camera axes oriented radially at positions of equal separation around the circumference of a circle. This circular set-up was used to examine the symmetry of *in-vitro* stent expansion and includes a detailed section on the camera calibration.

This study aims to deepen the knowledge about the accuracy of a stereoscopic camera set-up and is based on previous work by Katherine Goude and Iwona Zwierzak, MSc and PhD students in the Cardiovascular Science department, University of Sheffield, who both concentrated on a photogrammetry system for the detection of soft tissue deformations.

Katherine Goude [10] developed a software framework to perform stereoscopic reconstruction and strain measurement, allowing images to be acquired by either physical stereo camera setup or by virtual methods. The virtual approach was chosen and the ANSYS finite element package was used to model a virtual object and provide geometry and strain reference data; a chessboard texture was integrated with the object surface to allow automated identification of reference points. The modeled object was then imported in a virtual stereo camera rig and experiments were performed to evaluate the performance of the stereoscopic strain measurement technique.

The innovation of this study was the use of OpenCV functions developed for automatic object reconstruction. This algorithm is based on the identification of reference points which are represented by the corners of a checkerboard pattern. This procedure significantly improves the time of the manual reconstruction and allows analysis of more extended areas.

Another relevant aspect of this study is the possibility to create and import geometries in a virtual environment which reduces the costs of time and money related to an experimental approach.

The results of this study demonstrated that the stereoscopic reconstructions derived from the virtual geometry effectively captured relative position and displacement of the virtual object. The error in relative positions of object points was small (0-12.6 μm ; mean 2.6 μm) and consistent between calibrations, with small variations across the curved surface of the object. However reconstruction of absolute object position varied widely between calibrations. Each calibration introduced significant systematic geometric errors (up to 355 μm). As strain is derived from relative locations and displacements of reference points, this large systematic effect did not influence accuracy of strain calculations.

This project evaluated reconstruction algorithms to identify dominant factors responsible for compromising the derived strains. Though the automatic detection technique has not been applied to practical trials yet and is far from the actual experimental problems.

In order to consider the issues related to an experimental set-up the work by Iwona Zwierzak has been taken into account [9]. The aim of this experimental study was to explore a photogrammetric optical imaging method used to describe the local variation of strain in an elastic material undergoing large deformation (strip geometry). The material under investigation was marked with reference points and imaged with two stereoscopically positioned cameras during a tensile test. The cameras were calibrated using the Bouguet calibration toolbox in Matlab to characterize their optics and establish their positions. The deformation of the elastic material was determined by 3D reconstruction of the deformed geometry, in detail the tridimensional position of every marker was obtained from the 2D single images. Strain results derived from Matlab were compared to manual measurements performed with the use of a caliper. Camera calibration and reconstruction accuracy results indicated an uncertainty of dot separation of the order 30 μm , with inter-point distance of approximately 3 mm.

The Figure 5 show the specimen under investigation.

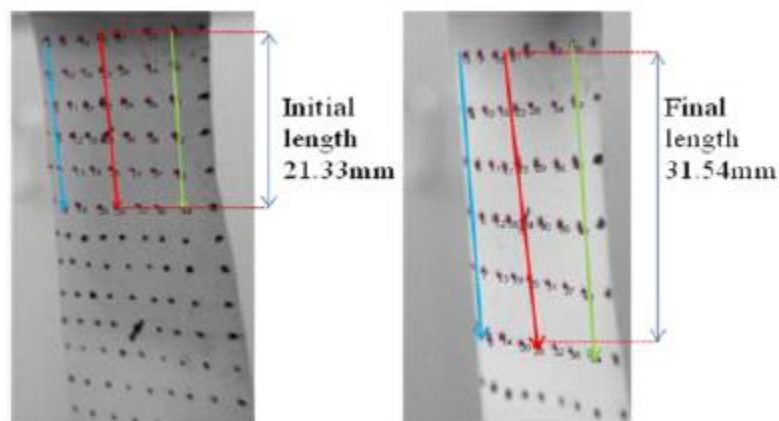


Figure 5 Strain measurement of an elastic sheet

The optical technique showed potential for development to investigate local strain variation in elastic biological materials, though a better comprehension of the sources of error was needed. In particular a characterization of the local vessel wall strain was recommended to provide a deeper understanding of the strain variation during stent deployment.

To simulate the same experimental condition the Bouguet calibration toolbox and the manual detection of points for reconstruction were used in the current study.

2. Image registration and Digital Image Correlation

Image registration has widely spread during recent years as an optical technique and an effective method of image analysis. Image registration has been used in the research community since the early 1980s and takes a number of different forms [25]. Image registration is the process of overlaying images of the same scene, captured at different times, from different viewpoints and/or by different sensors [26].

Typically, registration is required in remote sensing (multispectral classification, environmental monitoring, change detection, image mosaicking, weather forecasting, creating super-resolution images, ..), in medicine (combining computer tomography (CT) and NMR data to obtain more complete information about the patient, monitoring tumor growth, treatment verification, comparison of the patient's data with anatomical atlases), in cartography (map updating), and in computer vision (target localization, automatic quality control).

Its application can be divided into four main groups according to the manner of the image acquisition:

- *different viewpoints*: images of the same scene are acquired from different viewpoints;
- *different times*: images of the same scene are acquired at different times. The aim in this case is to find and evaluate changes in the scene which appeared between the consecutive image acquisitions. This methodology is the one used mostly for medical imaging;
- *different sensors*: images of the same scene are acquired by different sensors;
- *scene to model registration*: images of a scene and a model of the scene are registered.

Nevertheless, the majority of registration methods consists of the following four steps:

- *feature detection*: distinctive objects are manually or automatically detected;
- *feature matching*: the correspondence between the features detected in the sensed image and those detected in the reference image is established;
- *transform model estimation*: type and parameters of the mapping functions, aligning the sensed image with the reference image, are estimated;
- *image resampling and transformation*: the sensed image is transformed by means of the mapping functions.

Because of its importance in various application areas and because of its complicated nature, image registration has been the topic of much recent research. This includes use the use Digital Image Correlation (DIC) for the analysis of displacement fields between images of a deformed geometry.

One of the important aims of DIC is its potential use for strain measurement, in fact current strain gage technologies are only able to offer a limited number of discrete measurements, which often is not enough. Tension tests have been conducted on steel plates allowing measurements from the DIC technique to be compared to measurements from conventional foil strain gages. The potential sources of DIC strain measurement error have been analyzed and, in this case, the most significant is the out-of-plane motion. After having found suitable solutions it was possible to achieve mean strain errors of less than $5\mu\text{m}$ that are less than the error introduced with the strain gage measurement [27].

Another potential source of error is the impact of a non-perpendicular camera alignment to a planar sheet metal specimen's surface. This problem has been solved with a 3D DIC stereo configuration of cameras that induces a substantial compensation for the introduced image-plane displacement gradients [28].

Various studies have been conducted in the medical field. One of the most interesting examples used a stereomicroscope system adapted to make accurate, quantitative displacement and strain field measurements on mouse carotid arteries. Experimental results demonstrated that the microscope system with three-dimensional digital image correlation successfully measured the full 3D displacement and surface strain fields at the micro scale during pressure cycling of 0.40 mm-diameter mouse arteries, confirming that the technique can be used to quantify changes in local biomechanical response.

In modern medicine, digital subtraction angiography is a powerful technique for the visualization of blood vessels in a sequence of X-ray images. A serious problem encountered is misregistration of images due to patient motion. In one work a new approach to the registration of digital angiographic image sequences is proposed, based on local similarity detection by means of template matching according to combined invariants-based similarity measure and on thin-plate spline image warping in order to correct patient motion artifacts [29]. Another work discusses use of a suitable motion model for respiratory motion correction in cardiac imaging [30].

3. Virtual methods

Among all the illustrated works regarding the vessel-stent interaction and the surface strain analyses two softwares have been selected and applied in the current study. In particular the tests have been performed by using a combination of finite element analysis software (ANSYS 12.0) and computer-generated image rendering software (Realsoft3D).

3.1 ANSYS

ANSYS is a finite element analysis package that provides a means to model an object under deformation and stress. ANSYS includes a wide range of capabilities depending on the kind of analysis required, for example electromagnetic or fluid dynamic or structural. In this case the ANSYS 12.0 Mechanical APDL platform was used (Figure 6).

In order to set up a simulation the object firstly needs to be defined as a plane or solid geometry; then the model is divided into a mesh of elements identified by a set of nodes and element connectivity. At this stage boundary conditions are applied to the object to simulate an applied force or displacement and generate a strain. Finally ANSYS calculates the strain across the geometry and these results are used as a gold standard strain reference for result comparison.

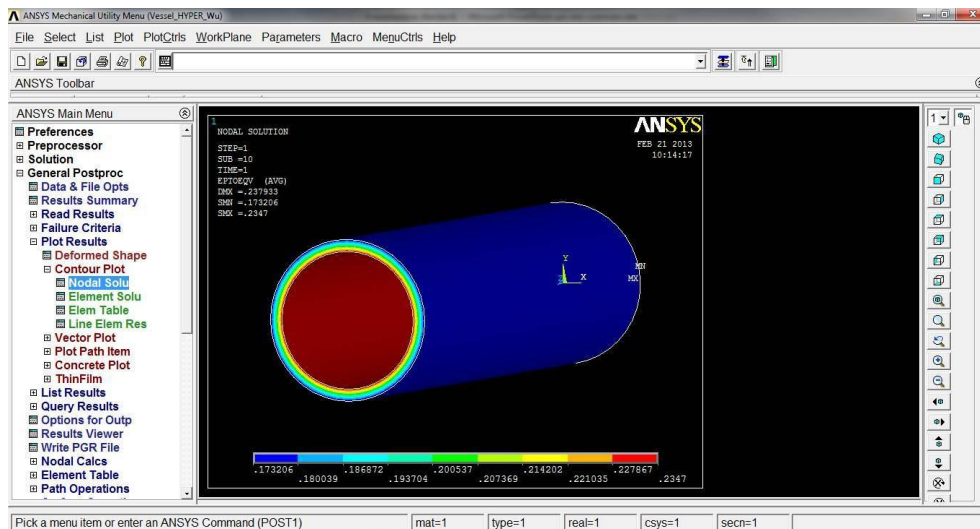


Figure 6 ANSYS is a finite element analysis package used to define a virtual object, apply a simulated force and calculate the strain

3.2 Realsoft 3D

Realsoft 3D (7.0) is a modelling and ray tracing application capable of simulating physical objects and rendering the virtual scene captured by one or more cameras. A realistic experimental camera setup can be modelled with this software and saved to file; all the

typical parameters of a camera can be set up for a specific test (e.g. focal length, field of view and focusing distance). Regarding applications in the field of interest the virtual system is capable of replicating the process performed with a physical camera rig during a strain experiment on a given surface (Figure 7).

In a real stereo-camera system calibration is needed, in fact cameras are placed in the tridimensional space but the knowledge of the exact relative positions is required in order to perform a reconstruction of the captured objects. Calibration can be obtained by importing chessboard objects at different positions in the field of view.

The objects to be imaged can be modelled directly in Realsoft or by using a Javascript code; the second approach is more convenient in terms of flexibility since the parameters can be easily changed and a new geometry implemented.

Once that the desired camera setup and the object are both loaded into Realsoft 3D then the scene is rendered from each camera to create the image files. The rendered images can then be saved in different formats and with different levels of resolution.

This software is particularly interesting for the purpose of this study because it provides a simple yet powerful platform to build and perform a virtual experiment, hence different aspects of the photogrammetry method can be analysed without a high request of time and funds. Though the scene recreated in Realsoft3D does not present some of the phenomena that occur in the real tests, like lens distortion and light reflection, that usually cause problems during the surface reconstruction.

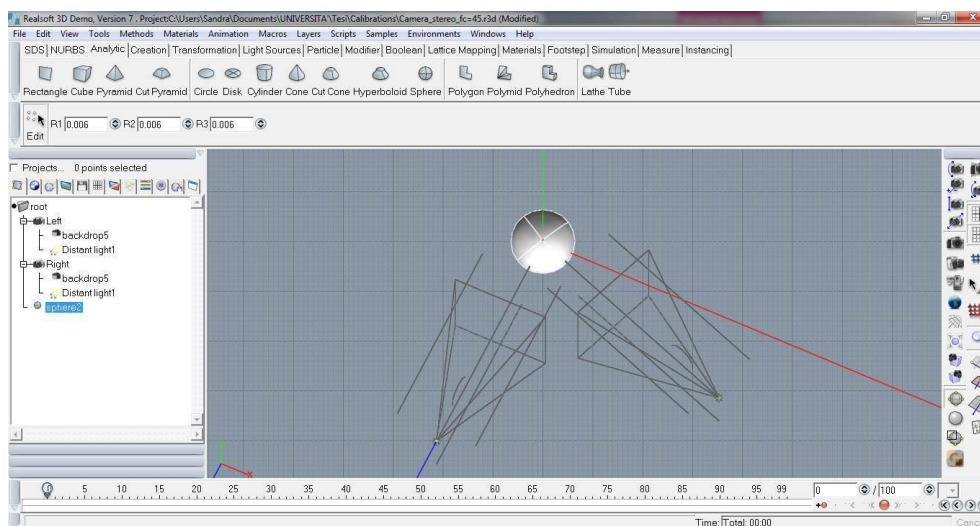


Figure 7 Realsoft 3D is a modelling and ray tracing program allowing specification of virtual cameras, modelling of virtual object and rendering of a scene from each camera.

4. Current project

4.1 Description and aims

The purpose of this work is to evaluate a stereoscopic method for surface strain measurement by means of the finite element (FEM) method and a virtual reality platform. In fact all the tests were performed with a virtual camera set-up in order to reduce the amount of time and funds required for an experimental *in-vitro* analysis and the data were compared with ANSYS simulations, taken as gold standard methods. The results of the study aim to determine the accuracy of the technique independent from experimental error sources (e.g. lens distortions or refraction) and to assert the possible future applications of this method.

The practical use of this technique is provide the accuracy value of the stereophotogrammetry for calculating the strain on the external surface of stented vessels for people will use this approach for *in-vitro* experiments.

The project intends to combine the potential of computational simulation with the complexity of the experimental reality. In fact the FEM results are used as a gold standard to compare the strains obtained with the photogrammetric technique but the difficulties related to an *in-vitro* test are taken into consideration because the process of surface reconstruction and data analysis reproduces Zwierzak's approach [9].

Furthermore, the virtual reality environment provides great flexibility and allows easy changes in the parameters of the camera rig to test the system under different conditions.

The technique has been tested with three geometries to gradually move towards a more realistic model: a strip, a vessel and a stented vessel. Also the material properties have been varied to understand the sensitivity of the system to different tissue behaviours.

A strip geometry was used to obtain preliminary knowledge of the technique and to perform trials to assess the accuracy. The effect of image resolution on the reconstruction error and the effect of reconstruction noise on the final strain measurement have been studied. Different formulas for the calculation of the strain have been evaluated through a comparison with the ANSYS data and the approximations introduced by the strain theory have been underlined. Once the preliminary phase was concluded the process of image capture, reconstruction and data analysis was applied to determine the accuracy and the

possible sources of error. In addition a zero strain test was performed to quantify the error introduced by the manual reconstruction of the surface. In parallel to the manual approach an Image Registration approach was proposed as a method to decrease the error on the nodal position data.

As regards the vessel and the stented vessel a preliminary mesh sensitivity test was carried out to detect the mesh which best optimised the computational time and an accurate ANSYS solution. In the stented vessel case changes to the element formulation were necessary to resolve the bending effects due to the stent structure. Once that the element formulation and the number of elements were confirmed the same strain measurement technique illustrated in the previous section was carried out and the data was compared with the FEM solution.

Materials and methods

1. Evaluation process

The process that has been used to evaluate the stereoscopic strain measurement technique (Figure 8) is based on the work of Goude [10] with the substantial difference that in this case a manual reconstruction of the analysed surface was carried out to simulate a real *in-vitro* approach.

The method consists of several steps, these are illustrated in the diagram shown in Figure 8. Initially, research was conducted to determine the geometry and the material properties of the objects under study, depending on the previous studies made in the same field of interest.

Once the object properties were chosen an input file was written to define the ANSYS geometry, loads and boundary conditions and post processing of the data. A virtual stereo camera set-up was defined in the Realsoft3D software, a program for virtual reality and object rendering; the system was calibrated using a set of checkerboards and a Matlab-based calibration toolbox. The position of object nodes was extracted from the ANSYS results and these values were converted using Matlab code to generate a JavaScript file with the geometry of the object at every step of deformation. The surface of the object was characterised by a checkerboard design implemented to easy detect the nodes; the grid pattern was generated following the element mesh set in the ANSYS simulation. At this point the JavaScript files were imported into the Realsoft3D camera rig and the images from the left and right camera were captured, replicating a real stereo camera experiment.

Subsequently the images were treated in two different ways: in the first case the pictures are loaded in Matlab and reconstructed with a manual function requiring hand-picking of points of interest; the second method applied image registration to extract the node coordinates at each step of deformation.

Finally the position values were used to calculate the surface strains and the data are compared with the computational results, which are considered to be the gold standard for this test. If this difference is below a threshold, the technique was considered validated, otherwise a check of the parameters of the virtual camera system and of the FEM model was performed in order to correct possible sources of error.

In addition an evolution of the geometric and material properties was undertaken to better approximate the biological complexity of real tissues and gradually approach the experimental reality.

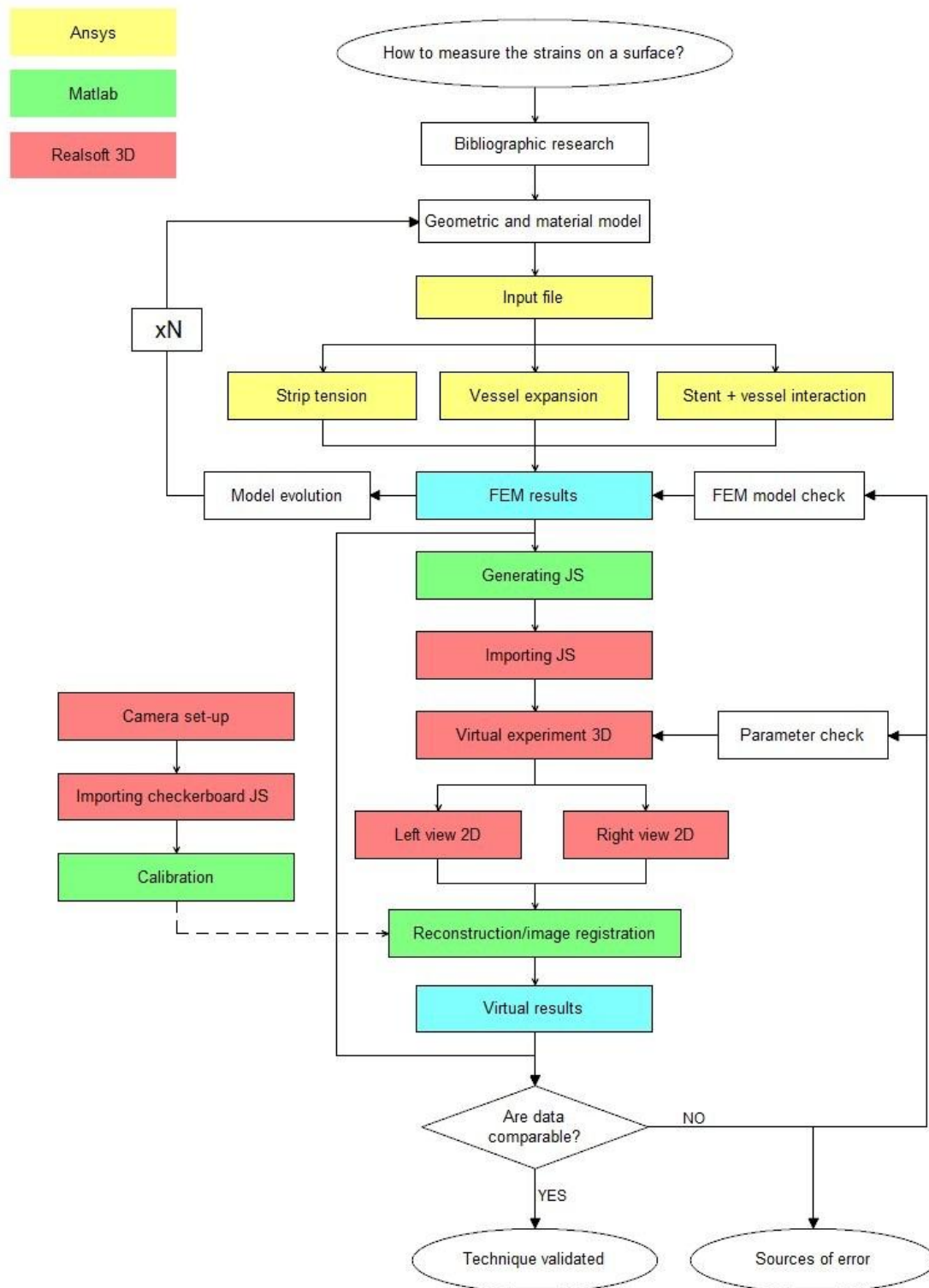


Figure 8 Process to evaluate the stereoscopic strain measurement technique

2. Geometric models

In order to test the technique under different conditions and examine if the geometry influences the results, various geometric models have been developed and tested. The Table 2 reports the reference for each configuration.

Table 2 Geometry configuration tested

Geometry	Name
Strip	A
Vessel	B
Stented vessel	C

2.1 Strip

A strip consistent with the work of Goude [10] and Zwierzak [9] was defined. An ANSYS input file was written to define a planar strip with a width of 11mm and a length of 25mm (Figure 9).

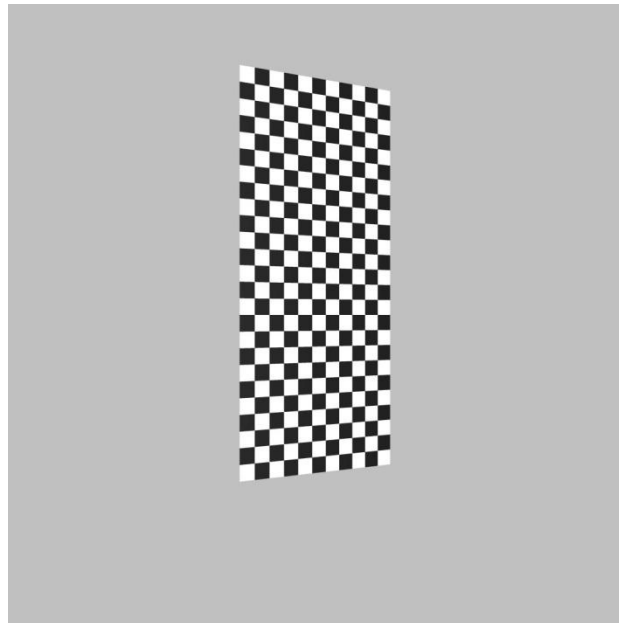


Figure 9 Strip geometry

The strip was aligned with the ANSYS global coordinate system without any rotation to the $x/y/z$ axis and the thickness of the sample in the z direction is ignored.

2.2 Vessel

In order to obtain a realistic geometry of a coronary vessel, experimental images were used to measure a porcine coronary artery, this data was provided by Iwona Zwierzak. The artery was taken from a pig heart provided on the same day as the test: the vessel was roughly separated from the rest of the organ with a bistoury, a perpendicular section was

obtained and placed on a plate under the camera set up. The coronary was not completely cleaned of the muscle which naturally surrounds the vessel *in vivo*, this did not influence the measurement as the outline of the lumen was clearly visible due to the difference in tissue composition.

The measurement was performed using a single camera with focal length $f_c = 31.5 \text{ mm}$. A ruler was positioned in the field of view so that calibration of the camera was not necessary because a millimeter reference was already included in the photo. Figure 10 shows the image of the vessel.

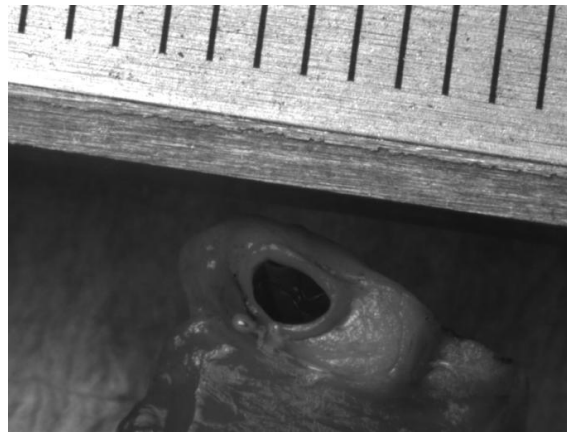


Figure 10 Vessel thickness measurement set-up

Once a clear image of the vessel was captured, vessel geometry was measured using the VIEW software, developed by a student of the University of Sheffield . This program allows measurement of the distance between two points taking as a unit reference the ruler which is placed in the frame of the image. The calibration of this system is made by using a virtual caliper which takes the single spacing of the ruler and associates to it a one millimeter unit. In Figure 11 it is shown the software screenshot.

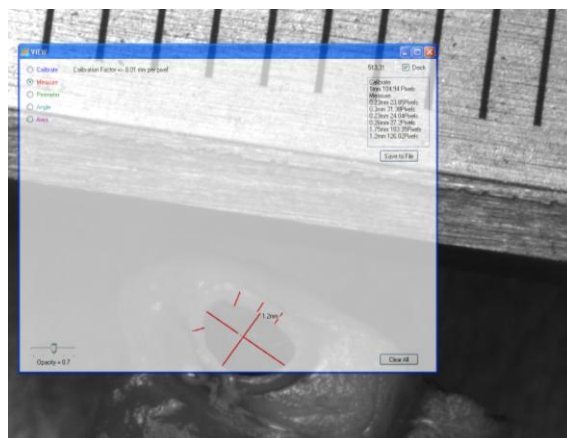


Figure 11 VIEW screenshot

Table 3 reports the measurements of the thickness and of diameter of the vessel.

Table 3 Measurement tests of thickness and the diameter of the vessel

Measurement	Thickness [mm]	Diameter [mm]
1	0.23	1.75
2	0.30	1.20
3	0.23	/
4	0.26	/
Mean	0.26	1.48

The results of the diameter are not particularly reliable since the vessel came from a young animal and there was no internal pressure applied during the test, so the dimensions are underestimated. It can be observed the lumen is circular but elliptic and the reported diameter is the mean between the major and minimum diameters of the section. As regards the thickness the estimated values are comparable to those reported in literature [31] and the measurement is quite constant around the circumference. The final dimension used for the vessel model are summarised in Table 4.

Table 4 Vessel geometry dimensions

Dimension [mm]	
L	13.00
r_{in}	1.00
r_{out}	1.26
t	0.26

The diameter value has been corrected taking under account the underestimation due to the age of the animal and the change in the tissue after the death. The new value of radius has been taken according to some literature studies on the vessels' anatomy [31].

These parameters were used to define a three-dimensional model of the vessel in its unexpanded configuration using the ANSYS finite element package.

2.3 Stent

The stent examined in this study is a coronary stent with applicator, similar to the MAC4 design. The stent proEngineering model was provided by the Laboratory of Biological Structure of Politecnico di Milano.

In the unexpanded configuration the stent is assumed to be a sequence of repeated rings linked by V-shape connectors and each ring is formed by five identical units in the circumferential direction. In this model only two rings of the stent are analysed. The

structure is assumed to be symmetric in the axial direction, except for the ends part circled in red: this difference is due to the fact that not the whole stent geometry is used in the analyses, but only the first two links. The initial length, inner and outer diameters are respectively equal to 3 mm, 1.25mm and 1.5mm (Figure 12).

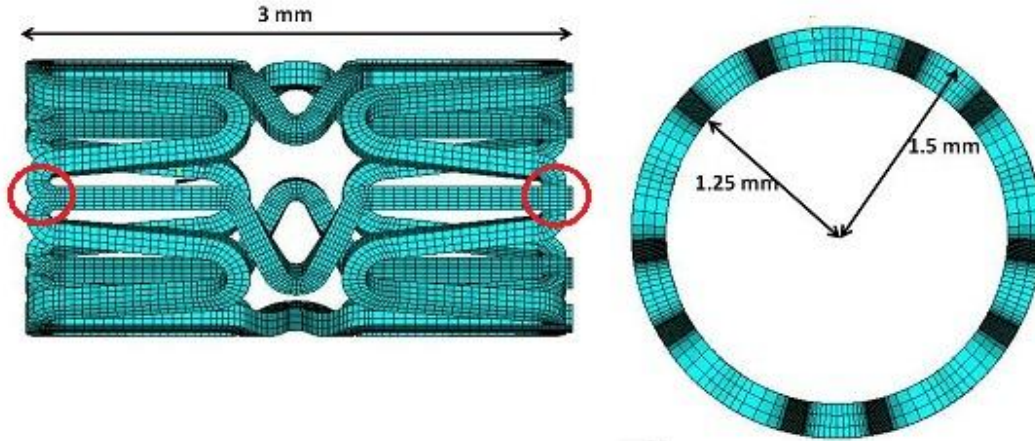


Figure 12 Stent dimensions: length, inner and outer diameters

The material used was an elastic stainless steel and its behavior is described by a bilinear isotropic hardening using the following parameters (Table 5). The element used to build the geometry was SOLID185.

Table 5 Stent bilinear isotropic hardening material parameters

Stent material parameters	
Elastic modulus	209 GPa
Poisson ratio	0.3
Yield stress	450 MPa
Tangent modulus	2000 MPa

2.4 Balloon

In order to simulate balloon inflation a cylindrical rigid area without thickness was created with length 3.5 mm and radius 0.63 mm and a radial displacement was applied to the nodes of the balloon's mesh.

3. Material models

Several material models were applied to the strip and the vessel to simulate different mechanical properties and determine how the system reacts to a change in mechanical behaviour.

3.1 Isotropic linear elastic

Linear elastic behaviour is described by the Hooke's law which defines the relation between stress (σ) and strain (ε):

$$\sigma = E\varepsilon$$

where E is the elastic Young's modulus. This value is related to the substance's tendency to deform elastically and, in particular, it determines how much an object deforms along an axis when forces are applied along that axis.

The material also deforms in the direction transverse to the loading axis and the shear modulus expresses the specimen's attitude of undergoing lateral strain. The shear modulus G is defined as:

$$G = \frac{E}{2(1 + \nu)}$$

where ν is the Poisson's ratio which defines the tendency of the material to compress when subject to a force. If the ratio is equal to 0.5 the material is considered to be incompressible.

The material is isotropic when the response to loading is the same independent of the direction of application, the Young's modulus is the same in all loading directions.

In this study two ANSYS linear elastic models were implemented and applied to the different geometries. Both models are based on literature references (Goude [10] and Chua et Al. [12]). The material characteristics are reported in Table 6.

Table 6 Linear elastic material properties

Material	1	2
Young's modulus [MPa]	1.00	1.75
Poisson's ratio [/]	0.49999	0.49000

3.2 Isotropic hyperelastic

In order to obtain more realistic material behaviour an isotropic hyperelastic material law was considered using the 3-parameter Mooney-Rivlin constitutive formulation.

Hyperelasticity is the capability of a material to experience large elastic strain without losing its original properties. An hyperelastic material has a non-linear behaviour, which means that its deformation is not directly proportional to the load applied and the stress-strain relationship derives from a strain energy density function [32].

Mooney and Rivlin proposed a strain energy function as an infinite series in powers of $(\bar{I}_1 - 3)$ and $(\bar{I}_2 - 3)$. For example, the Mooney-Rivlin 3-parameter form, used in this study is [33]:

$$\psi = C_{10}(\bar{I}_1 - 3) + C_{01}(\bar{I}_2 - 3) + C_{11}(\bar{I}_1 - 3)(\bar{I}_2 - 3) + \frac{1}{d}(J - 1)^2$$

where \bar{I}_1, \bar{I}_2 are the strain invariants of the principal stretches of the strain tensor, C_{10}, C_{01}, C_{11} are material constants and d is the material incompressibility parameter. The change of energy is due to the deformation which takes place so ψ is assumed to be zero in the reference configuration and to increase with deformation.

The constants used in the present work have been taken from literature [13] where a different notation was used. In particular $C_{10} = C_1, C_{01} = C_2, C_{11} = C_3$ and $d = C_4$. The applied parameters are summarised in Table 7.

Table 7 Hyperelastic material properties

Material	3
C_1 [MPa]	0.020
C_2 [MPa]	0.003
C_3 [MPa]	0.175
C_4 [MPa]	0.090

4. Camera set-up

The parameters of a single lens optical system are the object distance u , the sensor distance v and the focal length f_c . The sum of the object distance and the sensor distance is the focusing distance d . Figure 13 illustrates the camera parameters.

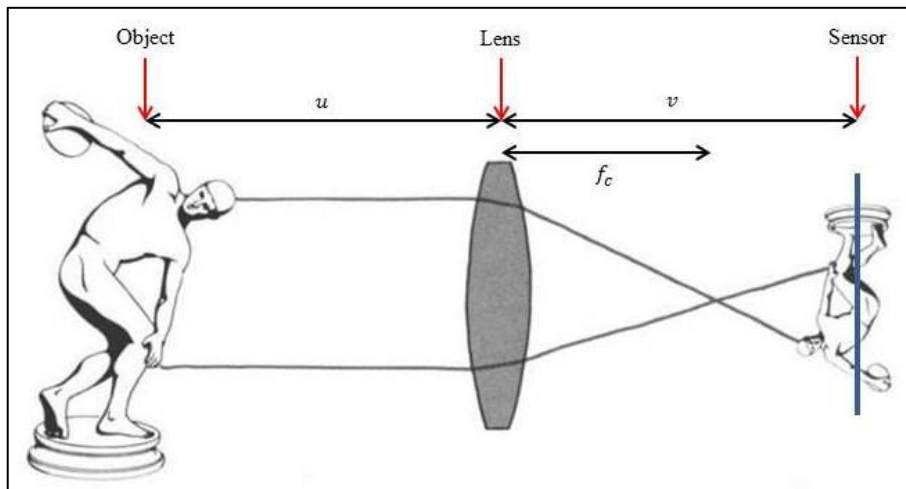


Figure 13 Parameters of a single lens optical system

For an object to be in focus on the camera the relationship between u , v and f_c must satisfy the lens equation:

$$\frac{1}{f_c} = \frac{1}{v} + \frac{1}{u}$$

$$M = \frac{v}{u}$$

where M is the magnification of the system. The hypothesis under this system is that the distance v is equal to the focal length, in fact the focal point is corresponding to the sensor position.

$$M = \frac{u}{v} = \frac{u}{f_c}$$

The Realsoft3D software illustrated in the State of the Art chapter was used to create the virtual stereo camera rigs used in this study. The program enables to choose between many system parameters, leading to a virtual configuration that best approximates a real camera. The following values were set up to build the framework:

- camera position x, y, z in the Realsoft3D coordinate system;
- aimpoint which is the point camera is directed to (always at 0,0,0);
- focal length f_c ;
- sensor width s_w and height s_h ;
- light sources:
 - type (point, ambient, distant, spot,...);
 - position x, y, z ;
 - intensity.

An example of stereo camera set-up is shown in Figure 14:

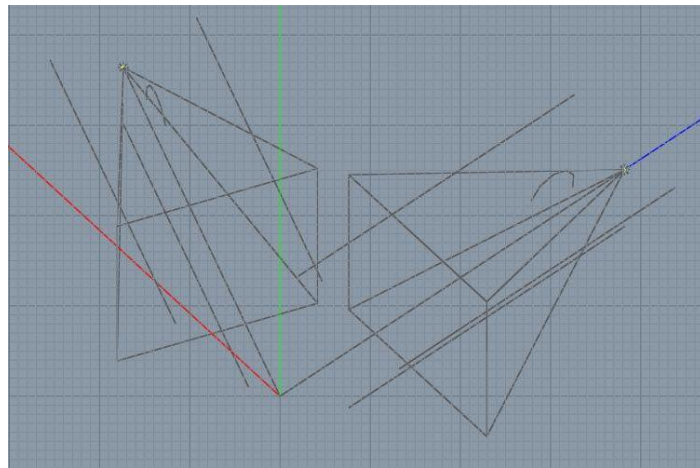


Figure 14 Realsoft 3D stereo camera set-up

Several stereo camera set-ups were created using Realsoft 3D to study different aspects of the photogrammetric technique. The following table summarises the applied parameters:

Table 8 Applied parameters of stereo set-ups camera

Set	Camera	s_w [mm]	s_h [mm]	f_c [mm]	Angle view [°]	d [mm]	x [mm]	y [mm]	z [mm]
1	Left	30	30	38	43.08	50	0	0	50
	Right	30	30	38	43.08	50	47	0	17
2	Left	30	30	70	24.19	50	0	0	50
	Right	30	30	70	24.19	50	47	0	17
3	Left	30	30	45	36.87	50	0	0	50
	Right	30	30	45	36.87	50	47	0	17
4	Left	5	4	31.5	9.08	150	0	0	150
	Right	5	4	31.5	9.08	150	75	0	130
5	Left	5	5	31.5	9.08	150	0	0	150
	Right	5	5	31.5	9.08	150	75	0	130
6	Left	5	5	31.5	9.08	105	0	0	105
	Right	5	5	31.5	9.08	105	53	0	91
7	Left	5	5	60	4.77	105	0	0	105
	Right	5	5	60	4.77	105	53	0	91
8	Left	5	5	60	28.07	90	0	0	90
	Right	5	5	60	28.07	90	45	0	78
9	Left	5	5	60	4.77	45	0	0	45
	Right	5	5	60	4.77	45	22	0	39
10	Left	30	30	60	28.07	90	0	0	90
	Right	30	30	60	28.07	90	78	0	45

The eight and tenth camera set-ups are particularly relevant because they were used for the main tests performed respectively on the vessel and strip configurations.

In order to prevent the reflections on the object captured with the camera, a light set-up was created, composed of three ambient lights (Table 9).

Table 9 Light source project specifications

Light source	1	2	3
Intensity	0.300	0.300	0.300
Falloff radius [mm]	100	3	3
Shadow casting	no shadow	no shadow	no shadow
x [mm]	23	23	23
y [mm]	0	-10	10
z [mm]	87	87	87

5. Calibration

Calibration is the process used to determine the exact orientation in space and the parameters of a set of cameras. Calibration data must be obtained in order to perform reconstruction and compute by triangulation the tridimensional coordinates of a point captured by two cameras. Calibrating a stereo camera system requires determination of the intrinsic and the extrinsic parameters of the camera set-up.

The extrinsic parameters define the location and orientation of a camera reference frame with respect to a known world reference frame or the relative transformation between two camera reference frames. In this study the extrinsic parameters identify the translation vector (T) between the relative positions of the origins of the two reference systems and the rotation vector (R) that brings the corresponding axes of the two frames into alignment (Figure 14).

$$T = [T_x \ T_y \ T_z]$$
$$R = [\theta_x \ \theta_y \ \theta_z]$$

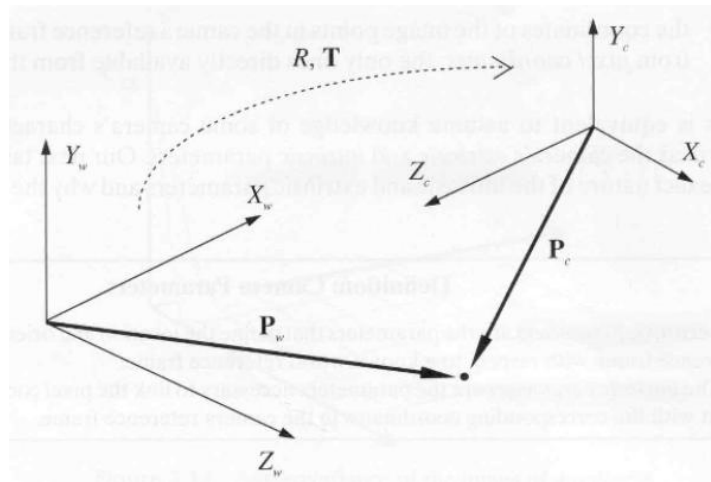


Figure 15 Translation (T) and rotation vector (R) linked two different frames

The intrinsic parameters are those necessary to link the pixel coordinates of an image point with the corresponding coordinates in the camera reference frame. In particular they characterize the optical, geometric and digital characteristics of the camera:

- the perspective projection or focal length f ;
- the transformation between image plane coordinates and pixel coordinates;
- the geometric distortion introduced by the optics.

The example of a camera aimed at a point in space is reported in Figure 16. The image plane is the plane on which the point is projected and it is normal to the optical axis of the

camera. It is along the respective optical axes that the z direction of the local camera coordinate system is defined.

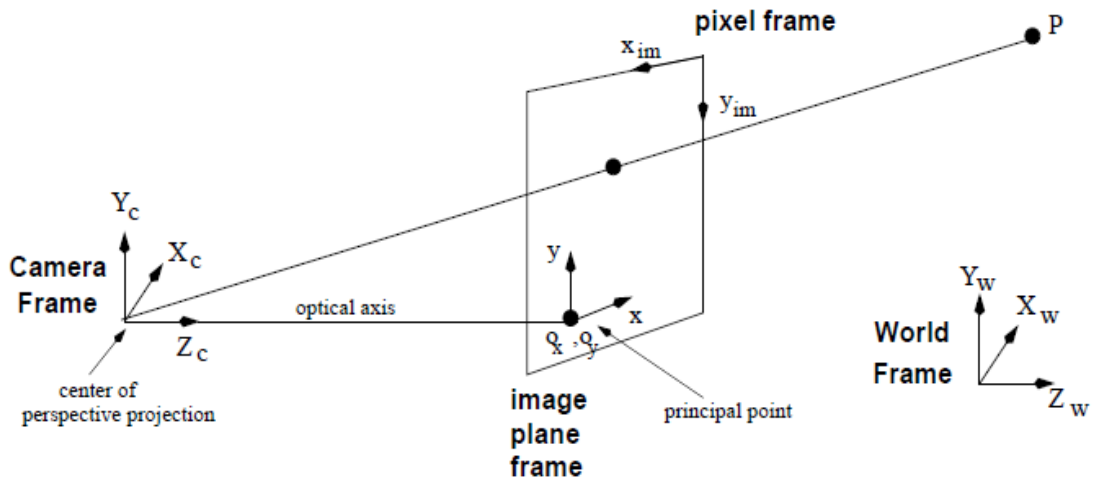


Figure 16 Camera aiming to a point in the space

The relationship between the camera coordinates and the image plane coordinates is the following:

$$x = f \frac{X_c}{Z_c} \quad y = f \frac{Y_c}{Z_c}$$

where f is the focal length, $X_c Y_c Z_c$ are the coordinates in the image plane and $x y z$ are the camera frame coordinates. To transform the image plane coordinates into pixel coordinates $(x_{im} y_{im})$ it is necessary to apply the formula:

$$x_{im} = -\frac{x}{s_x} + o_x \quad y_{im} = -\frac{y}{s_y} + o_y$$

where $o_x o_y$ are the coordinates of the principal point in pixels and $s_x s_y$ correspond to the effective size of the pixels in the horizontal and vertical directions in millimeters.

If the principal point is the center of the image the principal point can be expressed as a function of the horizontal and vertical number of pixels (N and M) which compose the image:

$$o_x = \frac{N}{2}$$

$$o_y = \frac{M}{2}$$

Finally the image can have distortions due to the optics of the camera, for example, related to the lens curvature. The two main types of distortion are radial and tangential which can be characterised using polynomials to describe the geometric perturbation. Radial

distortion can be defined by three parameters (k_1, k_2 and k_3) and tangential distortion can be corrected using two further parameters (p_1 and p_2). The relationships between the distorted and the corrected coordinates (x_d, y_d, x_c, y_c) are different for the radial and the tangential distortions, respectively:

$$\begin{aligned} x_c &= x_d(1 + k_1r^2 + k_2r^4 + k_3r^6) & y_c &= y_d(1 + k_1r^2 + k_2r^4 + k_3r^6) \\ x_c &= x_d + [2p_1y_d + p_2(r^2 + 2x_d^2)] & y_c &= y_d + [2p_2x_d + p_1(r^2 + 2y_d^2)] \end{aligned}$$

where $r = \sqrt{(x_d^2 + y_d^2)}$

The calibration method used in the present work is the Matlab calibration toolbox developed by Bouguet [11]. In Bouguet's calibration technique, several images of checkerboards in various positions are captured by each camera simultaneously and then loaded into Matlab. Usually the checkerboards are captured by a physical camera system, but in this case the checkerboard images were derived from JavaScripts objects imported in the virtual camera rig implemented with Realsoft3D. The checkerboards were moved as much as possible in the field of view, in order to cover the range of angles viewed by the two cameras. All the calibrations were performed using a set of eleven checkerboards rotated with respect to the y axis and translated along the x and y axis (Figure 17). Since different camera configurations presented different focal lengths and fields of view, several checkerboard sets were implemented to better fit the field of view and provide a good calibration in all directions. Table 10 summarises these sets of checkerboards.

Table 10 Checkerboard sets' features

CB set	A	B	C	D	E	F	G	H	I	J
Square size[mm]	2	2	2	1	1	1	0.5	0.25	2	3
θ_{y_min} [°]	0	0	0	-10	-20	-30	-30	-30	-5	-5
θ_{y_max} [°]	70	70	30	40	50	60	60	60	65	65
Δy_{min} [mm]	0	-3.5	-2	-4	-4	-4	-2	-1	-12	-10
Δy_{max} [mm]	0	3.5	2	4	4	4	2	1	12	10
Δx_{min} [mm]	0	0	0	-3	-3	-3	-1.5	-0.75	-12	-10
Δx_{max} [mm]	0	0	0	3	3	3	1.5	0.75	12	10

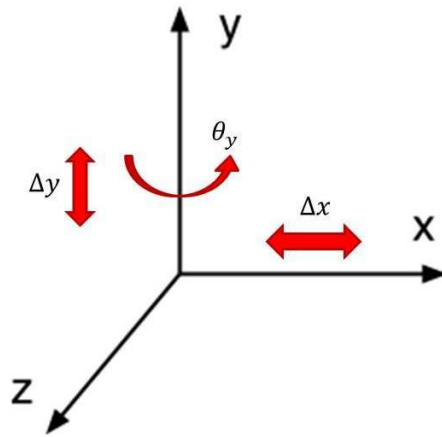


Figure 17 Possible translations and rotations of the checkerboards in the 3D space

The Figure 18 shows an example of calibration checkerboards.

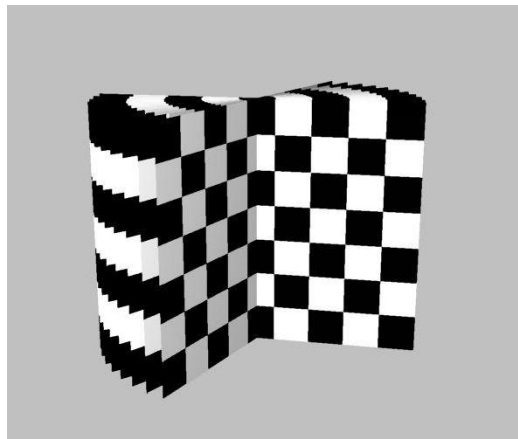


Figure 18 Calibration checkerboards

The extreme corners of each checkerboard pattern were located manually with four mouse clicks, the toolbox then locates the corners of internal squares of the checkerboard. At this point other options can be selected to improve the results of the calibration, such as changing the value of the radial distortion coefficient such that the internal squares can be located more accurately [34].

Once the corners have been extracted for all right camera and left camera images, the algorithms in the toolbox calibrate each camera separately and then as a stereo pair. The stereo calibration for a pair of cameras produces one set of extrinsic parameters (vectors R and T in millimeters) and a set of intrinsic parameters for each camera. The resulting intrinsic parameters include:

- focal length in pixels stored in the 2x1 vector f_c ;
- principal point coordinates in pixels stored in the 2x1 vector cc ;

- skew coefficient defining the angle between the x and y pixel axes stored in the scalar $alpha_c$;
- the image distortion coefficients (radial and tangential) stored in the 5×1 vector k_c .

Figure 19 depicts a graphical representation of the extrinsic parameters produced by a stereo calibration.

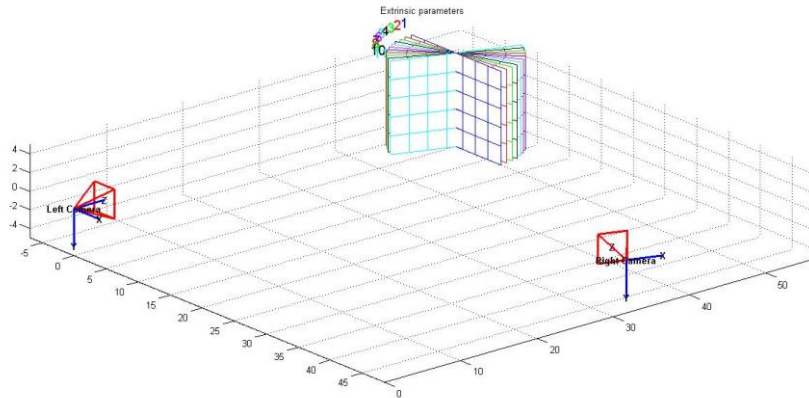


Figure 19 Extrinsic parameters image from Calibration Toolbox

The table below reports all the calibrations executed during the project:

Table 11 Calibrations realized

Calibration	Stereo set up	CB set	Resolution
1	1	A	1020X1020
2	2	A	1020X1020
3	2	A	1200X1200
4	2	B	2400X2400
5	3	B	2400X2400
6	4	C	2400X1796
7	5	C	2400X2400
8	6	D	2400X2400
9	6	E	2400X2400
10	6	F	2400X2400
11	7	G	2400X2400
12	8	G	2400X2400
13	9	H	2400X2400
14	10	J	2400X2400

The expected calibration parameters can be estimated by applying the relation illustrated some pages above to the parameters set in the virtual camera rig. For example set-up number ten represents two cameras divided by an angle of 60° , with images captured at

2400x2400 pixel resolution. Given this configuration the expected calibration parameters are:

$$f_x = f_y = 60 \left(\frac{2400}{30} \right) = 4800$$

$$o_x = o_y = \frac{2400}{2} = 1200$$

$$k = [0,0,0,0,0]$$

$$T = [78,0,45]$$

$$R = [0,60,0]$$

6. Reconstruction

In a stereo photogrammetric system the object of interest is captured by two cameras fixed at different angles to the object and a pair of two-dimensional images is produced. Reconstruction is the process using this pair of images to provide the tridimensional coordinates of a specified point. To obtain a correct tridimensional reconstruction the calibration parameters of the rig must be known. In fact the information related to the single camera and to the images are expressed in pixels while the results of the reconstruction are given in millimeters.

Reconstruction is divided into two stages called correspondence and triangulation. The first step is the process of identifying matching points on the images from both cameras and it is performed with the help of an epipolar line. Subsequently the triangulation stage converts pairs of two-dimensional pixel locations into three dimensional physical locations using the camera calibration parameters.

The correspondence and triangulations processes are based on the principles of stereoscopic vision and photogrammetry theory (Figure 20). When an object is projected onto the image plane the pixel coordinates are immediately known but the point could have any position along the projection line ($x_1, x_2, x_3 \dots$). If the same object is also projected on the image plane of another camera with a different angulation, then the two projection lines intersect at the correspondence point on the object and define its 3D position.

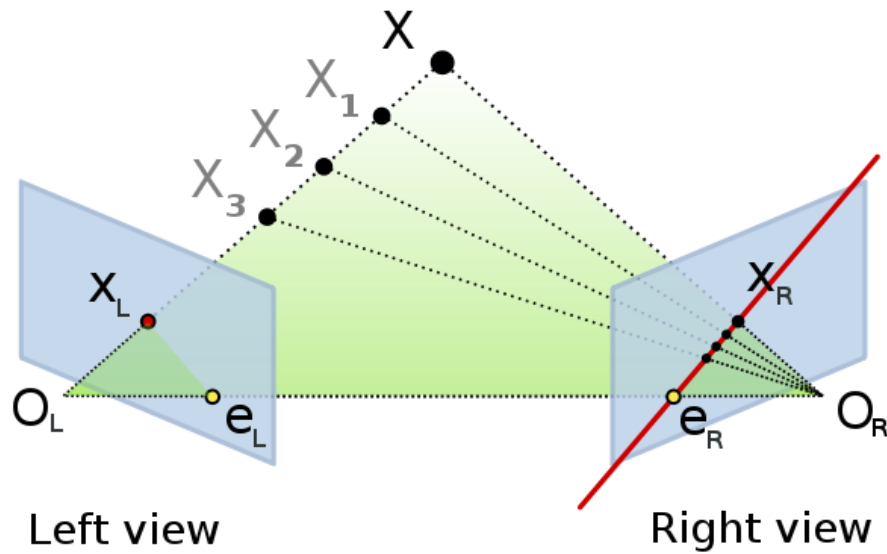


Figure 20 Triangulations processes based on the stereoscopic vision and photogrammetry theory

The right epipolar line is defined as the connection $e_R - x_R$ between the projection x_R of the object on the right image plane and the correspondent epipolar point e_R . The epipolar point is the projection of a center of projection (in this case O_L) on the other's camera image plane. Similarly, the epipolar line on the left image is defined as $e_L - x_L$. All epipolar lines in one image must intersect the epipolar point of that image. In fact, any line which intersects the epipolar point is an epipolar line since it can be derived from some 3D point X .

The epipolar line is important in the reconstruction process because if the position of the point is unknown, manual picking can be performed on one image (left) and subsequently the same point has to be detected on the corresponding image along the epipolar line, which provides support for correct point correspondence.

The reconstruction can be carried out as a manual process where the points of interest need to be selected by hand clicking or it can be applied as an automatic function. In this study the manual approach was used because the experiments are still carried out by performing a manual selection of the nodes on the surface.

The reconstruction approach followed within the present study is based on the code implemented by Jonathan David Hughes at the University of Leeds [35]. This code allows free selection of a point on one of the two images previously captured, then the correspondent second image appears and an epipolar line is drawn to assist the selection of the matching point. Once that the same point has been picked on both images the pixel

coordinates get stored in a matrix and the user can select a new point. When all the desired points have been picked the triangulation is applied and two sets of tridimensional coordinates from the left and right camera reference are given. The point picking is a manual process and the triangulation function is performed using the calibration data previously imported. This code was previously used to identify the centre of circular areas on an image using a center of gravity approach. In this study the code was modified to better select points on the edge of uniform area. In addition a zooming option was included to permit manual picking at a finer level.

7. Image registration

In this study image registration has been explored as a mechanism to provide the position of points at the final step of the test under examination. This provides a possible alternative to the manual methods described in the previous section. The focus of this study has not been to develop a new image registration technique, rather existing software has been applied to the data collected during this study. This software is referred to as the Sheffield Image Registration Toolkit (ShIRT), developed in Sheffield by Prof. David Barber and Prof. Rod Hose. Theoretical detail of the algorithms used in ShIRT has been previously published [36] and the following section provides an overview of the key concepts underlying the image registration technique in the context of this study.

The fundamental process of the image registration (IR) is to relate corresponding points in two images. If the coordinates of a point in one image are (x, y) and the coordinates of the same point in the second image are (x', y') , a mapping function can be defined to retrieve the coordinates of the second point from the coordinates of the first point. The relation between the coordinates in each image can be written as:

$$x' = u(x, y) + x$$

$$y' = v(x, y) + y$$

with the aim of the IR algorithm to compute the mapping function (u, v) for every point. In ShIRT the mapping function is defined at discrete points (nodes) in x and y [40]. Before doing the registration a mask can be applied to identify the region of interest in the image which reduces the computational cost of the registration. The mask can be of any shape and can contain holes.

An example of image registration in the context of this study is shown in Figure 21. Figure c) shows the intensity data from the "fixed" image (red) combined with the intensity data from the "registered" image (green), if the registration was successful, the two images are identical and this results in a yellow image.

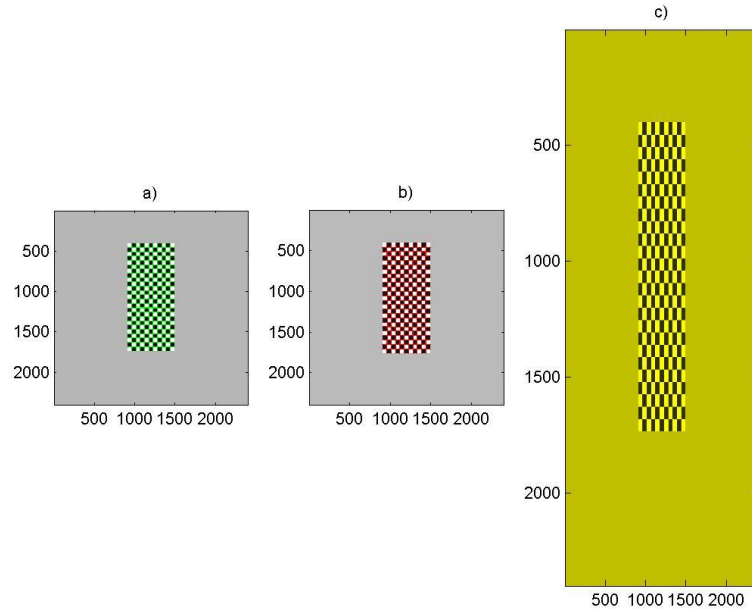


Figure 21 a) green grid points shown on undeformed (fixed) image b) red grid points shown in deformed (registered) image c) combined intensities of fixed (green) and registered (red) images

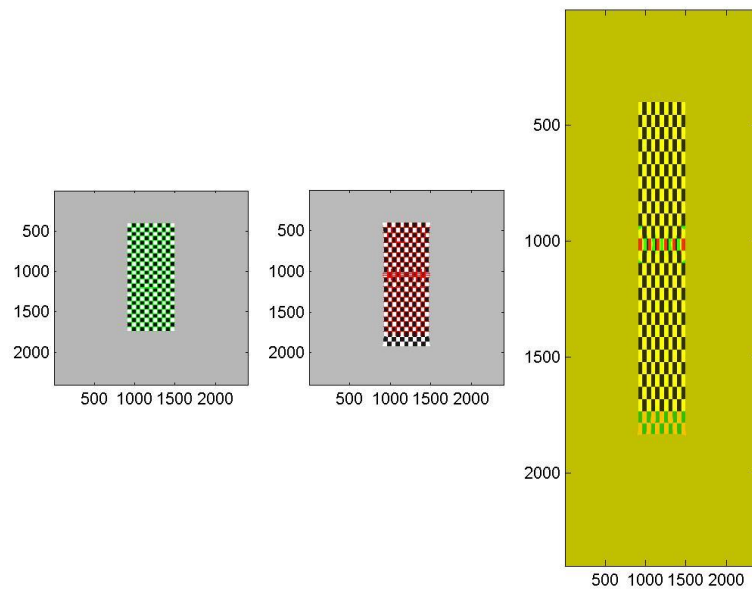


Figure 22 Example of grids overlapped with fixed and registered images after failed registration

Registration can fail if the displacement between the two images is too large. Figure 22 shows a case where the registration has not been completely successful and in the combined intensity image there are green and red marks where the fixed and registered images do not correspond.

To sort out this issue there are several possibilities but some common methods include:

- smoothing of images: in cases where registration of unsmoothed images may not be accurate, image smoothing can be used to reduce fine detail and improve the obtained mapping;
- use of intermediate images: in this case a number of registrations can be run using the existing map as a starting map to obtain a full mapping from the initial image to the final image.

In this work IR is used to determine the displacement of a grid of points. An initial grid is defined overlaid on the fixed image (undeformed shape), in this case the x and y coordinates of the correspondence points identified manually for use with the reconstruction algorithm were used. For each stage of deformation image registration was used to determine the deformed position of this grid of points by computing the mapping between the deformed and undeformed images and applying this mapping to the x and y coordinates of the initial grid points.

The IR process was run separately with left-camera and right-camera images using two .mat files containing the x and y coordinates of the initial grid in both the left and right images. To obtain the x, y and z coordinates of each grid point the triangulation function [34] was applied to the data from each camera view.

8. Strain measurement

Once reconstruction has been performed and the position data have been extracted the strains need to be calculated. To verify the degree to which the strain calculation method influences the accuracy of the process different methods of computing strain have been applied to the same data sets.

8.1 Engineering and true strain

Engineering strain is defined as the ratio of total deformation along a direction to the initial dimension of the same segment in which a force is applied. In the case of a line element

which is axially loaded, with deformed length l , the strain is expressed as the change in length (ΔL) per unit of the original length (L) of the element:

$$\varepsilon_{eng} = \frac{\Delta L}{L} = \frac{l - L}{L}$$

The strain is positive if the material is stretched and negative in compression. However Engineering strain is a small strain measure which is not generally used once the strain in the material becomes large (typically $> 5\%$). True strain, which is a nonlinear strain measure, is used for large strain calculations. In particular, true strain accounts for gradual changes in the geometry by using the instantaneous dimensions of the specimen, giving more accurate measurements for tests like the tensile one. True strain is defined and related to Engineering strain by the following relation:

$$\varepsilon_{true} = \log\left(\frac{l}{L}\right) = \log(1 + \varepsilon_{eng})$$

where l is the final length of the segment. ANSYS calculates strains as true strains, therefore a conversion is needed before comparing with data obtained using an Engineering strain measure.

In the present study the true strain was evaluated by considering two adjacent points using point coordinates extracted from object reconstruction from stereo image data. Given three points in the configuration show in Figure 23 the longitudinal and transversal strains are computed as follows:

$$\varepsilon_y = \ln\left(1 + \frac{\Delta L_y}{L_y}\right)$$

$$\varepsilon_x = \ln\left(1 + \frac{\Delta L_x}{L_x}\right)$$

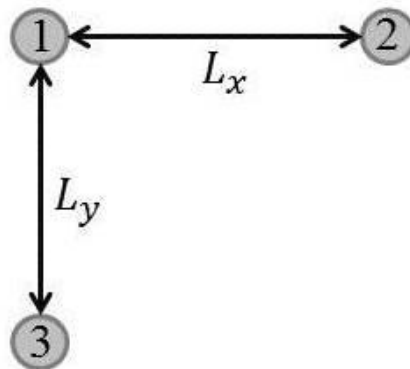


Figure 23 Triplet of points

The true strain calculated using adjacent points is also called Local Strain because it refers to a local region of the material. In the following sections the true strain will always be referred to as Local strain.

8.2 Global strain

In this study Global strain is defined as a measurement of strain estimated from the deformations of points which are not adjacent to each other. In this case the strain is calculated taking the coordinates of two points that cover a more extended area than the Local strain and therefore the final value represents the average strain over a region of the specimen. This measurement may reduce the error on the calculated strain as the averaging approach produces a smoothing of the inaccuracy related to adjacent points. Nevertheless attention must be paid to the degree of averaging as information may be lost to describe the variation of strain within the specimen.

The Engineering transversal strain can be calculated with the relation below:

$$\varepsilon_{x eng} = \frac{\Delta L}{L} = \frac{u_1 - u_2}{x_1 - x_2}$$

where u_1 and u_2 are the transversal displacements of two points in the tridimensional space and x_1 and x_2 are the abscissas of the points at the initial step of deformation.

The Engineering longitudinal strain is instead calculated with the following expression:

$$\varepsilon_{y eng} = \frac{\Delta L}{L} = \frac{v_1 - v_2}{y_1 - y_2}$$

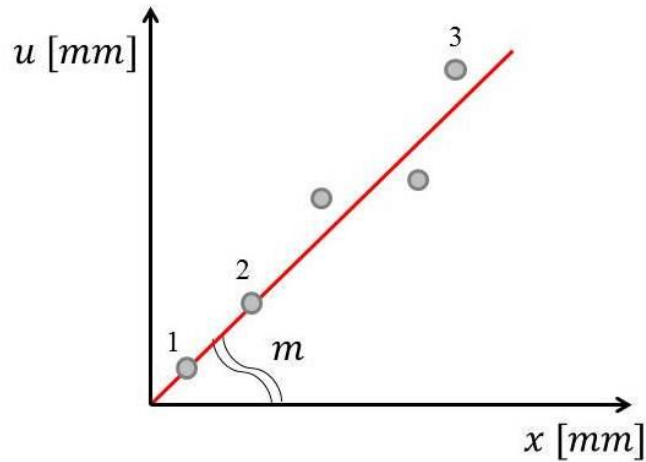
where v_1 and v_2 are the longitudinal displacements of the same two points and y_1 and y_2 are the ordinates of the two points at the same step analysed above.

In particular, for the transversal direction, if the displacements are plotted against the initial position of the corresponding points (Graph 5) the strain measure can be seen to be the slope of the resulting curve:

$$m = \frac{u_1 - u_2}{x_1 - x_2}$$

In this case the resulting value represents Local strain if two adjacent points are used:

$$\varepsilon_{local} = m_{12}$$



Graph 5 Displacement against initial position

To smooth the error associated with reconstruction of individual points a set of nodes can be taken into consideration and the variation of displacement with position can be assumed to vary linearly over the complete set of nodes. The slope of the best fit line corresponds to the average strain of the material over a finite region. For example if all points between 1 and 3 are considered the average value of strain is computed:

$$\varepsilon_{global} = m_{13}$$

The strain extracted with the illustrated method is an engineering strain and to compare the results with the ANSYS solution the logarithmic strain is computed.

$$\varepsilon_{global_true} = \log(1 + m)$$

In the present work the global strain was computed as the slope of the best fit line between three or more points and the logarithmic transformation was always considered. In particular, a test was performed to determine the optimal number of points for which the global approach reduces the error related to reconstruction without significant loss of information of strain variation (as discussed in the Strip test protocol).

8.3 Green-Lagrange tensor

To better account the large deformation and other non-linear effects, the Green-Lagrange tensor has been introduced in the strain calculation. This measurement is an exact measure independent of rigid body motion. The Green-Lagrange tensor is defined as:

$$E = \frac{1}{2}(F^T F - I)$$

where I is the identity matrix and F is the deformation gradient tensor expressed as:

$$F = \begin{bmatrix} \frac{\partial x_1}{\partial X_1} & \frac{\partial x_1}{\partial X_2} & \frac{\partial x_1}{\partial X_3} \\ \frac{\partial x_2}{\partial X_1} & \frac{\partial x_2}{\partial X_2} & \frac{\partial x_2}{\partial X_3} \\ \frac{\partial x_3}{\partial X_1} & \frac{\partial x_3}{\partial X_2} & \frac{\partial x_3}{\partial X_3} \\ \vdots & \vdots & \vdots \end{bmatrix}$$

in which X_i indicates the coordinates in the undeformed configuration and x_i the coordinates of the deformed shape.

In the present study only two directions have been considered to describe the surface strains, transversal and longitudinal for the strip and circumferential and axial for the vessel, so the Green-Lagrange tensor results in a 2 x 2 matrix.

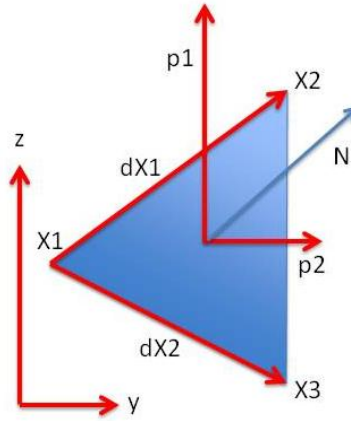


Figure 24 Configuration of vectors to obtain the normal and the tangent lines to the triangular surface. To compute the Green-Lagrange tensor a technique based on triangular domains has been applied to the position data. This procedure is commonly used in biomechanics, for example in the work of Genovese et Al [35] and Everett et Al [36].

Triplets of closely spaced points on the surface are selected to form adjacent triangles until all the object's area is meshed and no nodes are left. Three points define only one plane and this ensures the planarity of the single element. The triplets are described using a matrix which defines element connectivity using the numbering of the surface nodes.

Once that all the surface is divided into triangles the in-plane strain is calculated locally for each element applying the Green-Lagrange tensor. Given a triplet of points (1, 2 and 3) the components of the tensor F are calculated by computing how vectors $dX_1 = X_2 - X_1$ and $dX_2 = X_3 - X_1$ in an undeformed configuration (Figure 24) change to vectors $dx_1 = x_2 - x_1$ and $dx_2 = x_3 - x_1$ in the deformed configuration. By assuming that each flat, triangular

region is small, the associated surface deformation is assumed to be homogeneous $\Delta x \cong F * \Delta X$ [37].

To compare the results with the ANSYS data each component of the Green-Lagrange tensor is transformed into a true strain by applying the following relation:

$$\varepsilon_{true} = \frac{1}{2} \log (1 + 2 * \varepsilon_{Green})$$

9. Strip test protocol

This section describes the protocols applied to the study of the Strip geometry using the methods for object reconstruction and strain evaluation that have been described in the previous sections. A flowchart illustrating the major components of the test protocol is provided in Figure 25.

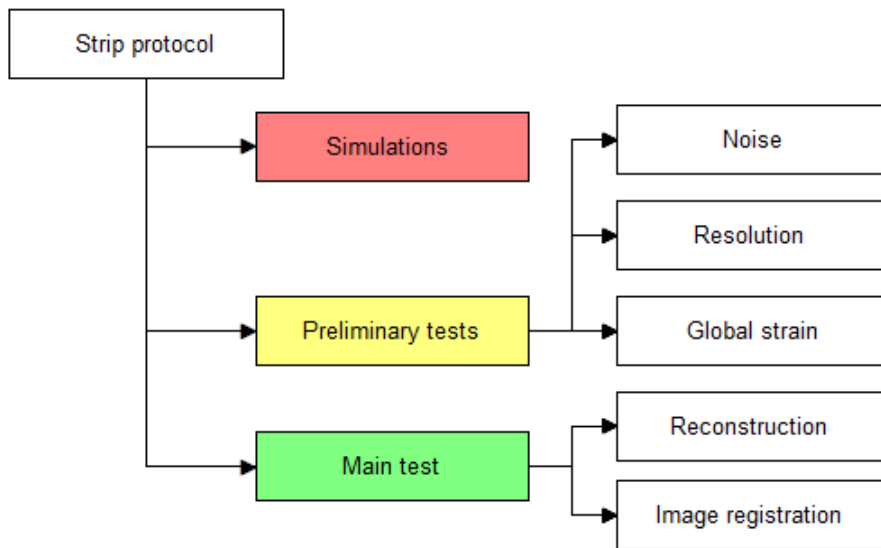


Figure 25 Flowchart illustrating Strip test protocol

9.1 Simulations

On the strip two different ANSYS simulations have been run:

- a vertical displacement of 2.5mm was applied to all the nodes of the strip over ten steps, representing a zero strain test. The element type used is PLANE42;
- the geometry was fixed at the upper boundary and a displacement of 5mm was applied to the nodes at the lower boundary of the strip (Figure 26), applied over ten steps. Element type PLANE42 and PLANE182 were used.

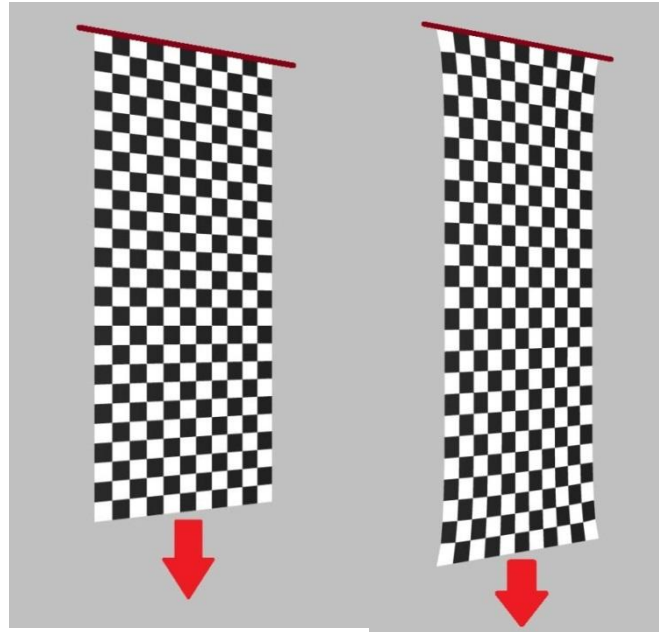


Figure 26 First and last tensile test step

9.2 Noise Test

Table 12 Protocol code

Geometry	Material	Simulation	Calibration	Element
A	1	B	/	Plane42

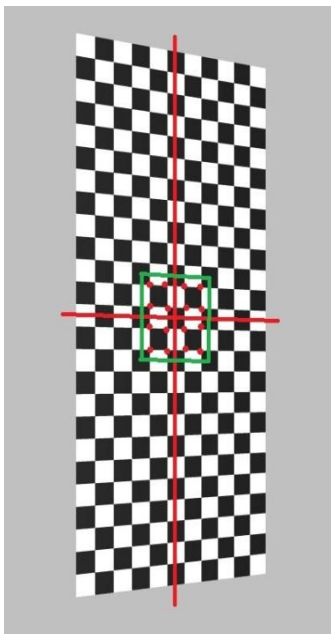


Figure 27 Central points picked for the noise test

To examine how an error due to the manual picking of the points can affect the resulting values of strain a random noise was applied to the ANSYS position data extracted from the tensile strip simulation. For this test (Table 12), the computational coordinates are considered to be the gold standard, therefore generating a random error simulates the error introduced by the manual reconstruction. The propagation of a random position error to the computed strain values was analysed. In addition also the error on the displacement has been evaluated.

The noise was applied to 16 points at the centre of the strip geometry as shown in Figure 27. The positions of the same points were taken from the strip at the beginning of the test (strip001), at the middle instant (strip006) and at the end of the

deformation (strip011). The strains were extracted with the local strain measurement. Since the applied error is random, every test was repeated five times and the mean value of error was reported.

9.3 Resolution Test

Table 13 Protocol code

Geometry	Material	Simulation	Calibration	Element
A	1	B	2/3/4	Plane42

This test (Table 13) was performed to study the effect of image resolution on the reconstruction and data analysis process. The principal issue involved in this trial was the error introduced by a lower resolution compared to the error given by an image containing more pixels.

As before, three object positions were considered, strip001, strip006 and strip011. The same Realsoft3D camera set-up was used to capture the object with three image resolutions: 1020 x 1020 pixels, 1200 x 1200 pixels and 2400 x 2400 pixels.

The 16 points shown in Figure 27 were reconstructed and the reconstruction error provided by the triangulation function was investigated.

9.4 Global strain

Table 14 Protocol code

Geometry	Material	Simulation	Calibration	Element
A	1	B	5	Plane42

The global strain approach (Table 14) was verified by applying the best fit method to a restricted set of points (48 nodes) before analysing the whole geometry. In particular the smoothing of the reconstruction error was the interest of this trial.

This matter was addressed by performing the reconstruction and the strain measurement on two columns along the strip during the middle and final deformation steps (Figure 28). Only the longitudinal strain was calculated because larger displacements take place along the longitudinal axis and possible variations can be evaluated more easily.

If the Global approach is used to average over a large number of points the strain results will not describe possible variations with position due to the excessive averaging used in the fitting process. For this reason the Global strain was calculated on the same data set applying averaging over an increasing number of points (3,4,5 and 6). The aim was finding

the optimal trade-off between smoothing of reconstruction error and preventing loss of information on the strain distribution.

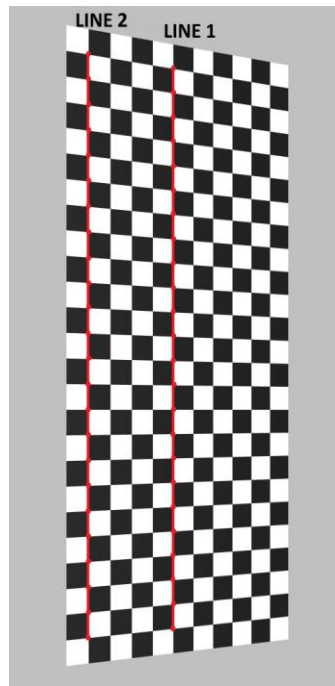


Figure 28 Two column reconstructed for global strain test

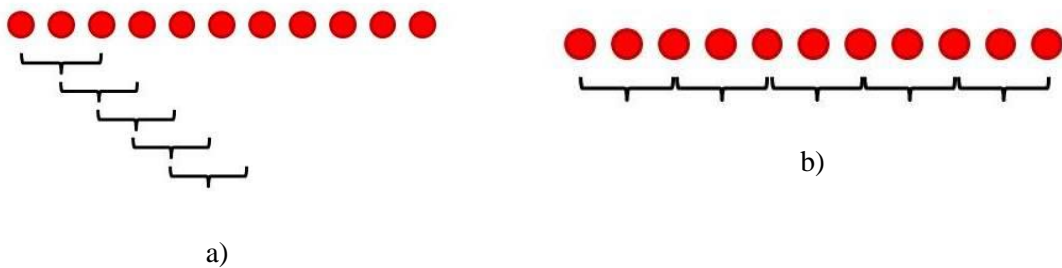


Figure 29 Graphical illustration of method 1 and 2 for Global strain evaluation

Method 1: The strain was obtained by applying a linear best fit to the longitudinal displacement of three adjacent nodes (as shown in Figure 29a). As 24 point locations were available in each column (Figure 28) 22 resulting values of strain were obtained each representing strain at the mid-point of the three nodes.

Method 2: The second method uses three points in series as shown in Figure 29b. In this case 11 resulting strain values were obtained and the last node was not included in the calculation. As the strain is evaluated at the mid-point of each set strain is not calculated at every reconstructed point but every two nodes.

Method 3 and 4: The process is the same as for method 1 and 2, taking five points instead of three. Method 3 refers to the concatenated system and gives 20 values of global strain, while method 4 uses the serial scheme and provides 5 strain values.

9.5 Reconstruction and image registration

Table 15 Protocol code

Geometry	Material	Simulations	Calibration	Element
A	1	b	14	PLANE42
A	2	b	14	PLANE42
A	3	b	14	PLANE182

Once all preliminary tests (Table 15) were concluded the complete virtual stereoscopic process was performed on configurations reported in the table above to evaluate the accuracy and performance of the system.

The nodal coordinates were extracted using two distinct approaches:

- a manual reconstruction of the first and final steps of deformation;
- an image registration of the images captured by the virtual camera rig.

The aim of obtaining coordinates using two different methods is to verify how the data acquisition influences the error on the final strain and whether this inaccuracy might be decreased with new analysis approaches.

The strains were calculated with all the three strain measurements illustrated above: true local strain, true global strain and Green-Lagrange tensor.

9.5.1 Zero strain test

Table 16 Protocol code

Geometry	Material	Simulations	Calibration	Element
A	1	a	14	PLANE42

The purpose of this trial (Table 16) was to quantify the inaccuracy provided by manual point picking. If the geometry is simply translated the expected strains are zero, but due to the reconstruction error on the node positions an artificial strain can result. Zero strain tests have been used to assess strain error magnitude in previous studies (Genovese et Al. [35], Sutton et Al. [38], Smith et Al. [39]).

The same analysis process used for the stretched strip was executed, so two coordinates extraction methods and three strain measurements were obtained.

10. Vessel test protocol

This section describes the protocol applied to the study of the Vessel geometry using the methods for object reconstruction and strain evaluation that have been described in the previous sections. A flowchart illustrating the major components of the test protocol is provided in Figure 30.

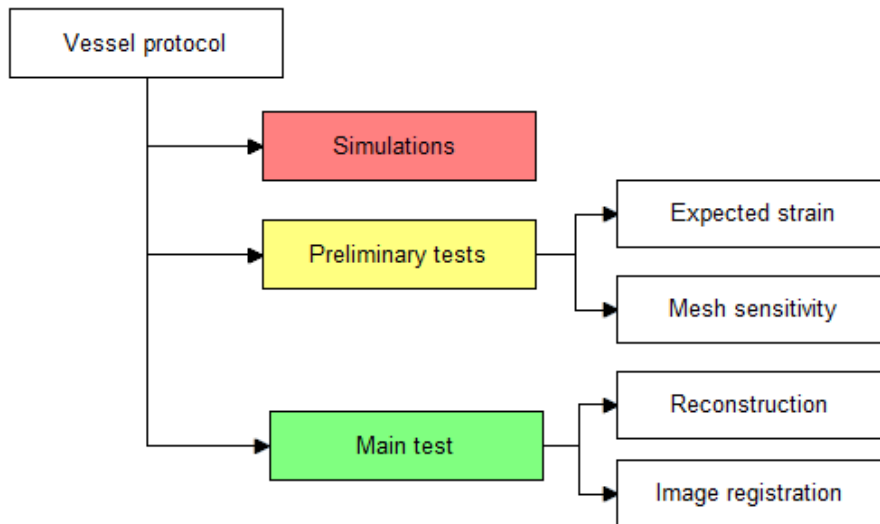


Figure 30 Simulation and test protocol on the vessel

10.1 Simulations

Two ANSYS computational tests were performed on the same geometry using SOLID185 elements, with the same boundary conditions but with different loading conditions. The applied boundary conditions consisted of constraints in the axial and circumferential directions to the nodes belonging to the end of the vessel, to avoid axial displacement and rotation. The run simulations are listed below.

- c) the vessel was expanded using a pressure of 0.016 MPa (120 mmHg) applied to the internal area of the vessel over ten load steps.
- d) the vessel was over expanded by a radial displacement of 0.5 mm, applied to the internal nodes of the vessel over ten steps;
- e) the geometry was over expanded using a pressure of 0.058 MPa (435 mmHg) applied to the internal area of the vessel. This value of pressure was chosen to be sufficient to generate a large circumferential strain, but low enough to provide convergence of the ANSYS simulation.

10.2 Expected strain

In order to evaluate if the ANSYS solution is reasonable and provides correct values of strain, thick-walled vessel theory was used to calculate the expected strains for comparison with the computational simulation. This analysis was undertaken for the parameters specified in Table 17.

Geometry	Material	Simulations	Calibration	Element
B	2	e	/	SOLID185

The simulation was run twice: firstly the non-linearity due to the large deformations was included (NLGEOM,1) and in a second simulation the non-linear option was deactivated so that only the linear response was considered (NLGEOM,0). The results of the linear and non-linear analyses were compared to determine which option better represents the real deformation.

The ANSYS values of strain were extracted from a point on the external surface of the vessel ($r = r_e$) and at the middle length of the cylinder ($l = \frac{L}{2}$) as shown in Figure 31.

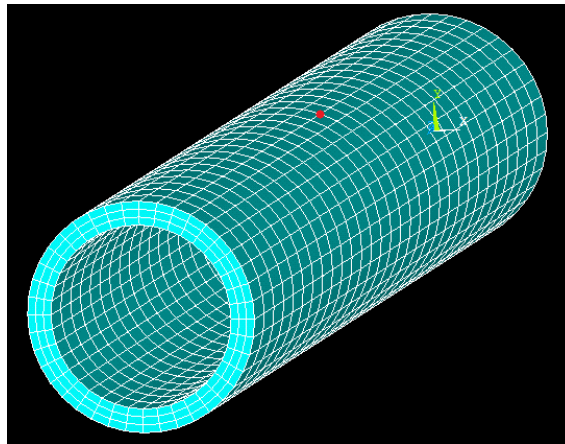


Figure 31 Cylinder used to modelling the vessel in the simulation procedure

The results of the computational trials were compared with strains calculated using thick-walled vessel theory [33]. The vessel was considered to be thick-walled because of the relationship:

$$\frac{t}{2r_i} = 0.13 > 0.1$$

Figure 32 shows the stress components acting on a portion of vessel.

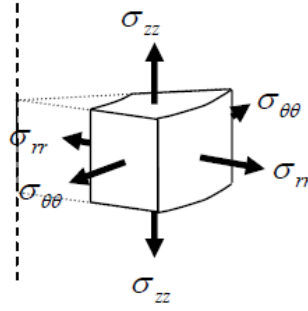


Figure 32 Stress components acting on a infinitesimal portion of vessel

In this study the vessel is loaded with a uniform pressure and subject to plane strain conditions with the following characteristics:

- axisymmetric loading and constraints;
- $\varepsilon_z = 0$;
- $\sigma_z \neq 0$.

The radial stress is given by:

- $\sigma_{rr}(r = r_i) = -p_i$ where p_i is the internal pressure;
- $\sigma_{rr}(r = r_e) = -p_e$ where p_e is the external pressure.

The 3D stress-strain relations reduce to:

$$\varepsilon_{rr} = \frac{(1 + \nu)}{E} ((1 - \nu)\sigma_{rr} - \nu\sigma_{\theta\theta})$$

$$\varepsilon_{\theta\theta} = \frac{(1 + \nu)}{E} ((1 - \nu)\sigma_{\theta\theta} - \nu\sigma_{rr})$$

where $\nu =$ Poisson's ratio

$E =$ elastic modulus

The solution of the equilibrium equations for the cylindrical geometry is:

$$\sigma_{rr} = \sigma_{rr}(r) = -p_i \frac{\frac{r_e^2}{r^2} - 1}{\frac{r_e^2}{r_i^2} - 1}$$

$$\sigma_{\theta\theta} = \sigma_{\theta\theta}(r) = p_i \frac{\frac{r_e^2}{r^2} + 1}{\frac{r_e^2}{r_i^2} - 1}$$

$$\sigma_{zz} = \nu(\sigma_{rr} + \sigma_{\theta\theta})$$

Applying the values of radial and circumferential stresses extracted above to the stress-strain relations it was possible to calculate the values of strain in all directions of the cylindrical coordinate system.

The results of the analytic calculation were then corrected with the true strain formulation, considering that the vessel was subject to large deformations.

$$\varepsilon_{true} = \log (1 + \varepsilon_{eng})$$

10.3 Mesh sensitivity test

The vessel was discretized with different number of elements to assess the influence on discretization on the computational solution. In finite element modelling a finer mesh typically results in a more accurate solution with associated increase in computational time and memory requirements. To find the best trade-off between mesh density, computational time and effort to undertake manual reconstruction, a mesh convergence study was performed on the vessel model using the parameters given in Table 18.

Geometry	Material	Simulations	Calibration	Element
B	2	c	/	SOLID185

The results taken into consideration were the ANSYS strains on the central ring of the vessel. The mesh refinement study was undertaken in two stages as described below:

- create a mesh using a relatively small number of elements and analyse the solution of the model;
- reset the mesh with a denser element distribution in the circumferential and radial direction, compare the results with those of the previous mesh;
- continue increasing mesh density and comparison until the results converge. Convergence is obtained when the results of a simulation differ from the values computed at the gold standard mesh-density less than a fixed threshold;
- once that mesh in the circumferential and radial directions has been chosen, a refinement of the element number in the axial direction was performed.

The mesh parameters used for these tests are reported in Table 19, results and discussion of mesh sensitivity is provided later in this report.

Table 19 First stage mesh refinement in radial and circumferential direction; second stage mesh refinement in axial direction

First stage mesh refinement				Second stage mesh refinement			
Mesh	N axial	N circumferential	N radial	Mesh	N axial	N circumferential	N radial
A	120	40	2	A1	60	40	2
B	120	60	3	A2	120	40	2
C	120	80	4	A3	180	40	2
D	120	100	5				

10.4 Reconstruction and image registration

Following the preliminary tests describe above the complete virtual stereoscopic process was performed on the configurations reported in Table 20 to evaluate the accuracy and performance of the system.

Table 20 Protocol code

Geometry	Material	Simulations	Calibration	Element
B	2	c	12	SOLID185
B	2	d	12	SOLID185
B	3	c	12	SOLID185
B	3	d	12	SOLID185

As for the Strip geometry, the nodal coordinates were extracted using two approaches:

- a manual reconstruction of the first and final step of deformation;
- an image registration of the images captured by the virtual camera rig.

Whilst for the Strip geometry all the nodes were reconstructed, in the Vessel geometry only 190 nodes were picked or registered as only a slice of the whole cylinder can be seen by both cameras using the current stereo camera configuration (Figure 33).

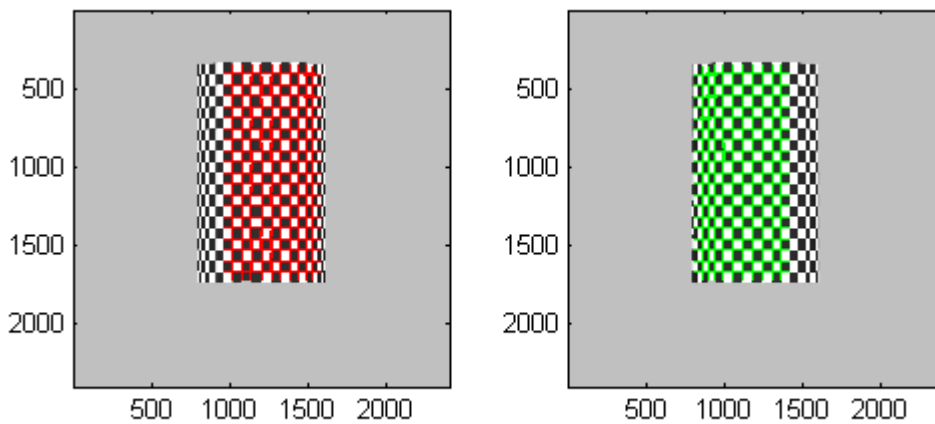


Figure 33 Left and right camera views of cylinder in Realsoft 3D showing region that can be reconstructed.

The strains were calculated with two of the three strain calculation methods measurements illustrated above: the true Local strain and the Green-Lagrange measure. The Global strain approach was not applied to the data because of a problem due to the curvature of the Vessel geometry. Transforming the nodal coordinates from a Cartesian to a Cylindrical reference system presented a difficulty due to a mismatching between them. This mismatching was caused by the calibration procedure, as already underlined in the Goude work [10]. The interpolation of the displacements on the Cylindrical coordinates would have been distorted and the results coming from the Global strain formula would have not been comparable with the values given by ANSYS.

11. Stented vessel test protocol

This section describes the protocol applied to the study of the Stented vessel geometry using the methods for object reconstruction and strain evaluation that have been described in the previous sections. A flowchart illustrating the major components of the test protocol is provided in Figure 34.

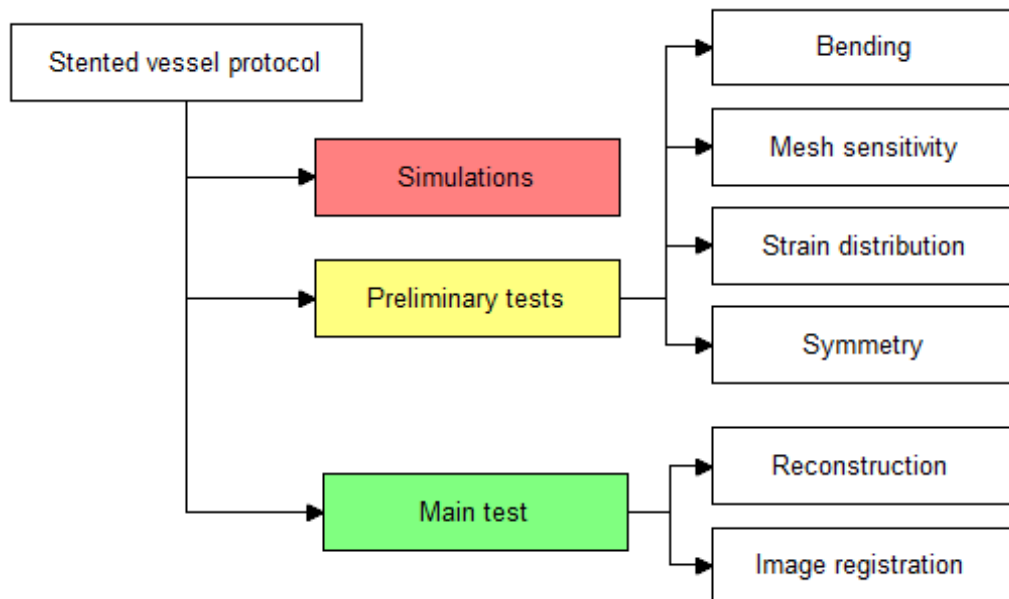


Figure 34 Simulation and test on the Stented vessel

11.1 Simulations

A finite element model of a stent expanded in a vessel by an inflating balloon was constructed in ANSYS 12.0 APDL, as shown in Figure 35. Inside the stent, a cylindrical rigid body was created to simulate the balloon and the vessel was generated as a cylindrical

geometry, as already modelled in the previous analysis, with its center located at the center of the stent.

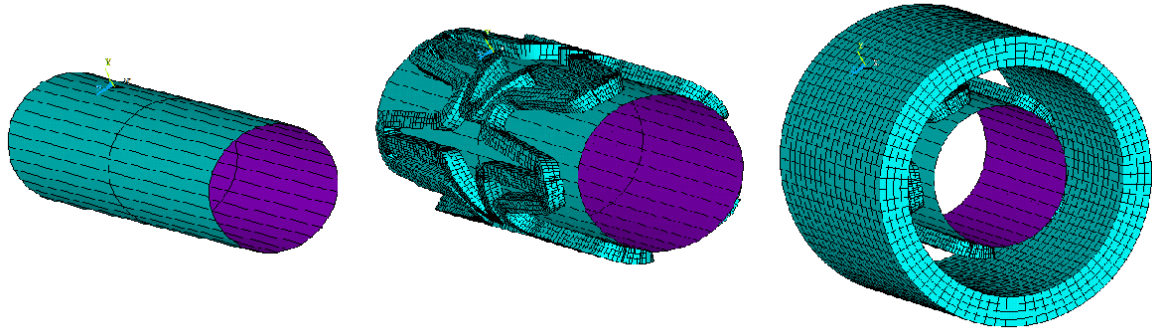


Figure 35 Realization of Stented vessel geometry step by step: the first panel shows the balloon surface, in the second there is the contact between the balloon and the stent and finally, in third one, balloon, stent and vessel are presented together.

The ANSYS simulations run for this geometry are listed below:

- f) the whole Stented vessel was expanded by a radial displacement of 0.5mm applied to the balloon areas. The end of the stent and the vessel geometry were constrained in the circumferential and axial direction to avoid undesired rotations and translations of the components. The element type used is the SOLID185.
- g) Half of Stented vessel model was expanded by a radial displacement of 0.5mm applied to the balloon areas. The end and the middle part of the stent and the vessel geometry were constrained in the circumferential and axial direction to avoid undesired rotations and translations of the components. The element type used is the SOLID185.

The definition of surface-to-surface contact is important to model balloon-stent and stent-vessel contact. In this study, a rigid-to-flexible contact was used for the balloon-stent contact and a flexible-to-flexible contact was used for the stent-vessel contact. Usually the target surface is the deformable one and is modeled with TARGET170 element type while the contact surface, modeled with CONTACT174 element, is the rigid one.

11.2 Bending Problem

In these analyses the SOLID185 element was used, the ANSYS Element Reference states that KEYOPT(2) = 2, which uses the Enhanced Strain element formulation, is recommended for problems with significant bending. As stent deployment generates

bending in the vessel wall more than under uniform pressure loading this element option was used to improve agreement between ANSYS strain and derived strains.

The expected value, which is used to evaluate if KEYOPT(2) = 2 really improves the calculation, was estimated with the following formula:

$$\varepsilon_{\theta,true} = \log (1 + \varepsilon_{\theta,eng})$$

with

$$\varepsilon_{\theta,eng} = \frac{u_{rr}}{r_e}$$

where $\varepsilon_{\theta,eng}$ is the Engineering circumferential strain, u_{rr} is the radial displacement and r_e is the external radius.

For this initial analysis a relatively coarse mesh was used with 120 elements in the axial direction, 40 in the circumference and 2 across the thickness.

11.3 Mesh sensitivity test

To determine the best trade-off between mesh density, computational time and effort to undertake the manual reconstruction of the stented vessel a mesh convergence study was performed on the vessel wall by evaluating the ANSYS strains on the central ring of the vessel, which is located at the middle of the stent. The parameters used for these tests are given in Table 21.

Geometry	Material	Simulations	Calibration	Element
C	2	f	/	SOLID185

To reduce the computational expense of the solution and reduce simulation times a half model in the axial direction was used. Figure 36 shows the half model with the vessel discretised using the coarsest mesh (mesh A in Table 22)

Mesh refinement was undertaken in two stages, as for the Vessel geometry the mesh parameters used are given in Table 22.

Table 22 First stage mesh refinement in radial and circumferential direction; second stage mesh refinement in axial direction

First stage mesh refinement				Second stage mesh refinement			
Mesh	N axial	N circumferential	N radial	Mesh	N axial	N circumferential	N radial
A	120	40	2	C1	60	80	4
B	120	60	3	C2	120	80	4
C	120	80	4	C3	180	80	4
D	120	100	5				

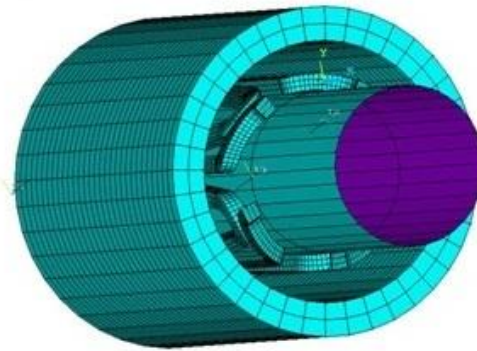


Figure 36 Half vessel and stent model used to do faster mesh analysis

11.4 Strain distribution

In order to clarify how the strain is distributed along the vessel, the strain given by the simulation undertaken using the parameters given in Table 23 is analysed.

Table 23 Protocol code

Geometry	Material	Simulations	Calibration	Element
C	2	f	/	SOLID185

In addition nodal components were created to plot the strain distributions at axial positions outside, but however closed, to the stented region of the vessel, in order to analysis the presence of end effects caused by the ends of the stent. Three rings were defined (un_Ring1 $z=3.466$ mm, un_Ring2 $z=3.899$ mm, un_Ring3 $z=4.332$ mm) and the corresponding strains were also extracted from ANSYS at these locations (Figure 37).

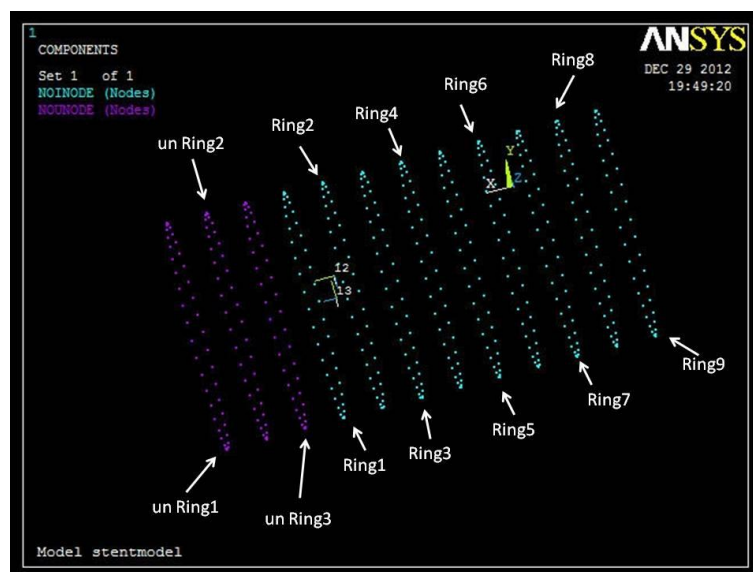


Figure 37 Location of circumferential rings used to assess symmetry of strain distribution within the stented region (Ring 1 – Ring 9) and in the unstented region (un_Ring1 – un_Ring3)

11.5 Symmetry

In order to clarify if the strain which is generated within the vessel is symmetric with respect to the middle of the geometry, the comparisons between the ANSYS strains on selected circumferential rings were made. These tests were undertaken using the parameters given in Table 24.

Geometry	Material	Simulations	Calibration	Element
C	2	f	/	SOLID185

The location of the circumferential rings is illustrated in Figure 37 and the axial location of these 9 rings is given in Table 25, rings identified with the same colour were compared. The centre of the stent geometry corresponds to Ring 5.

Ring	1	2	3	4	5	6	7	8	9
Axial (z) location	4.768	5.201	5.634	6.067	6.500	6.933	7.366	7.799	8.232

11.6 Reconstruction and image registration

Following these preliminary tests to assess the influence of mesh sensitivity and the symmetry of the solution the complete virtual stereoscopic process was performed on the configuration reported in Table 26 to evaluate the accuracy and performance of the system.

Geometry	Material	Simulations	Calibration	Element
C	3	f	12	SOLID185

As for both the Strip and Vessel geometries, the nodal coordinates were extracted using two approaches:

- manual reconstruction of the first and final step of deformation;
- image registration using images captured by the virtual camera rig.

As for the vessel geometry only 285 nodes were picked or registered as only a slice of the whole stented vessel can be seen by both cameras using the current stereo camera configuration (Figure 38).

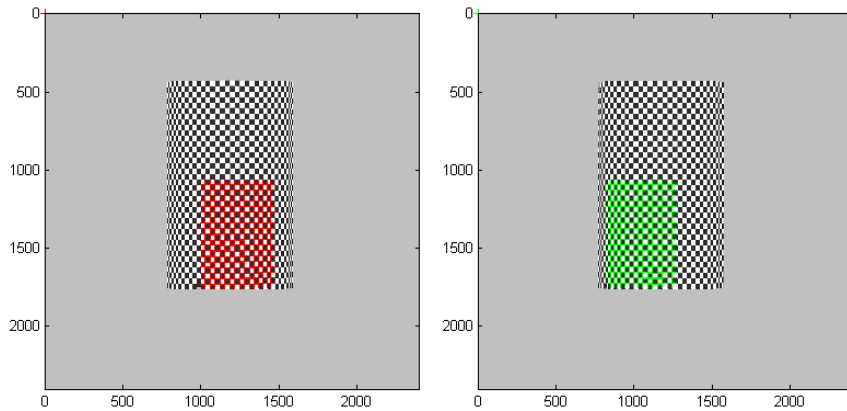


Figure 38 Left and right camera views of Stented vessel geometry in Realsoft 3D showing region that can be reconstructed.

The strains were calculated with two of the three strain calculation methods measurements illustrated above: the true Local strain and the Green-Lagrange measure. The Global strain approach was not applied to the data because of a problem due to the curvature of the Stented vessel geometry, as already shown in the previous paragraph for Vessel. Transforming the nodal coordinates from a Cartesian to a Cylindrical reference system presented a difficulty due to a mismatching between them. This mismatching was caused by the calibration procedure, as already underlined in the Goude work [10]. The interpolation of the displacements on the Cylindrical coordinates would have been distorted and the results coming from the Global strain formula would have not been comparable with the values given by ANSYS.

Results

The Results section of this report considers the results of the study grouped by the geometry of interest. Firstly, results are reported for the Strip model, followed by the Vessel geometry and concluding with the Stented Vessel configuration.

1. Strip

This section reports the results of tests undertaken on the Strip geometry. Preliminary results are reported to describe the variation of derived strains with application of noise and with changes in the image resolution used to capture the object. The assessment of the influence of the degree of averaging used for the Global strain measures is then reported, referring to the longitudinal strain over two regions of the Strip. Finally, a comparison between manual reconstruction and image registration results is reported over the full region of the model.

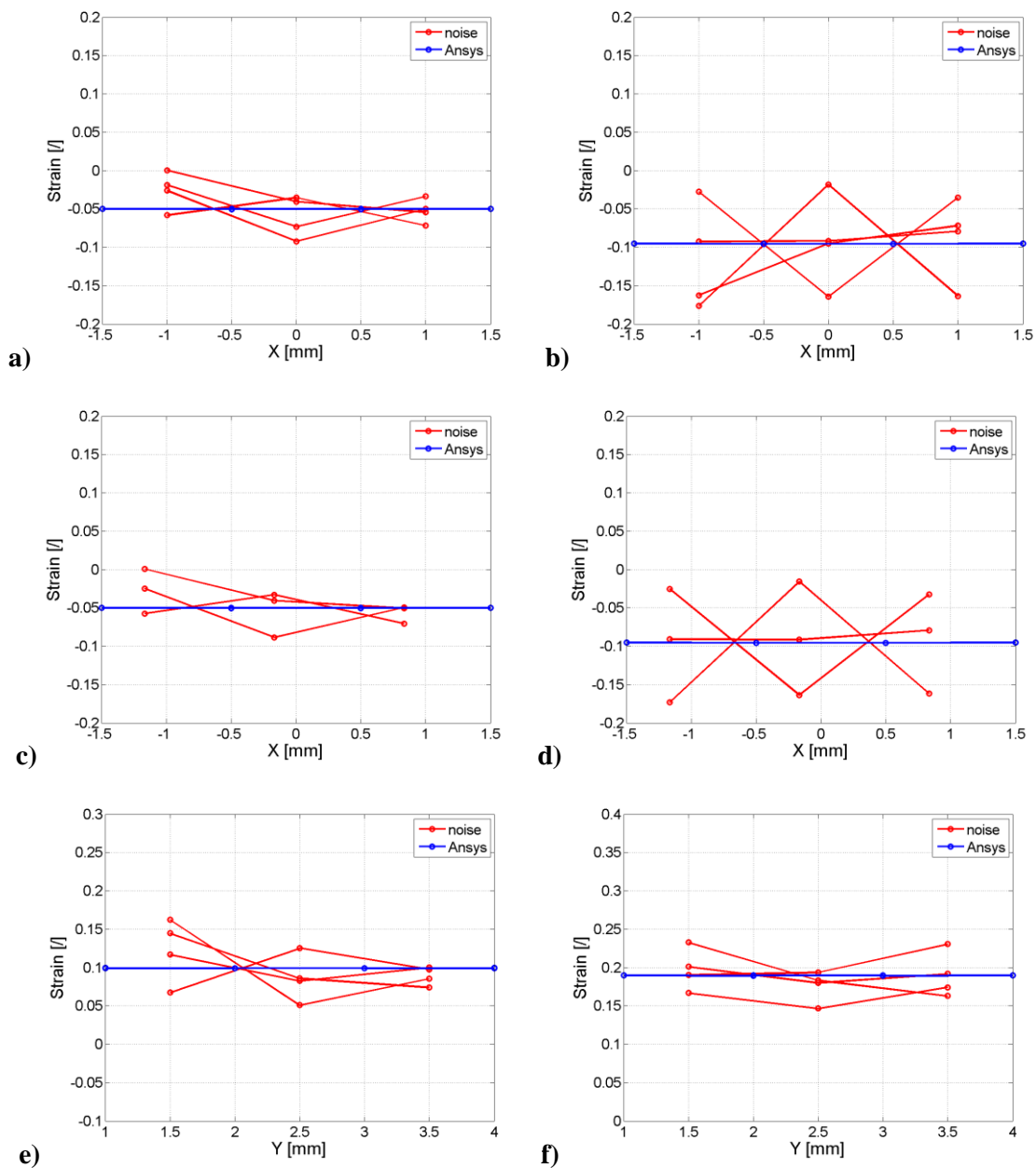
1.1 Preliminary tests

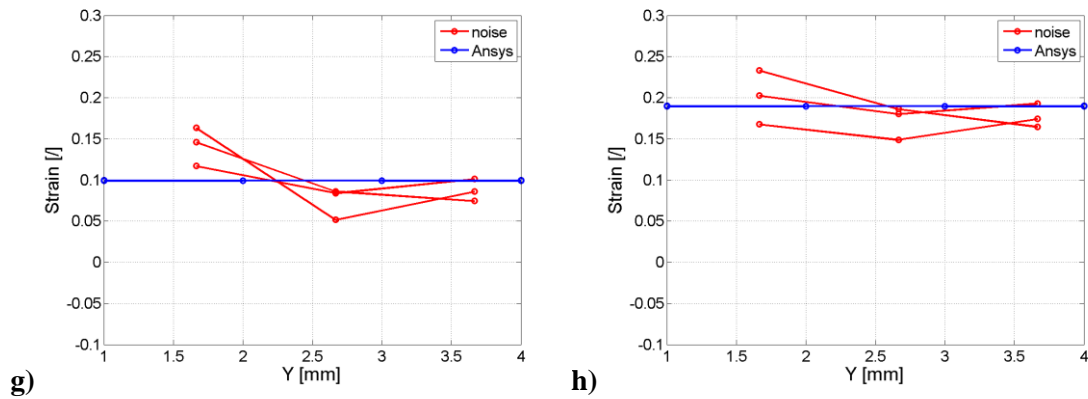
1.1.1 Noise test

The noise test was performed to study how a random noise on the nodal position can affect the final strain measurement. The application of random noise simulates the error due to the manual picking procedure, the disturb given by the technique and the errors due to the system characteristics.

In the transversal direction a random error of $6.20 \pm 5.00\%$ was applied on the position of the nodes. In the longitudinal direction the imposed random error was $5.50 \pm 4.90\%$. The error given to simulate the noise on the position detection was generally random but controlled in magnitude in order to have a realistic value in the context of the present stereoscopic method.

The outputs of this test using by the green strain measurement have been shown in the following graphs (Graph 6) but only one of the five tests is reported. In Graph 6a,b,c,d the longitudinal strain has been plotted against the y coordinates. In Graph 6e,f,g,h the transversal strain has been plotted against the x coordinates.





Graph 6 Strain results after random noise applied to position data: a-d) longitudinal strain; e-h) transverse strain; a,b,e,f) Local strain measure; c,d,g,h) Green strain measure; a,c,e,g) middle stage of deformation; b,d,f,h) final stage of deformation.

The Table 27 below summarizes the errors from the five noise tests in terms of the mean error at all points and the standard deviation, calculated using the Local and Green strain approaches (see Appendix B1 for the complete error Tables 31, 32, 33 and 34); both absolute values of error and percentage values are reported.

Table 27 Absolute and percentage error on the strain after applying a random error on the position

		Transversal		Longitudinal		Transversal		Longitudinal	
		Green	LS	Green	LS	Green	LS	Green	LS
		Absolute error				Percentage error			
Middle step	Mean	0.026	0.027	0.027	0.027	52.47	54.55	27.64	27.21
	Std	0.020	0.020	0.018	0.019	38.83	39.50	18.19	18.77
	Mean + std	0.046	0.047	0.045	0.046	/	/	/	/
Final step	Mean	0.040	0.038	0.022	0.021	42.04	40.32	11.51	11.17
	Std	0.027	0.028	0.016	0.017	28.88	29.56	8.65	8.97
	Mean + std	0.067	0.066	0.038	0.038	/	/	/	/

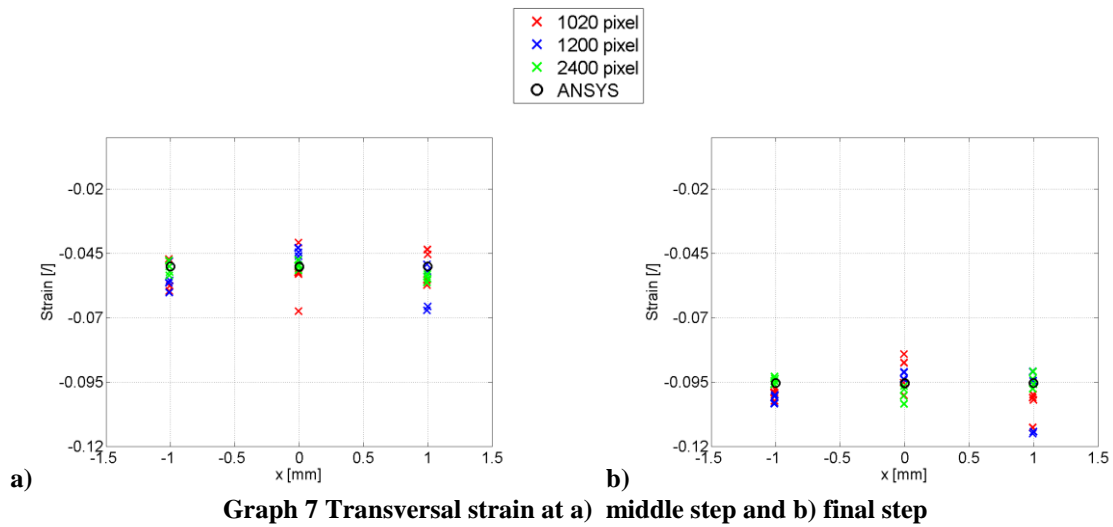
From Graph 6a-d it is possible to see that the deviation of the strain from the ANSYS value remains meanly unchanged while passing from the middle to the final step in the transversal direction (Graph 6e-f) causes an increase of the distance between derived and ideal data. Table 27 shows that the absolute values are fairly constant while the percentage values vary due to smaller strains in transverse direction and higher total strain at final step of deformation.

1.1.2 Resolution test

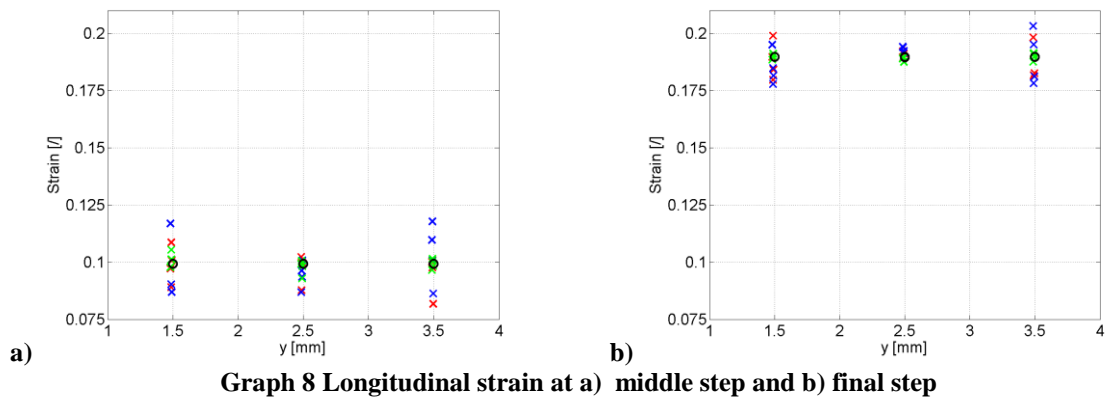
Graph 7 shows the transversal strain at the middle and final stages of deformation taking account of the variation of the number of pixels in the captured images. The Local strain was calculated on a set of 16 points picked in the central part of the strip geometry and the deformation values are reported against the corresponding x coordinates at which they were observed. Similar results for longitudinal strain are shown in Graph 8.

In both direction the plots show that the strain increases from middle to last stage of deformation and the derived measurement are dispersed around the ANSYS value which is considered the golden standard.

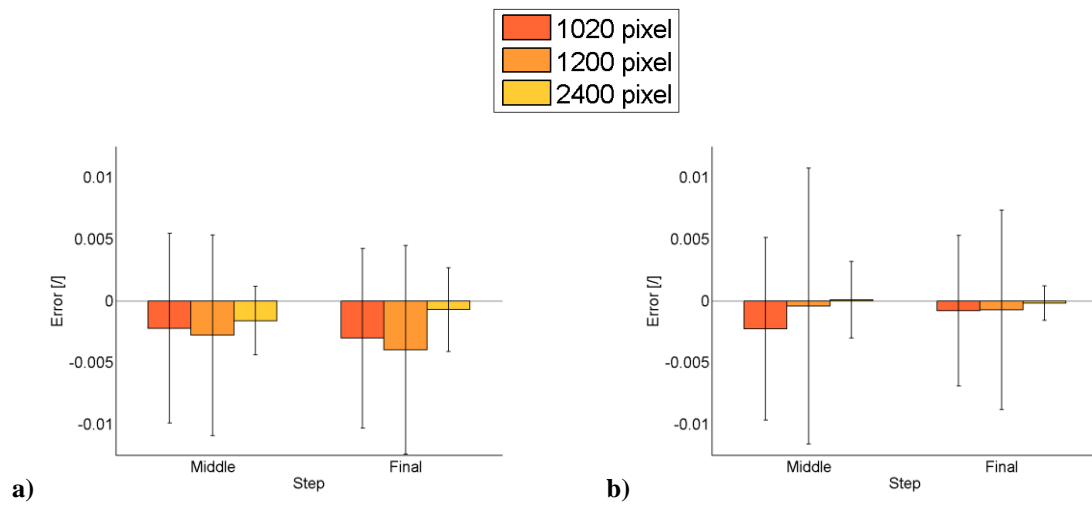
Graph 9 presents the mean and standard deviation of the error on transversal and longitudinal strain. The values are reported as mean absolute error on the measurement with variation in the number of pixels. The size of the error bars is determined by the standard deviation of the error value. The numerical values of these errors are reported in Table 35 and Table 36 in Appendix B2, for the deviation formulas see Appendix A1.



Graph 7 Transversal strain at a) middle step and b) final step



Graph 8 Longitudinal strain at a) middle step and b) final step



Graph 9 a) Absolute error on transversal strain b) Absolute error on longitudinal strain

The bar plots illustrate as the mean and standard deviation reduce as image resolution is increased. The 1200 pixel resolution does not seem to provide a significant improvement, on the contrary in the transversal direction the results are worse, but the 2400 pixel images decrease the error in any direction.

1.1.3 Global strain

Figure 39 represents the ANSYS longitudinal strain at different steps of deformation along the two analysed lines of the strip geometry. The strain along the two rows is reported to better show the variation of the strain value along the longitudinal direction, in fact the central line (1) shows a greater variation of the strain compared to the external column (2) and this affects the following results.

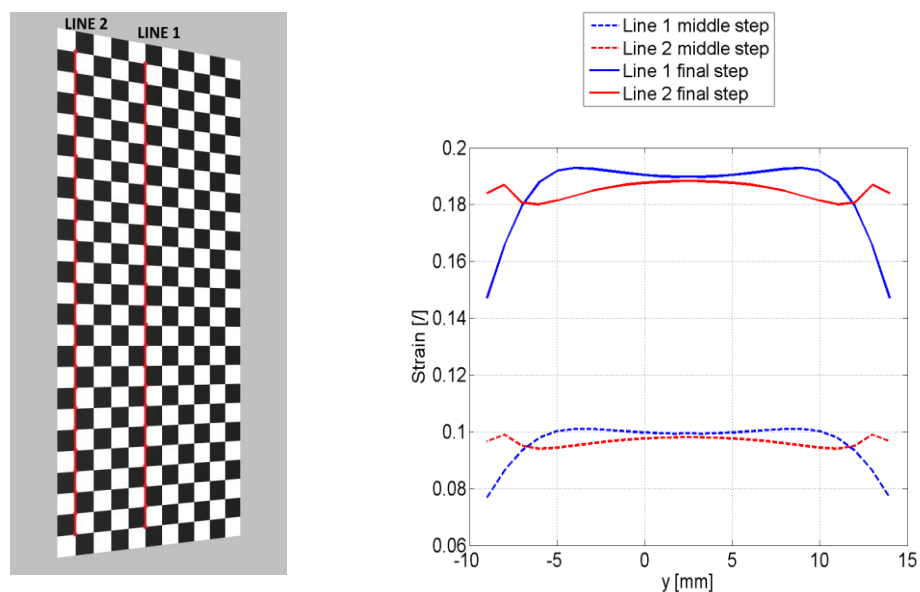
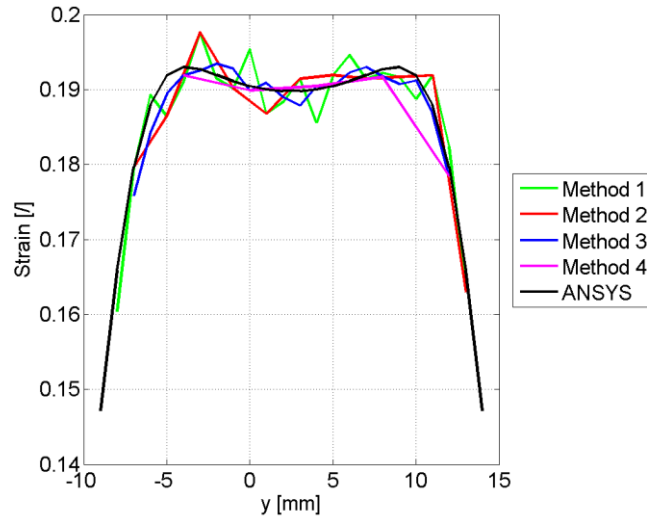


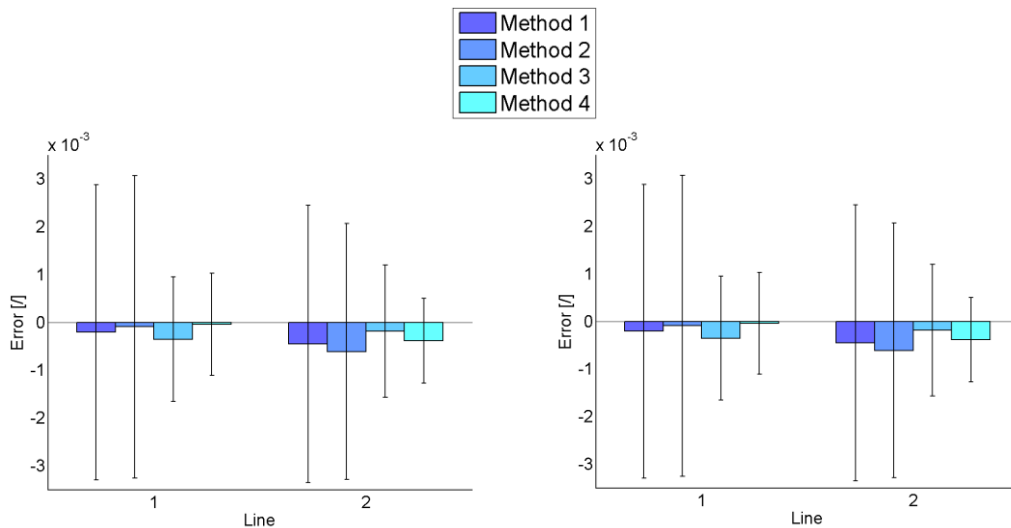
Figure 39 ANSYS longitudinal strain

Four methods were used to derive these strain values, as described in the *Materials and methods* section. Method 1 and 2 apply averaging over 3 nodes, while method 3 and 4 interpolate the displacements over 5 nodes. Method 1 and 3 take the nodal data with a concatenating process and method 2 and 4 select sequential sets of points which do not overlap. As an example Graph 10 shows the ANSYS longitudinal strain and the Global strains calculated with the four methods on line 1 at the final step of deformation.



Graph 10 Longitudinal ANSYS strain and Global strain calculated with the four methods

Graph 11 reports the absolute mean and standard deviation of the error on strain, calculated as the difference between the derived strain and the computational result at the same coordinate. The values are plotted at each step of deformation and along the two lines of investigation. The numerical value of these errors are summarised in Table 37 and Table 38 in Appendix B3, for deviation formulas refer to Appendix A1.



Graph 11 Absolute error on longitudinal strain a) at middle step b) at final step.

As shown in Figure 39 the longitudinal strain on line 1 varies more than the strain on line 2 at both steps of deformation. The consequence of this trend is visible in Graph 11 where the standard deviation always reduces averaging on five points instead of three, but on line 1 the mean value increases as more nodes are used to interpolate. This is probably due to a loss of information during the averaging process. The overall errors are always under 0.0005 demonstrating a good level of accuracy.

1.2 Reconstruction and image registration

This section compares the results obtained using both the manual reconstruction and the image registration methods to derive measures of strain for the Strip geometry. Four analyses were undertaken as listed in Table 28.

Table 28 Summary of Strip geometry tests

Test	Geometry	Material	Simulation	Calibration	Element
1	A (Strip)	1 Goude	b (tensile)	14	Plane42
2	A (Strip)	2 Chua	b (tensile)	14	Plane42
3	A (Strip)	3 Wu	b (tensile)	14	Plane182
4	A (Strip)	1	a (zero strain)	14	Plane42

Figure 40 and Figure 41 report the contours of strain in the longitudinal and transversal directions for test 1. Figure 42 and Figure 43 illustrate the strain distribution in the longitudinal and transversal directions for test 2. Figure 44 and Figure 45 show the contours of strain in both directions for test 3. Finally Figure 46 and Figure 47 report similar results for test 4. Each plot provides seven measures of strain: ANSYS reported strains, three measures of strain obtained using the manual reconstruction and three measures of strain obtained using image registration. For both the manual reconstruction and the image registration methods the three measures of strain are obtained using the Green strain, Local strain and Global strain approaches. For the global strain measure averaging was undertaken using Method 3 with local groups of five nodes.

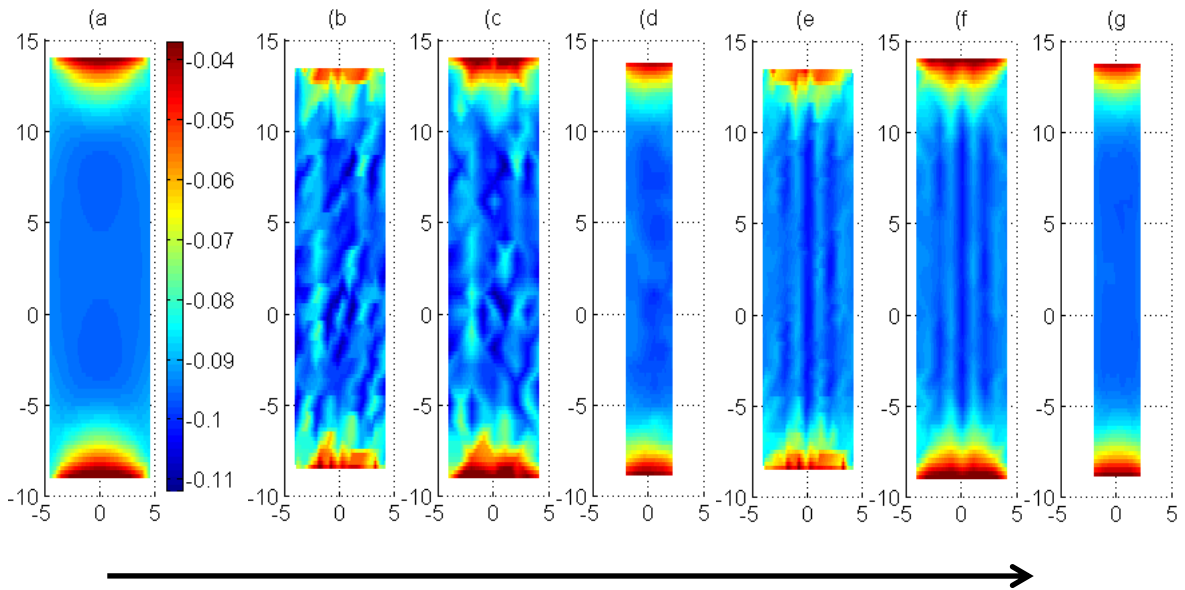


Figure 40 Transversal strain results (direction shown by arrow) for test 1: a) ANSYS strain; b) - d) reconstruction results; e) – g) image registration results; b) and e) Green strain; c) and f) Local strain; d) and g) Global strain.

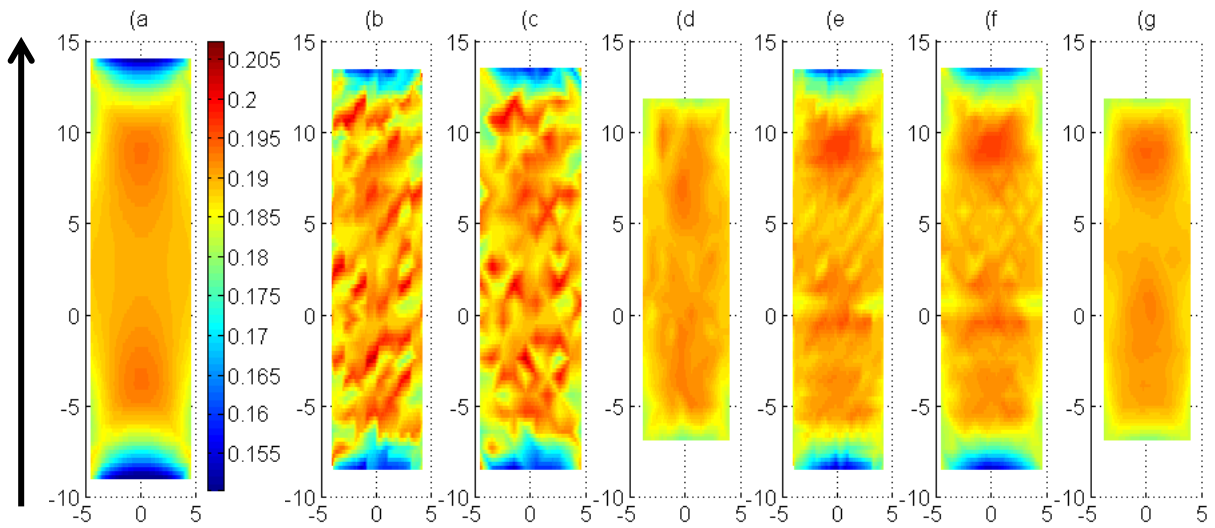


Figure 41 Longitudinal strain results (direction shown by arrow) for test 1: a) ANSYS strain; b) - d) reconstruction results; e) – g) image registration results; b) and e) Green strain; c) and f) Local strain; d) and g) Global strain.

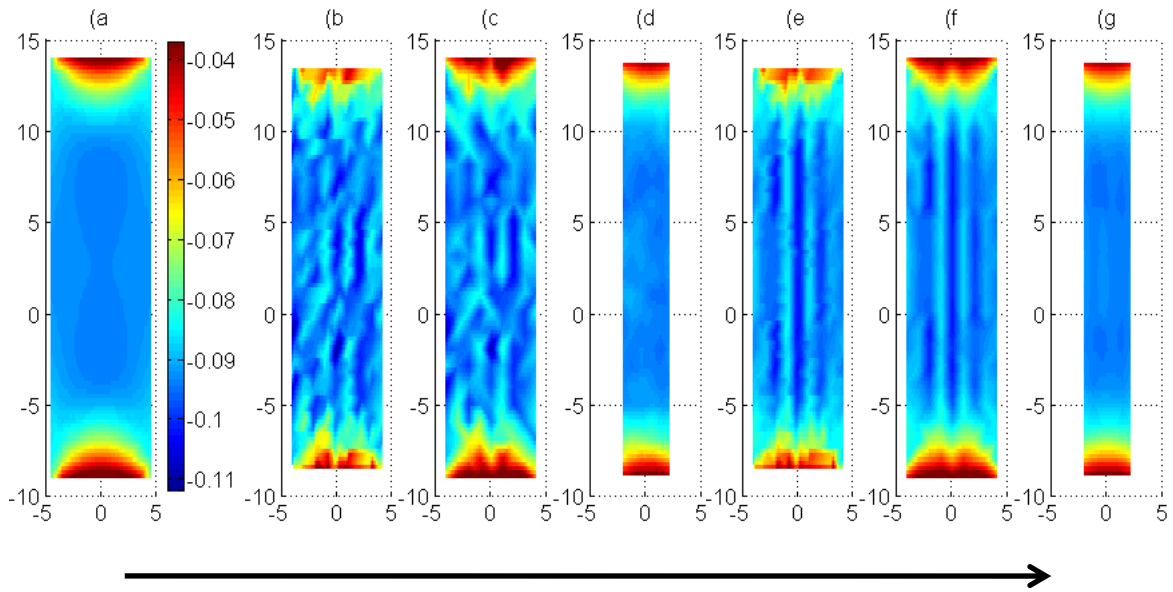


Figure 42 Transversal strain results (direction shown by arrow) for test 2: a) ANSYS strain; b) - d) reconstruction results; e) – g) image registration results; b) and e) Green strain; c) and f) Local strain; d) and g) Global strain

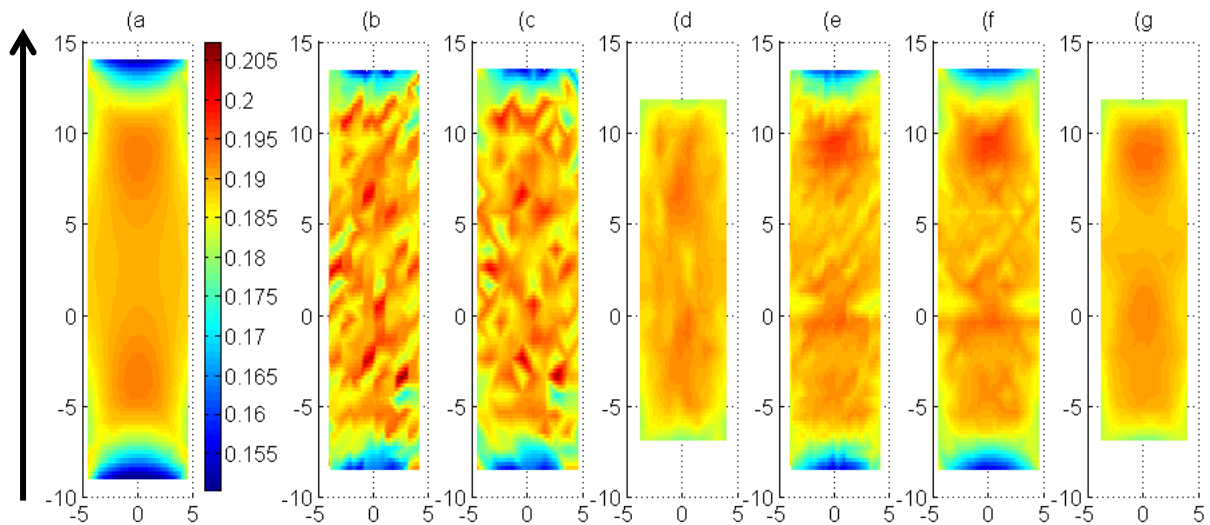


Figure 43 Longitudinal strain results (direction shown by arrow) for test 2: a) ANSYS strain; b) - d) reconstruction results; e) – g) image registration results; b) and e) Green strain; c) and f) Local strain; d) and g) Global strain.

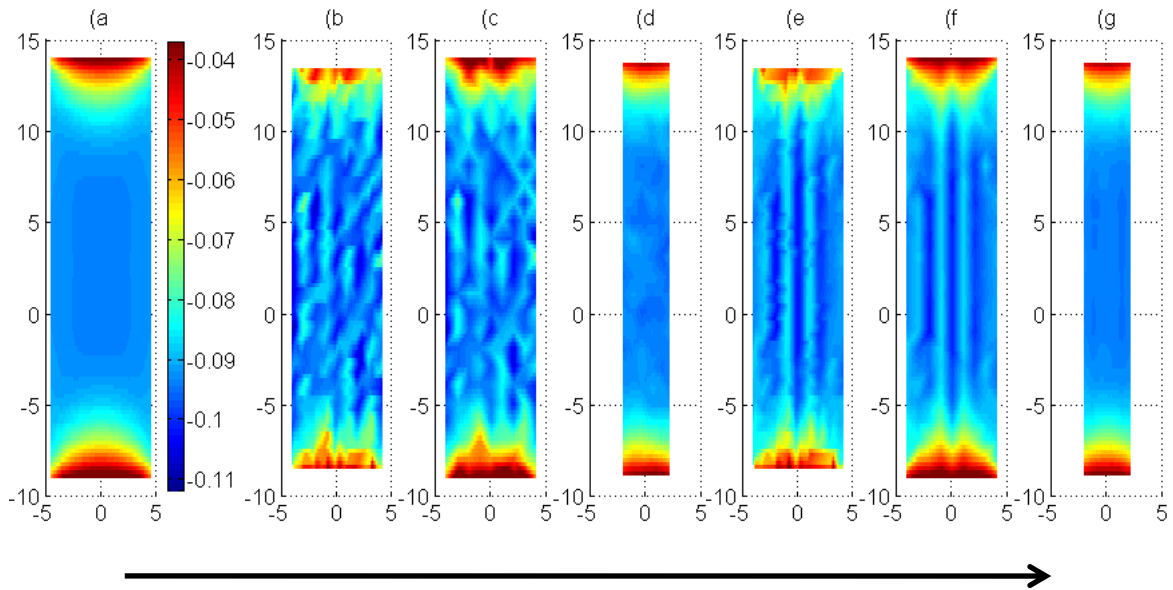


Figure 44 Transversal strain results (direction shown by arrow) for test 3: a) ANSYS strain; b) - d) reconstruction results; e) – g) image registration results; b) and e) Green strain; c) and f) Local strain; d) and g) Global strain.

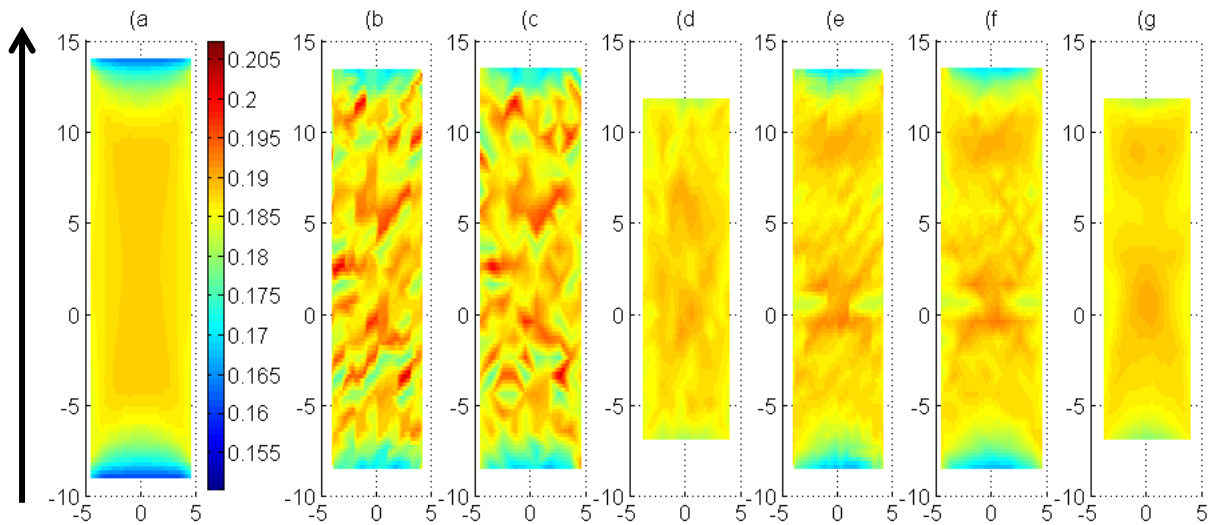


Figure 45 Longitudinal strain results (direction shown by arrow) for test 3: a) ANSYS strain; b) - d) reconstruction results; e) – g) image registration results; b) and e) Green strain; c) and f) Local strain; d) and g) Global strain.

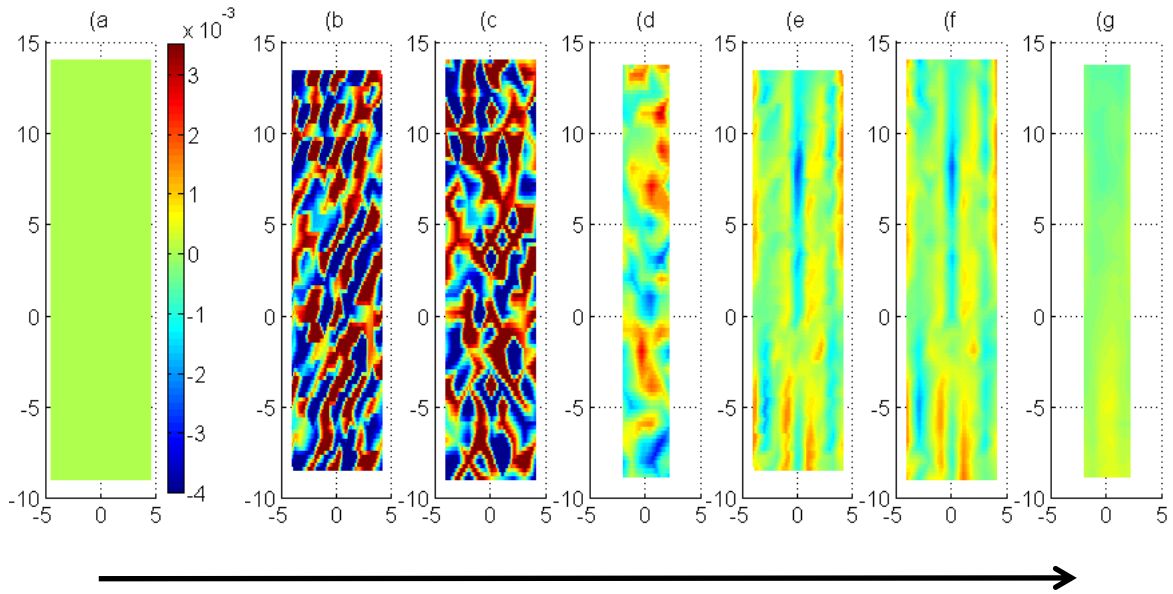


Figure 46 Transversal strain results (direction shown by arrow) for test 4: a) ANSYS strain; b) - d) reconstruction results; e) – g) image registration results; b) and e) Green strain; c) and f) Local strain; d) and g) Global strain.

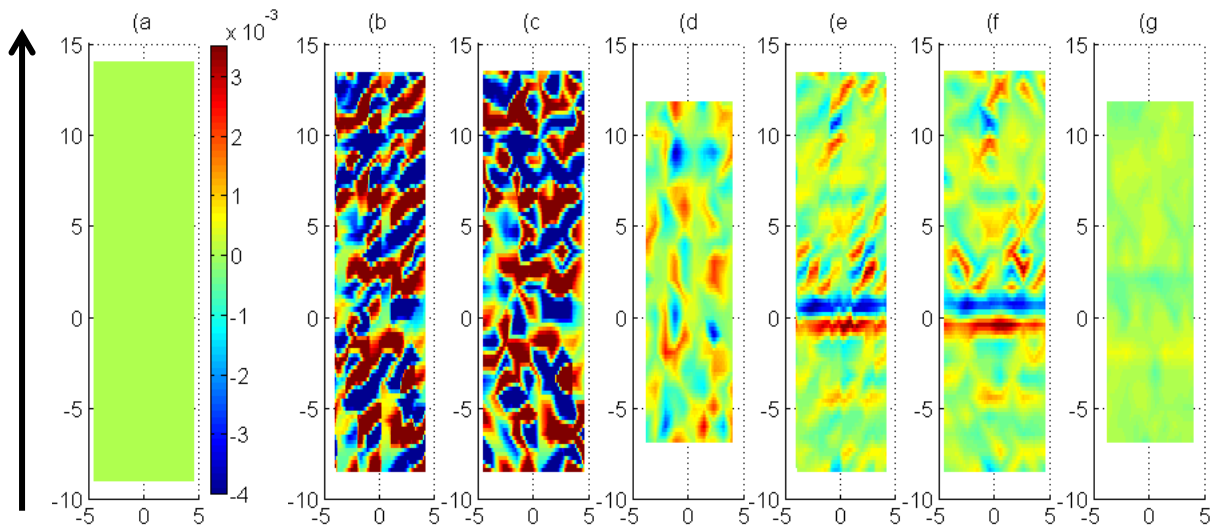


Figure 47 Longitudinal strain results (direction shown by arrow) for test 4: a) ANSYS strain; b) - d) reconstruction results; e) – g) image registration results; b) and e) Green strain; c) and f) Local strain; d) and g) Global strain.

As it is possible to see the size of the reported areas is different for each plot. This is due to the fact that every calculation method employs a different number of points' coordinates to obtain the strain, therefore the covered areas result various. For example the Global strain approach performs an averaging on a set of nodes and the derived values are related to a reduced amount of nodes. On the opposite the Green strain is the method which computes more strain values because of the triangulation approach and the centroids coordinates.

From Figure 40 to Figure 47 is reported an evident noise on the Green and Local strain results and the Global strain seem to improve the correspondence with the ANSYS data. The level of noise appears reduced when using image registration rather than manual reconstruction for all tests.

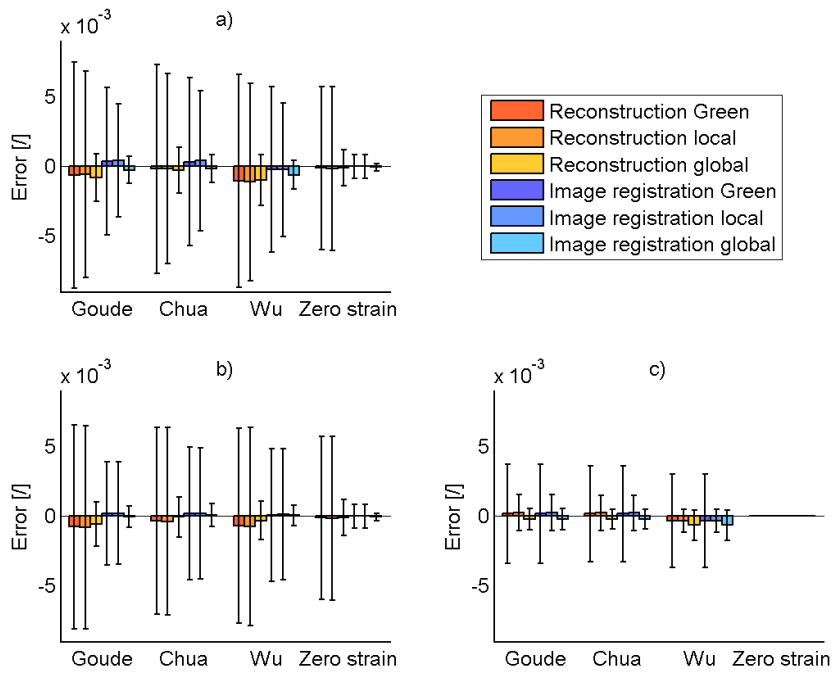
The contour results of test 2 and 3 seem to be very similar in both directions to those obtained for test 1, so the overall behaviour does not change significantly. Test 3 shows values of strain slightly lower than in the other tests and this is due to the stiffness of the material which becomes hyperelastic instead of linear elastic.

Figure 46 and Figure 47 illustrate the contour plots relative to the zero strain test. The comments are similar to those made for the first three tests, so the noise in the manual reconstruction results is remarkable while the image registration introduces a visible improvement. The contour values vary in a range between -0.004 and 0.004 so the maximum errors due to the picking operation are of the order of 10^{-3} .

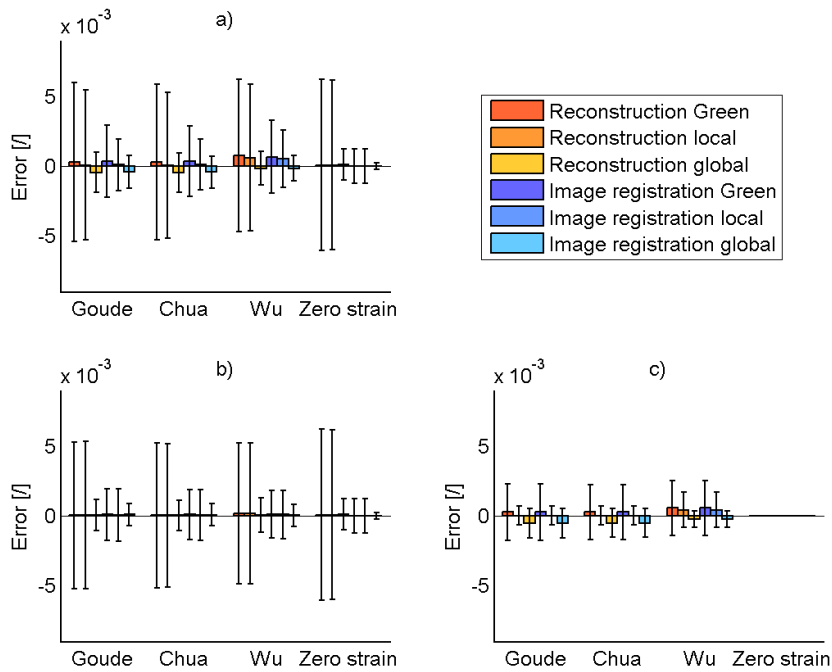
Graph 12 and Graph 13 compare results over all four tests reporting the mean error and standard deviation for the transversal and longitudinal strain respectively. For each test three comparisons of error measure were taken into account:

- a) between the values obtained with the photogrammetric method (test data) and ANSYS reported strains;
- b) between the values obtained with the photogrammetric method (test data) and strains calculated from the ANSYS 3D position data using the experimental post-processing (ANSYS derived strains);
- c) between the ANSYS derived strains and ANSYS reported strains.

The numerical values of the strain comparison are reported in Appendix B4 from Table 40 to Table 47. The errors are calculated with the relationships in Appendix A1.



Graph 12 Error on transversal strain: a) test data vs. ANSYS reported data; b) test data vs. ANSYS derived data; c) ANSYS derived data vs. ANSYS reported data.



Graph 13 Error on longitudinal strain: a) test data vs. ANSYS reported data; b) test data vs. ANSYS derived data; c) ANSYS derived data vs. ANSYS reported data.

Graph 12 and Graph 13 indicate that the overall error (mean plus standard deviation) on strain measurements for the Strip geometry is generally low. The mean values are always small and the standard deviation is below 0.005 for most cases; this shows a good accuracy of the system for 2D configurations. The four materials do not seem to introduce significant differences in the behaviour of the model.

The Global strain measure tends to reduce the standard deviation of error in all the cases, thanks to the averaging process which smoothes the reconstruction errors. The image registration appears particularly effective in the dominant direction and reduces the mean and standard deviation in most cases.

The overall error is generally higher in the transversal direction and this is probably related to the low level of deformation. On the opposite in the longitudinal direction where the deformations are greater the error is lower, especially on the Green and Local strain.

The comparison between the three analyses underlines that the error on the transversal strain is due both to the noise introduced by the optical system and to the formula approximations, while the error on the longitudinal data is mainly related to the calculation method.

2. Vessel

This section reports the results of tests undertaken on the Vessel geometry. Preliminary results are first illustrated to describe the comparison between computational results and thick-walled theory and to assess mesh sensitivity. This section is followed by a comparison of the manual reconstruction results with the image registration data.

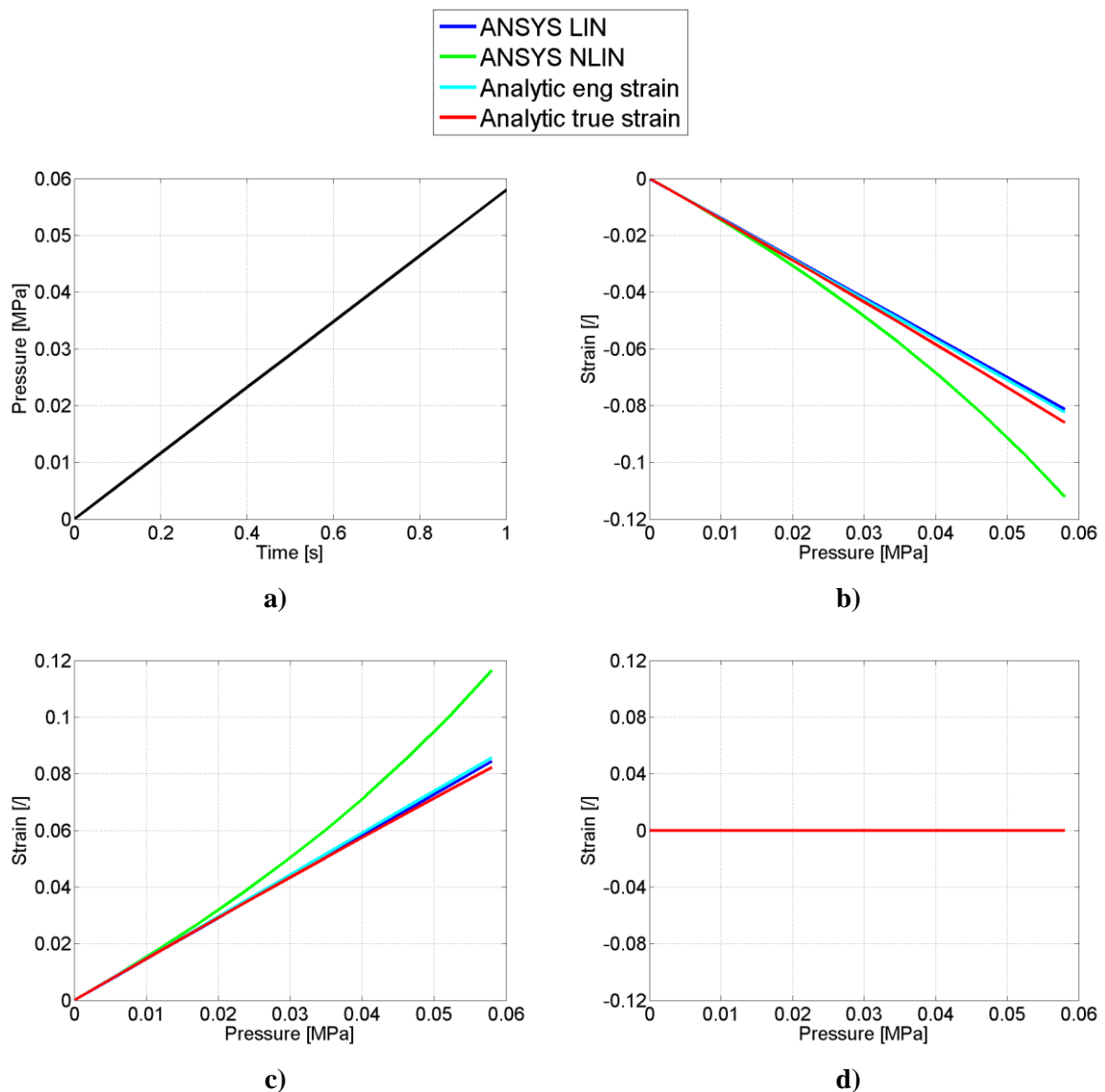
2.1 Preliminary tests

2.1.1 Expected values: thick wall theory

In this test the vessel was expanded with a pressure of 0.058 MPa and the computational strains were compared to an analytical solution to evaluate if the ANSYS simulation provided values of strain which corresponded to the expected values and therefore if it was possible to rely on the ANSYS data in the following studies. The computational results presented here are confronted with the thick-walled theory. The applied pressure varies linearly with the analysis time as shown in Graph 14a. The circumferential, radial and axial components of strain are plotted with increasing pressure in Graph 14b –Graph 14d. The values have been extracted from the ANSYS simulation with both non-linear and linear

effects (ANSYS NLIN and LIN) and are compared with the analytical solution (engineering and true strain).

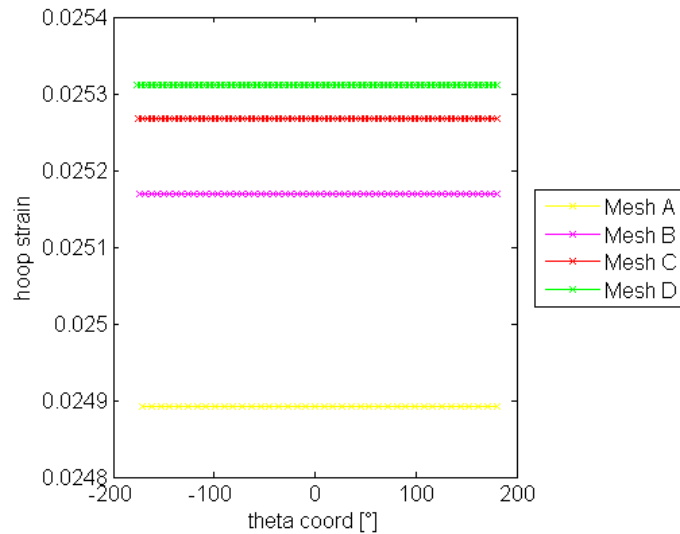
Graph 14b and Graph 14c show that the ANSYS solution is well approximated by the analytic engineering strain. This suggests that when the non-linear effects are deactivated the software computes the strain as an engineering value since the deformations are supposed to be little. Instead the non-linear ANSYS data diverge from the analytic strain after 2% of deformation; this trend is expected because the approximations made in the thick-wall theory exclude the non-linear behaviours. In Graph 14d the axial strain is zero for all the cases due to the plane strain conditions imposed at the beginning of the simulation.



Graph 14 a) Variation in applied pressure with analysis time. Variation of strain results with applied pressure: b) radial strain; c) circumferential strain; d) axial strain.

2.1.2 Mesh sensitivity test

The mesh sensitivity test was performed to determine the best mesh which optimised the goodness of the solution and the computational time required to run the simulation. The mesh was first tested in the circumferential direction and through the thickness, then the axial number of elements was refined. Graph 15 shows the trend of the ANSYS strain at the centre of the vessel at the total applied pressure for four different mesh densities, from a coarse to a fine mesh in both circumferential and radial directions.

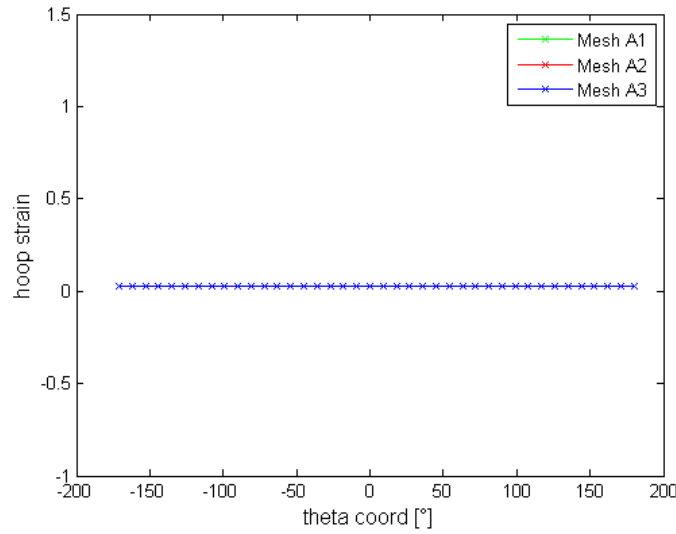


Graph 15 ANSYS circumferential strain against theta coordinate. The strain is plotted for each one of the four meshes with different numbers of elements in the circumferential and radial direction.

After define a threshold of 0.005, the absolute error between the ANSYS strain extrapolated from a mesh and the finest one (Mesh D), taken as the gold standard mesh, was always under this threshold. The difference between the coarsest (Mesh A) and the finest (Mesh D) mesh is about 0.0004 and the comparison between Mesh D and Mesh C is less than 0.0001

In Graph 16 the circumferential ANSYS strain from models with different axial mesh has been plotted against the tetha coordinates.

In this case the comparison between the strain values, on the middle ring, given by different ANSYS simulations shows that they are equal for every mesh, in fact the absolute error is null.



Graph 16 ANSYS hoop strain against theta coordinate. The strain is plotted at different mesh refinements in the axial direction.

2.2 Reconstruction and image registration

This section compares the results obtained using both the manual reconstruction and the image processing methods to derive measures of strain for the Vessel geometry. Four analyses were undertaken as listed in Table 29.

Table 29 Summary of Vessel geometry tests

Test	Geometry	Material	Simulation	Calibration	Element
1	B	2 (Chua)	c (120 mmHg.)	12	SOLID185
2	B	2	d (over)	12	SOLID185
3	B	3 (Wu)	c	12	SOLID185
4	B	3	d	12	SOLID185

Figure 48 and Figure 49 report the contours of strain in the circumferential and axial directions for test 1. Figure 50 and Figure 51 show the same results for test 2 and similarly Figure 52 and Figure 53 represent the strain distribution in both directions for test 3. Finally Figure 54 and Figure 55 report the strain values for test 4. Each figure provides five strain contour plots: the first one is the ANSYS reported strain, the second and third distributions represent the two measures of strain obtained applying the Green and Local strain on the manual reconstruction data, the fourth and last plots illustrate the Green and Local strain measured derived from the image registration nodal coordinates.

The contour plots present a rectangular shape although the vessel is a tridimensional geometry because the analysed patch is represented from a frontal point of view. The

curvature of the cylinder is not visible from this perpendicular perspective but it was taken under account in the data processing.

As it was already observed for the Strip geometry the size of the contour areas is different for each plot. This is due to the fact that every calculation method employs a different number of points' coordinates to obtain the strain, therefore the covered areas result various. The Global strain approach computes the lowest amount of strain data since it performs an averaging on a set of nodes; on the contrary the Green strain method produces more strain values because in the triangulation the deformation is computed at the centroids and every element is characterised by two centroids.

From Figure 48 to Figure 55 it is shown that the strain measurement on the Vessel geometry is affected by evident noise. In fact the Green and Local measurements are disturbed and the contour plots are featured by peaks and vales of strain. The level of noise appears reduced when using the image registration rather than the manual reconstruction to pick the points; once more the registration technique introduces an improvement on the data acquisition due to the semi-automatic position selection.

The axial strain is expected to be always zero due to the plain strain conditions applied to the vessel and the results are similar in every test. The ANSYS strain is null while the Green and Local strains for the manual reconstruction present prominent deviations from the ideal value and also the image registration is affected by noise, although the error is reduced in magnitude.

In the circumferential direction the level of deformation differs in every test depending on the materials and loadings. Test 1 presents a little deformation because of the linear material and the low pressure of inflation, while test 2 is performed with the same material but a higher displacement and the resulting hoop strain is almost ten times the previous value. The material for test 3 is hyperelastic and using the same level of pressure applied in test 1 the circumferential deformation is greater. Finally test 4 has a bigger hoop strain than the result of test 2 where the displacement imposed at the vessel was the same. The influence of noise on the hoop contour plots is the same observed in the axial direction. A remarkable feature is the presence of vertical stripes on the circumferential strain distribution in the image registration results. This could be the marker of an error introduced by the calculation method because of the geometry's curvature.

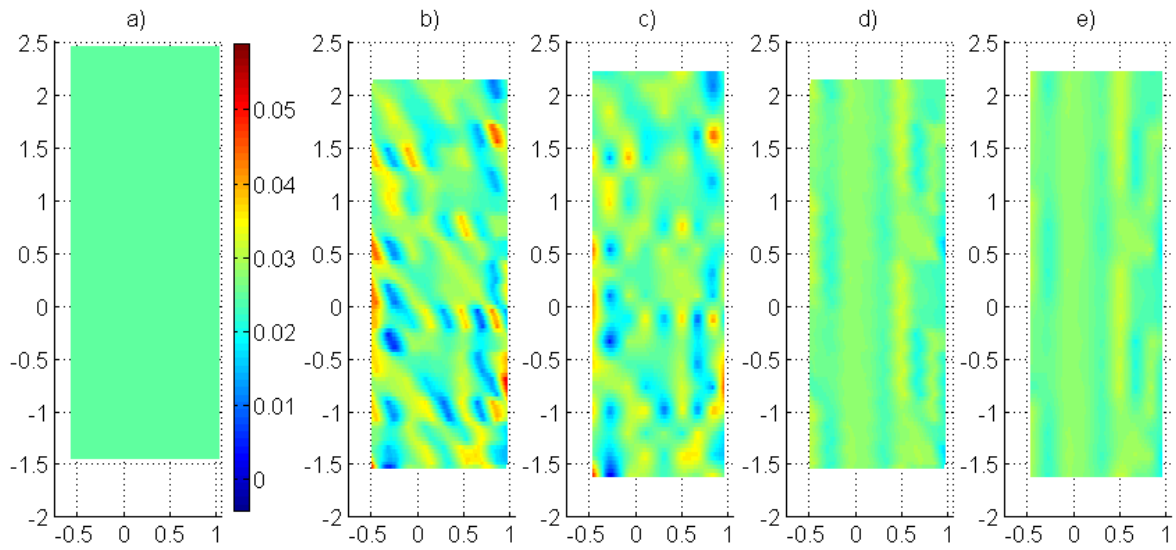


Figure 48 Circumferential strain results (direction shown by arrow) for test 1: a) ANSYS strain; b) and c) reconstruction results; d) and e) image registration results; b) and d) Green strain; c) and e) Local strain.

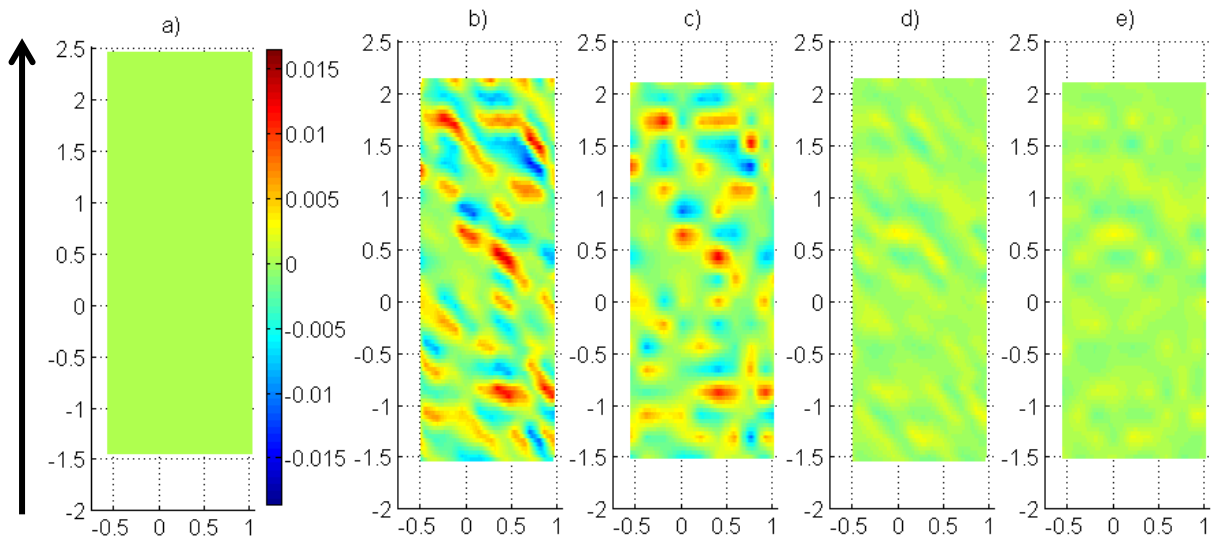


Figure 49 Axial strain results (direction shown by arrow) for test 1: a) ANSYS strain; b) and c) reconstruction results; d) and e) image registration results; b) and d) Green strain; c) and e) Local strain.

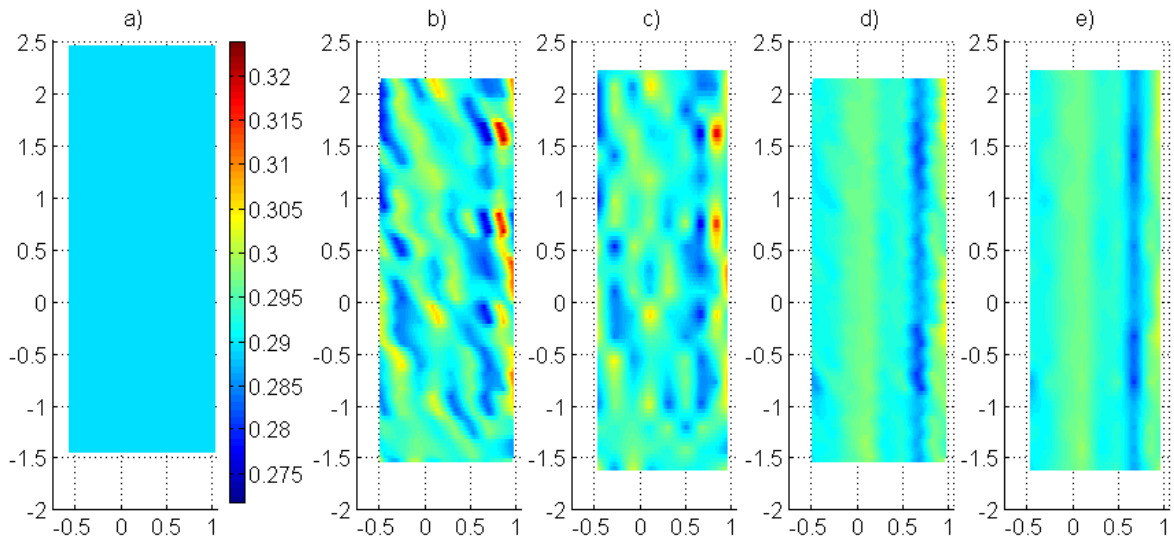


Figure 50 Circumferential strain results (direction shown by arrow) for test 2: a) ANSYS strain; b) and c) reconstruction results; d) and e) image registration results; b) and d) Green strain; c) and e) Local strain.

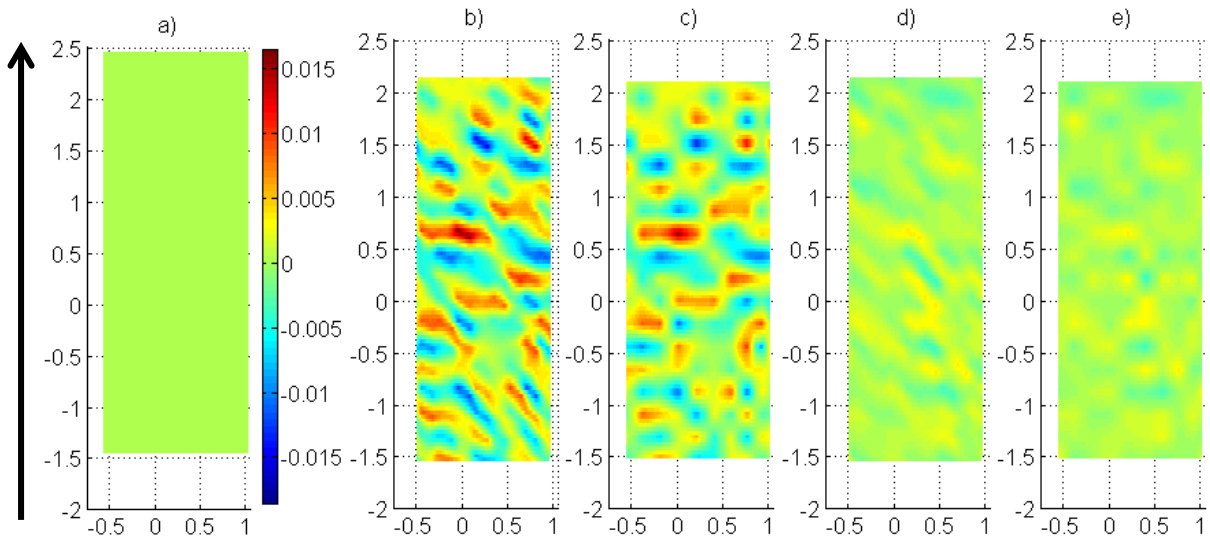


Figure 51 Axial strain results (direction shown by arrow) for test 2: a) ANSYS strain; b) and c) reconstruction results; d) and e) image registration results; b) and d) Green strain; c) and e) Local strain.

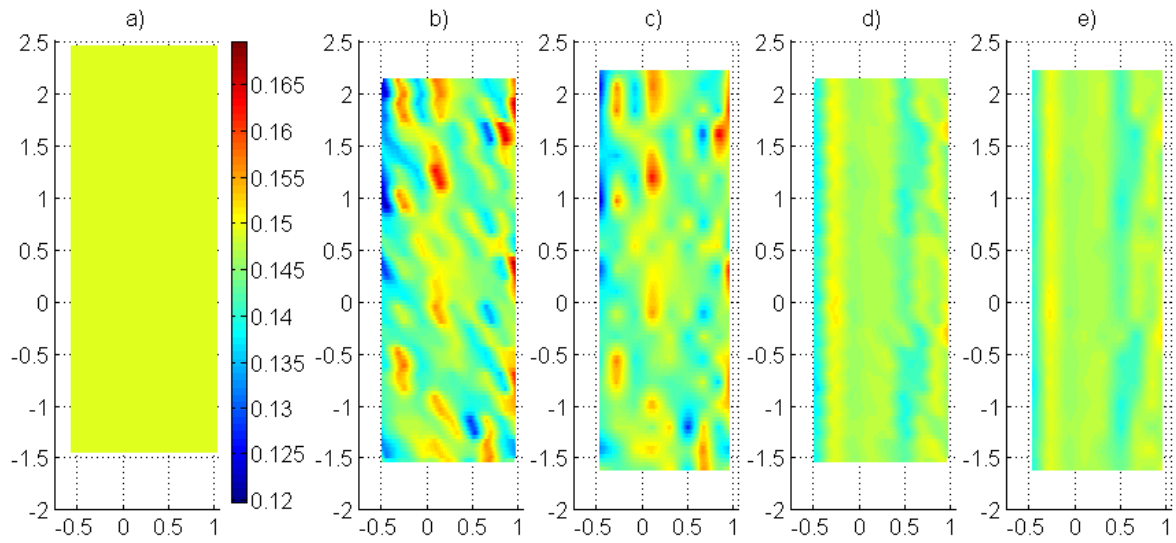


Figure 52 Circumferential strain results (direction shown by arrow) for test 3: a) ANSYS strain; b) and c) reconstruction results; d) and e) image registration results; b) and d) Green strain; c) and e) Local strain.

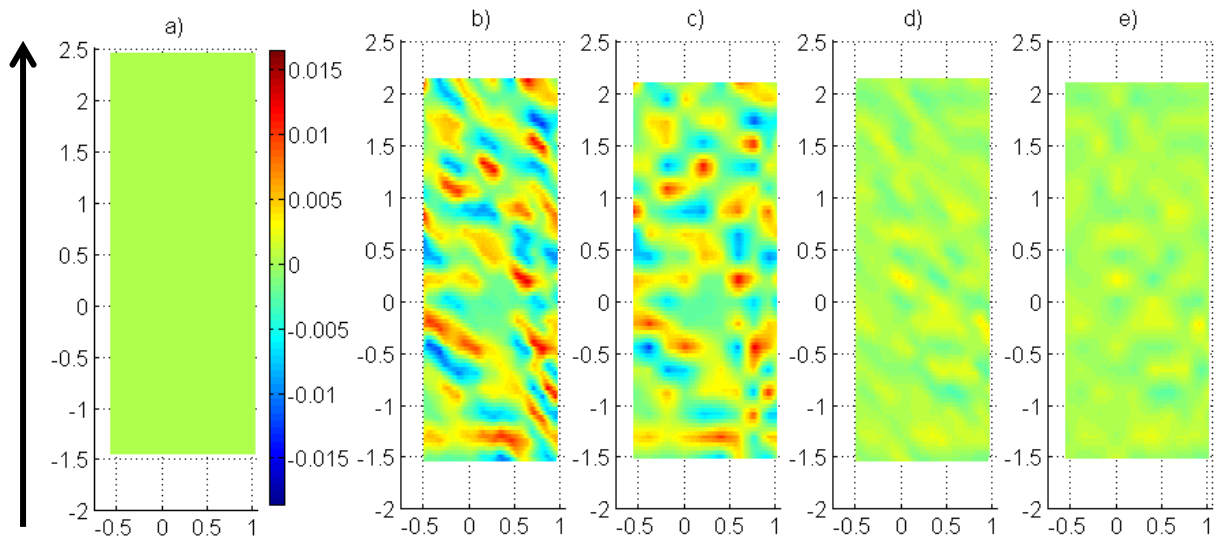


Figure 53 Axial strain results (direction shown by arrow) for test 3: a) ANSYS strain; b) and c) reconstruction results; d) and e) image registration results; b) and d) Green strain; c) and e) Local strain.

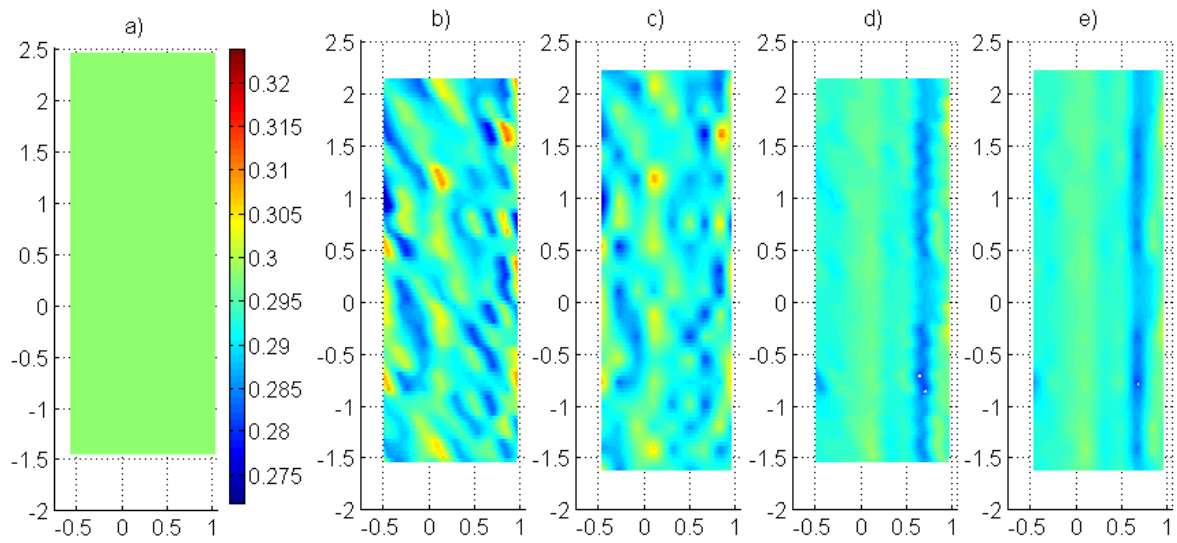


Figure 54 Circumferential strain results (direction shown by arrow) for test 4: a) ANSYS strain; b) and c) reconstruction results; d) and e) image registration results; b) and d) Green strain; c) and e) Local strain.

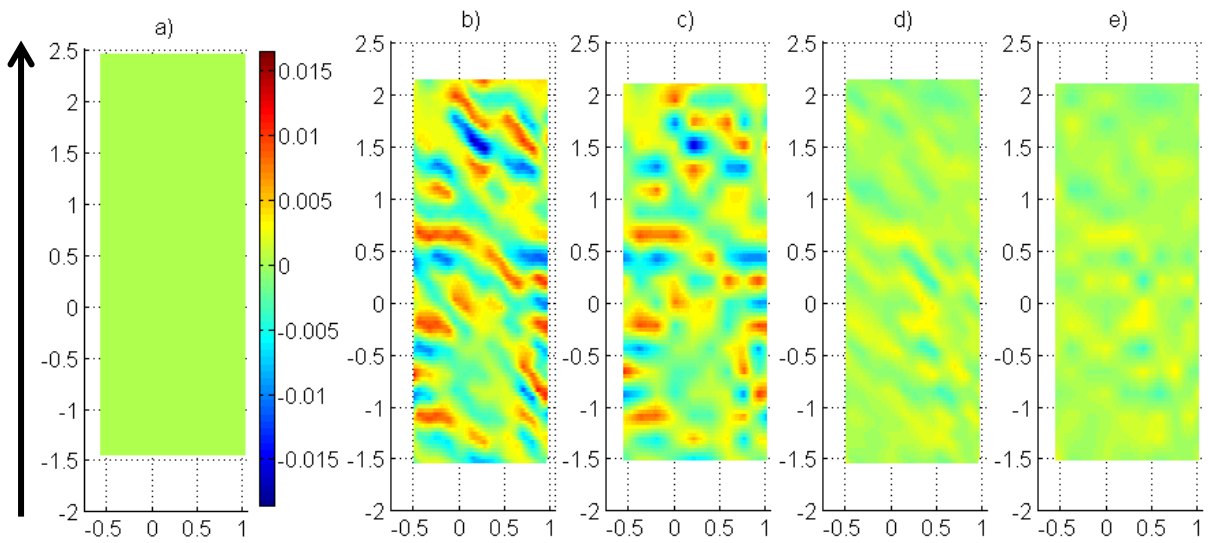


Figure 55 Axial strain results (direction shown by arrow) for test 4: a) ANSYS strain; b) and c) reconstruction results; d) and e) image registration results; b) and d) Green strain; c) and e) Local strain.

Graph 17 and Graph 18 compare results over all four tests reporting the mean and standard deviation error respectively for the circumferential and axial strain. For each test three comparisons of the strain measures are taken into account:

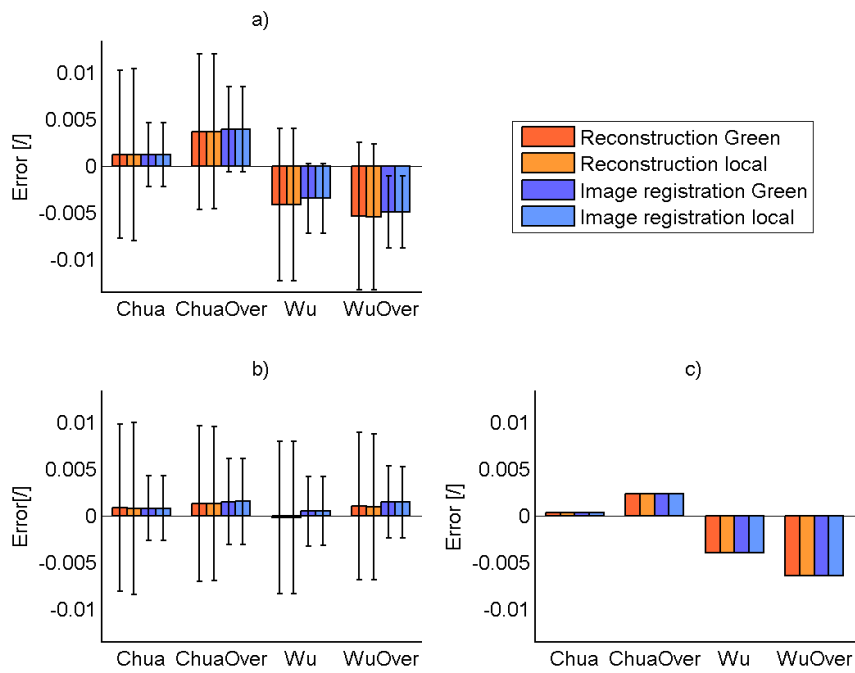
- a) between the values obtained with the photogrammetric method (test data) and ANSYS reported strains;
- b) between the values derived with the photogrammetric method (test data) and the strains calculated from the ANSYS 3D position data using the experimental post-processing (ANSYS derived strains);
- c) between the ANSYS derived strains and ANSYS reported strains.

The numerical values of the errors on strain are reported in Appendix C1 from Table 49 to Table 52; for the deviation formulas see Appendix A1.

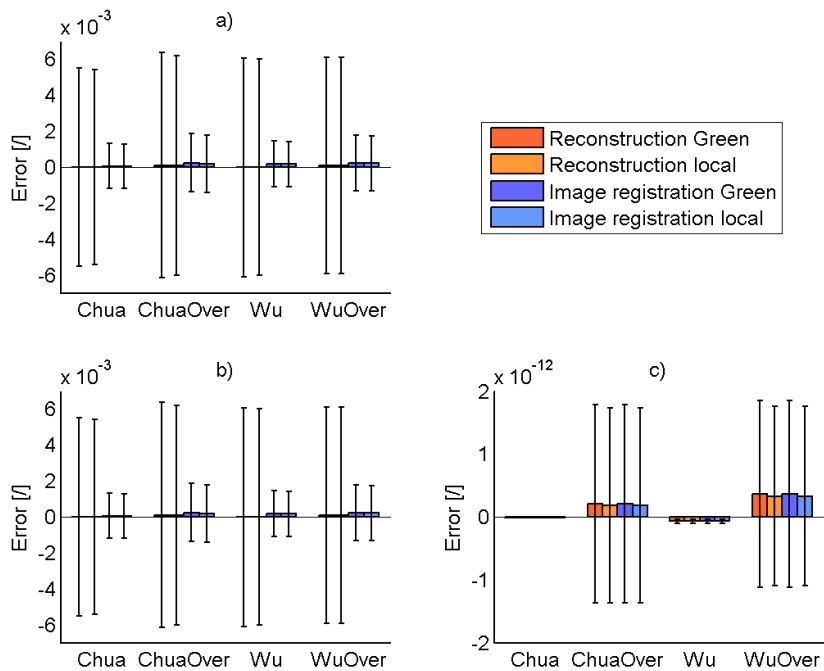
Graph 17 shows that the mean error on circumferential strain is always below 0.005 and the standard deviation is below 0.01 in most cases. The overall error is due both to the calculation procedure and to the acquisition technique since the error on the second comparison is not null.

In Graph 18 it is possible to notice that the total error in the axial direction is lower, in most cases it is below 0.006 and the disturb due to the strain derivation is almost null. The results in this direction are comparable to those obtained for the zero strain test on the Strip geometry where the expected deformation was null as well.

In both directions the influence given by the Green and Local strain measurement is similar, in fact the mean and standard deviation do not change depending on the calculation approach. The image registration is effective in reducing the standard deviation in all the cases and it is confirmed as the better technique between the two analysed in this work. The response is slightly different among the materials, especially in the hoop direction, and this is noticeable in the mean errors. This discrepancy could be the effect of different levels of deformation in the four tests.



Graph 17 Error on circumferential strain: a) test data vs. ANSYS reported data; b) test data vs. ANSYS derived data; c) ANSYS derived data vs. ANSYS reported data.



Graph 18 Error on axial strain: a) test data vs. ANSYS reported data; b) test data vs. ANSYS derived data; c) ANSYS derived data vs. ANSYS reported data.

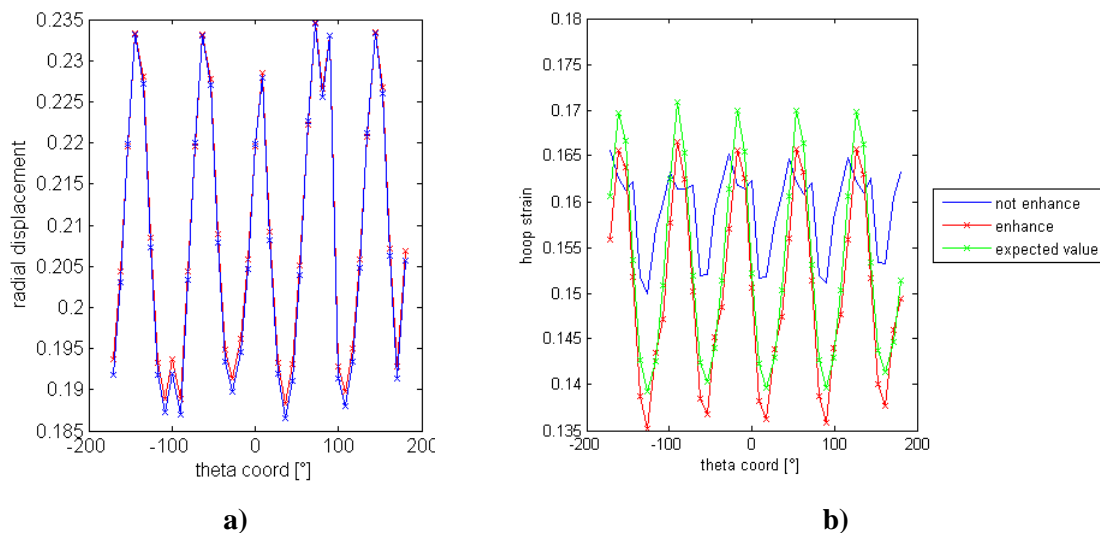
3. Stented vessel

This section illustrates the results of tests undertaken on the Stented vessel geometry. Preliminary results are first reported to show the influence of element formulation and to assess mesh sensitivity. The symmetry of the strain distribution in the full vessel model is also analysed in the preliminary investigations. This section is followed by the results derived from the main test and the comparison between the manual reconstruction and image registration techniques.

3.1 Preliminary tests

3.1.1 Bending problem

Graph 19 shows the comparison between the computational solutions obtained respectively with the enhanced strain option and the default element formulation. The two measures taken under consideration for this investigation are the ANSYS displacement (Graph 19a) and strain (Graph 19b) in the Stented vessel model. For this analysis a coarse mesh was used (Mesh A). In Graph 19b is also represented the expected value of strain calculated with the formula that consider the radial displacement as the unique cause of the circumferential strain.



Graph 19 Comparison between enhanced strain and default element formulation a) ANSYS radial displacement b) ANSYS hoop strain

As shown in Graph 19a the agreement between the displacements computed with the two different formulations is in good agreement, since the enhanced and default options do not affect the displacement acquisition by ANSYS. The Graph 19b shows that the strain calculated with the enhanced strain formulation follows the expected trend of deformation; instead the default option strain evidently differs from the analytical values.

The enhanced strain presents some variations from the theoretical measure in correspondence with the maximum and minimum values, due to the initial hypothesis and approximation made by the analytical formula.

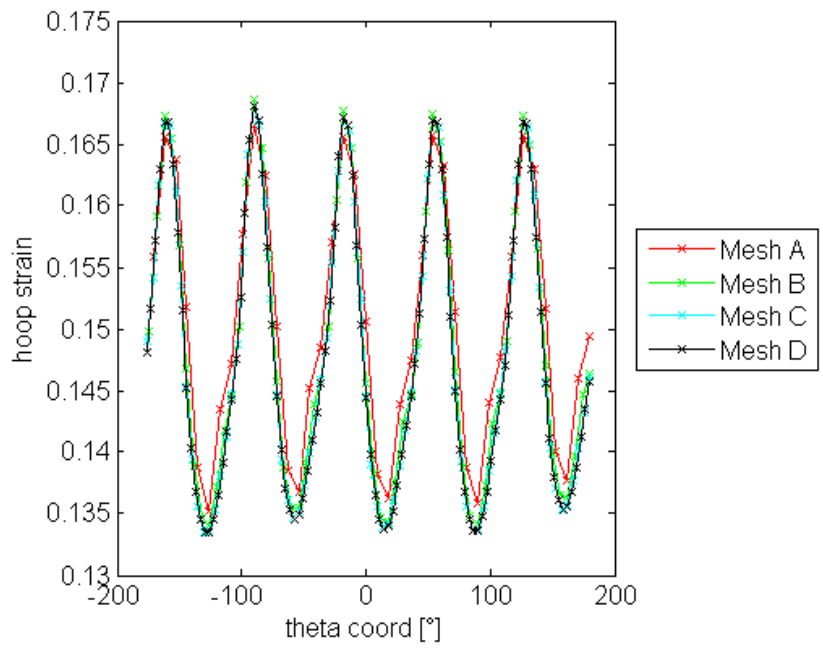
3.1.2 Mesh sensitivity test

The mesh sensitivity test was performed to determine the best mesh which optimised the goodness of the solution and the computational time required to run the simulation. As already exposed for the Vessel geometry *Results*, the mesh was first tested in the circumferential direction and through the thickness, then the axial number of elements was refined.

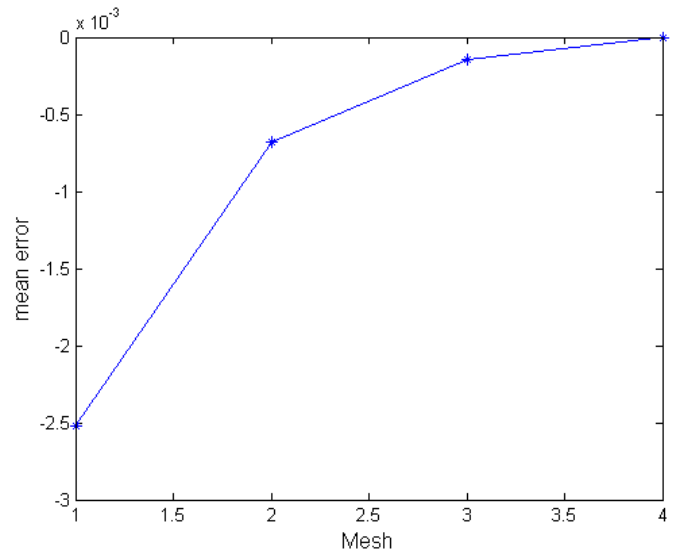
Graph 20 shows the trend of the ANSYS circumferential strain on a middle ring for four different meshes at the end of vessel expansion. The meshes range from a coarse to a fine mesh gradually refined in the circumferential and radial direction (Mesh A, Mesh B, Mesh C and Mesh D).

Graph 21 reports the mean error on the ANSYS hoop strain calculated as the mean difference between the results given by each mesh type and the reference Mesh D. Mesh D is taken as the reference mesh because of its higher fineness and the solution obtained in this case is considered to be the golden standard.

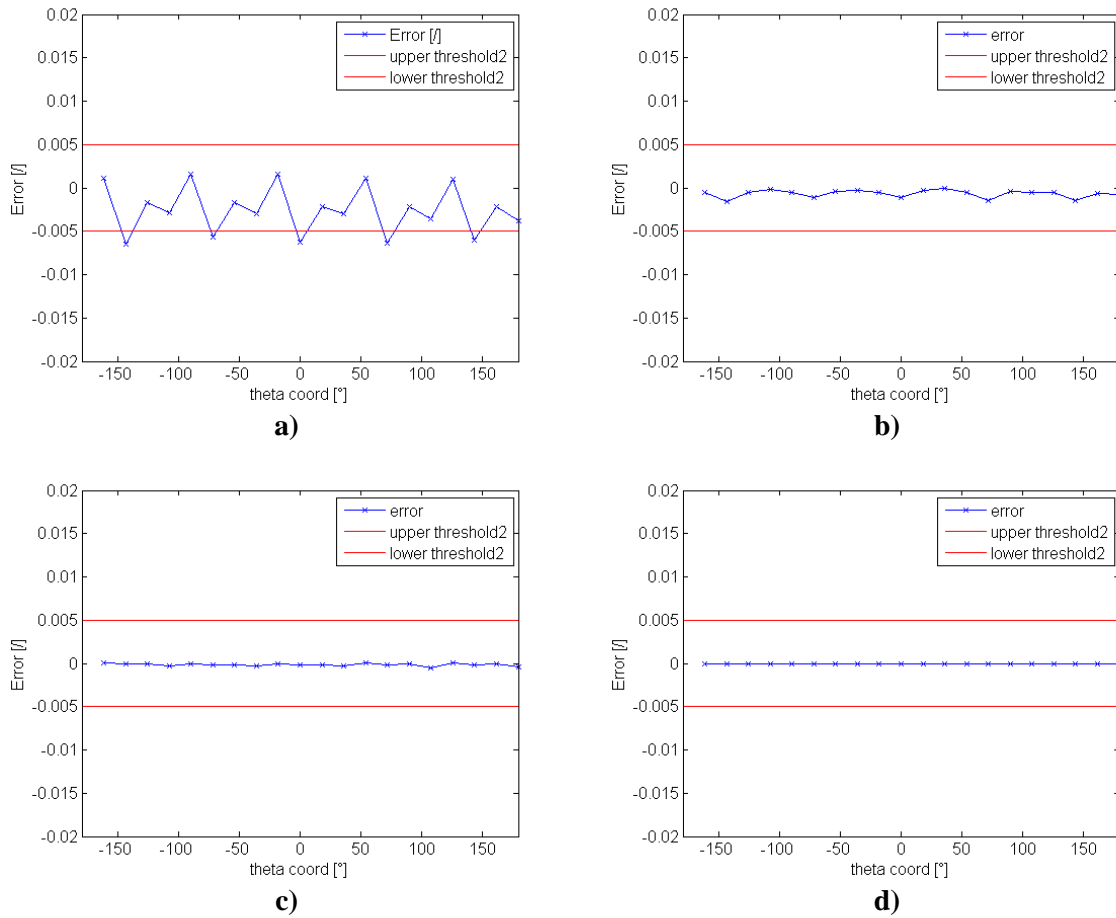
Graph 22 illustrates the absolute error on the ANSYS circumferential strain at the variation of the theta cylindrical coordinate. The error value is computed as the deviation between the results given by each mesh type and the reference mesh at every angle of the geometry. The red lines represent the threshold of strain deviation and they are equal to ± 0.005 . If the errors are all included between the two lines the analysed mesh is considered to provide a solution as robust as that given by the reference Mesh D.



Graph 20 ANSYS hoop strain against theta coordinate. The strain is plotted for each one of the four meshes with different numbers of elements in the circumferential and radial direction.



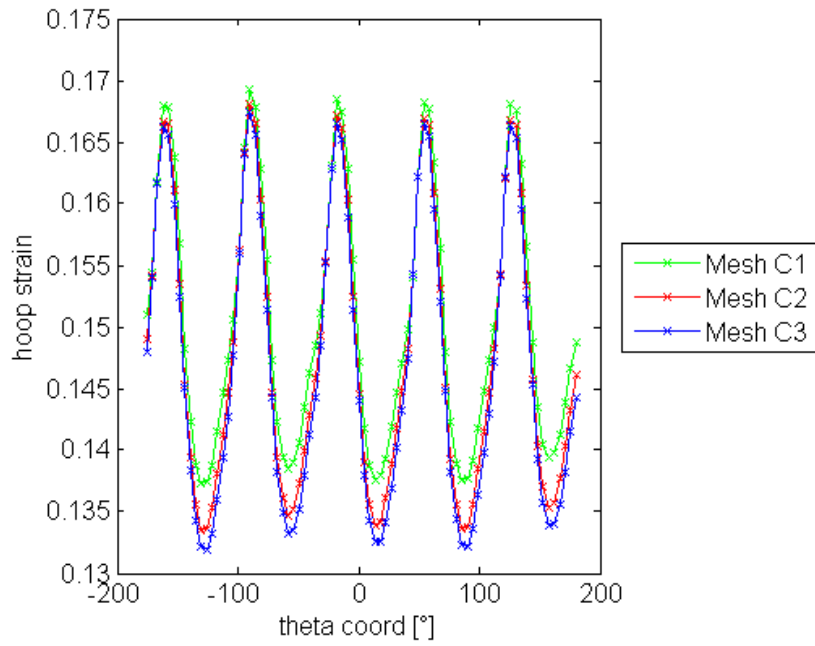
Graph 21 Mean error on ANSYS hoop strain between each mesh and the reference mesh D. Axis x represents mesh type: 1=A, 2=B, 3=C, 4=D.



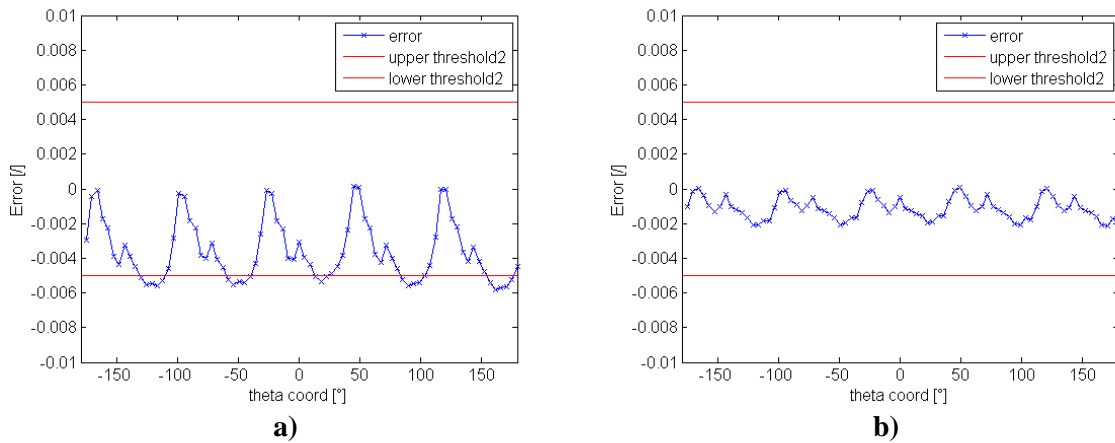
Graph 22 Absolute error between ANSYS hoop strains computed with: a) mesh D and mesh A; b) mesh D and mesh B; c) mesh D and mesh C; d) mesh D and mesh D.

Graph 23 represents the comparison between ANSYS circumferential strains calculated with meshes gradually refined in the axial direction. The circumferential and radial densities correspond to those of mesh type C, hence the models are named C1, C2 and C3 to indicate the increasing number of elements along the vessel axis.

Graph 24 displays the absolute error between the ANSYS circumferential strains given by each mesh type and the reference mesh. The red lines represent the threshold of strain deviation and they correspond to ± 0.005 . In this case the absolute error is calculated taking as golden standard the finest Mesh C3.



Graph 23 ANSYS hoop strain against theta coordinate. The strain is plotted for each one of the four meshes with an increasing number of elements in the axial direction

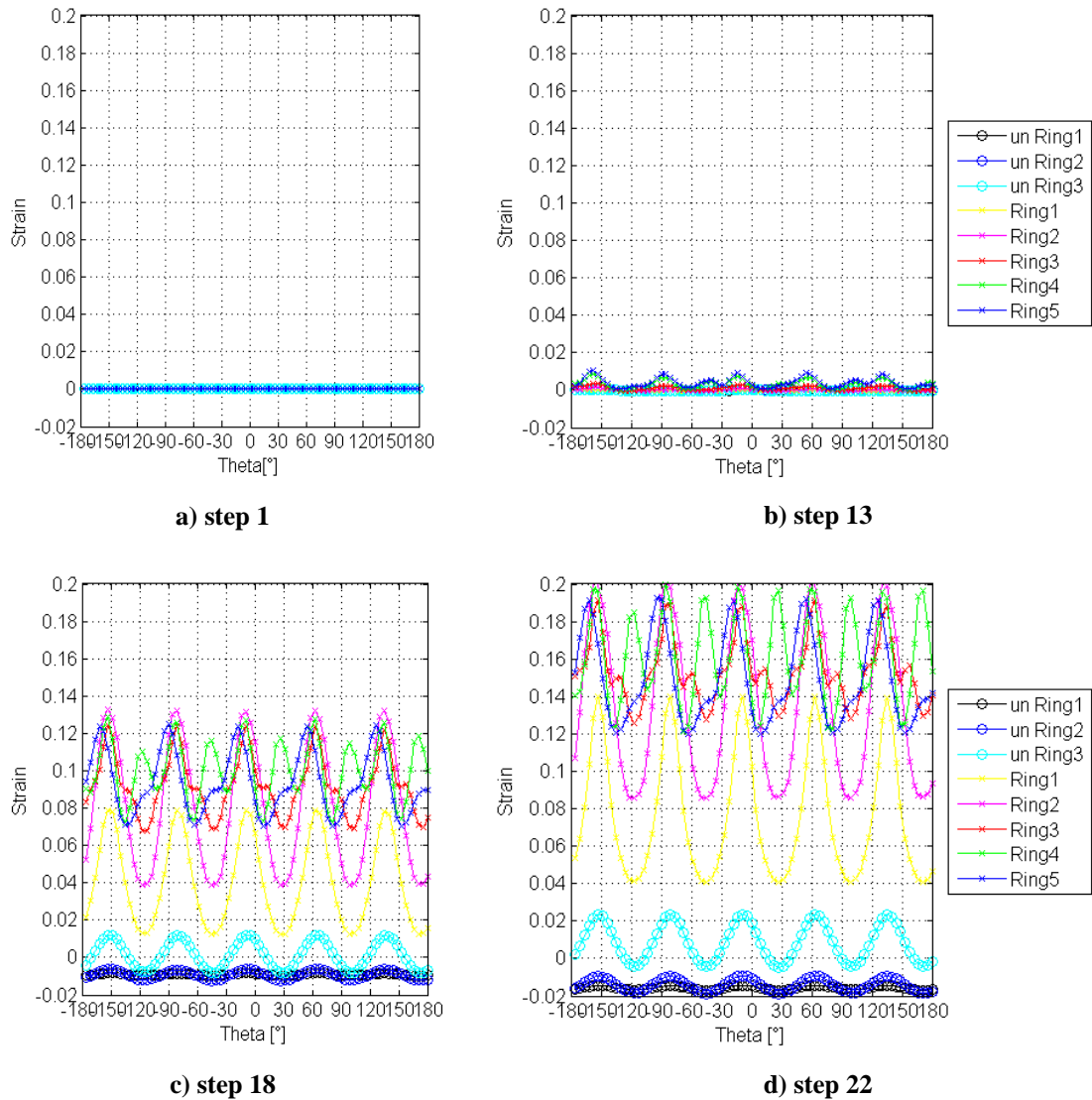


Graph 24 Absolute error between ANSYS hoop strain calculated with: a) mesh C3 and mesh C1; b) mesh C3 and mesh C2.

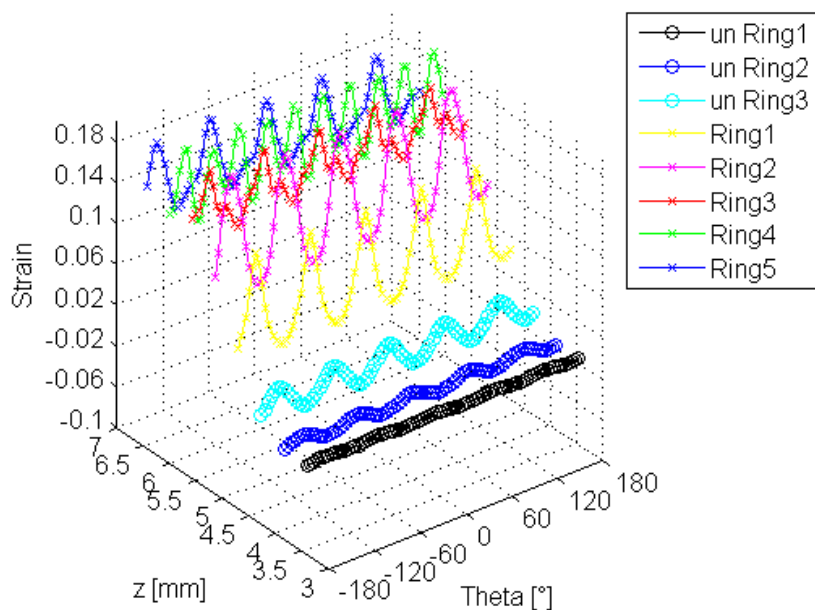
3.1.3 Strain distribution

This test was undertaken to clarify how the strain is distributed along the vessel and explore the influence of the stent presence in the train trend. Graph 25 shows the ANSYS circumferential strain versus the angle in a cylindrical reference system at different substeps of the expansion simulation. The strain values are plotted for each ring of the vessel and are computed using the Mesh C1 detected in the previous chapter (see *Materials and methods* section for the test protocol). The reported substeps represent the instants after the contact between vessel and stent, and step 22 corresponds to the fully expanded stent configuration.

Graph 26 illustrates a 3D image of the strain distributions over half of the vessel along the z direction after full expansion of the stent.



Graph 25 Hoop strain plots against theta coordinate on different rings at different simulation substeps.



Graph 26 Variation in hoop strain distribution along z direction.

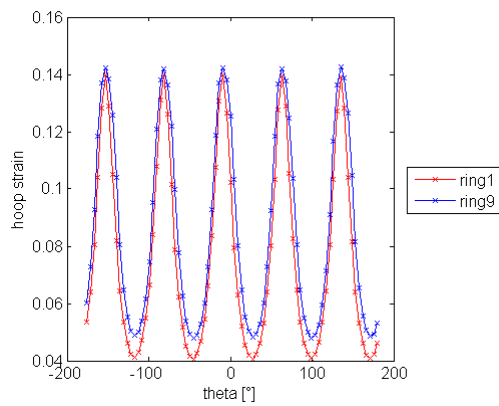
The Graph 25 shows an increase in the strain over the course of the analysis as the balloon pushes the stent further into the vessel wall.

In 3D Graph 26 it is possible to notice that going from the edge toward the medium axial length of the geometry the variation of strain around the circumference becomes remarkable. In fact the circumferential strain increases as the coordinate moves from the not stented region to the part where the stent deforms the vessel and the curve of the strain there is characterised by a sinusoidal trend. This non-uniform distribution in the circumferential direction can be due to the gaps between the stent struts.

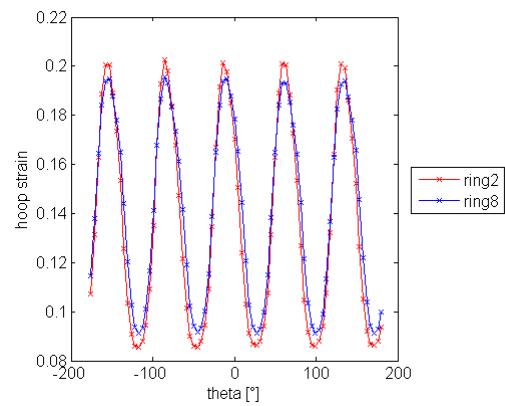
3.1.4 Symmetry

The symmetry test was performed to evaluate if the strains were distributed symmetrically with respect to the middle length of the stented vessel configuration.

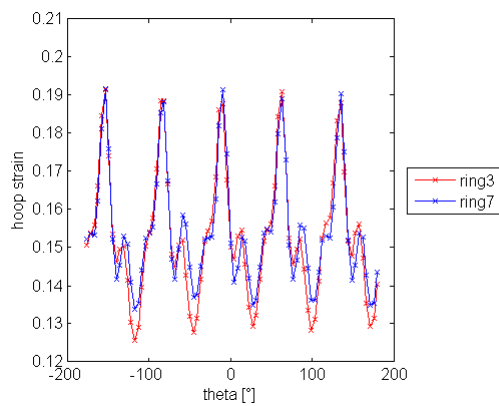
The strain distributions are observed at correspondent rings either side of the center of the geometry on the external surface (see *Materials and methods* for the couples of rings) and the results are compared in Graph 27. The vessel is discretized with the same Mesh C1 provided in the previous tests.



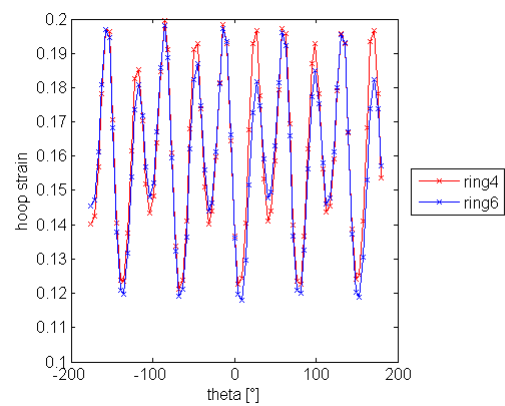
a) ring 1 and ring 9



b) ring 2 and ring 8



c) ring 3 and ring 7



d) ring 4 and ring 6

Graph 27 Circumferential strain comparison between correspondent axial locations.

The 2D plots demonstrate that the general form of the strain distribution is in good agreement either side of the stent, that is the distributions on rings which are symmetrically positioned are correspondent. Though there are some local variations in the strain, especially in correspondence of the maximum and minimum values of the distribution. These discrepancies are due to small deviations from full symmetry in the stent geometry (see Figure 12 in *Materials and methods*) which cause a slightly different expansion of the vessel walls.

3.2 Reconstruction and image registration

This section compares the results obtained using both the manual reconstruction and the image processing methods to derive measures of strain for the Stented vessel geometry. One analysis was undertaken as listed in Table 30 and the evaluation process was applied only to a portion of the stented vessel as shown in Figure 56.

Geometry	Material	Simulation	Calibration	Element
C	2	f	12	SOLID185

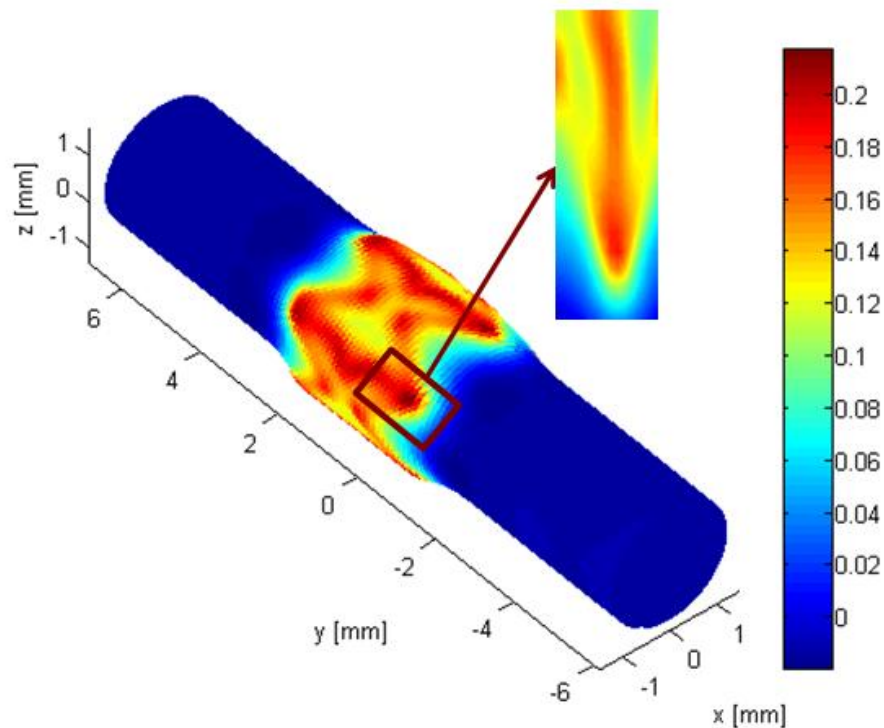


Figure 56 ANSYS circumferential strain on the entire geometry and selected patch.

Figure 57 and Figure 58 report the contours of strain in the circumferential and axial directions. Each figure provides five strain contour plots: the first graph is the ANSYS reported strain, the second and third distributions represent the Green and Local strains obtained from the manual reconstruction data, the fourth and last plots illustrate the Green and Local strain measures derived from the image registration nodal coordinates.

The contour plots present a rectangular shape although the stented vessel is a tridimensional geometry because the analysed patch is represented from a frontal point of view. The curved features are not visible from this perpendicular perspective but they were taken under account in the data processing.

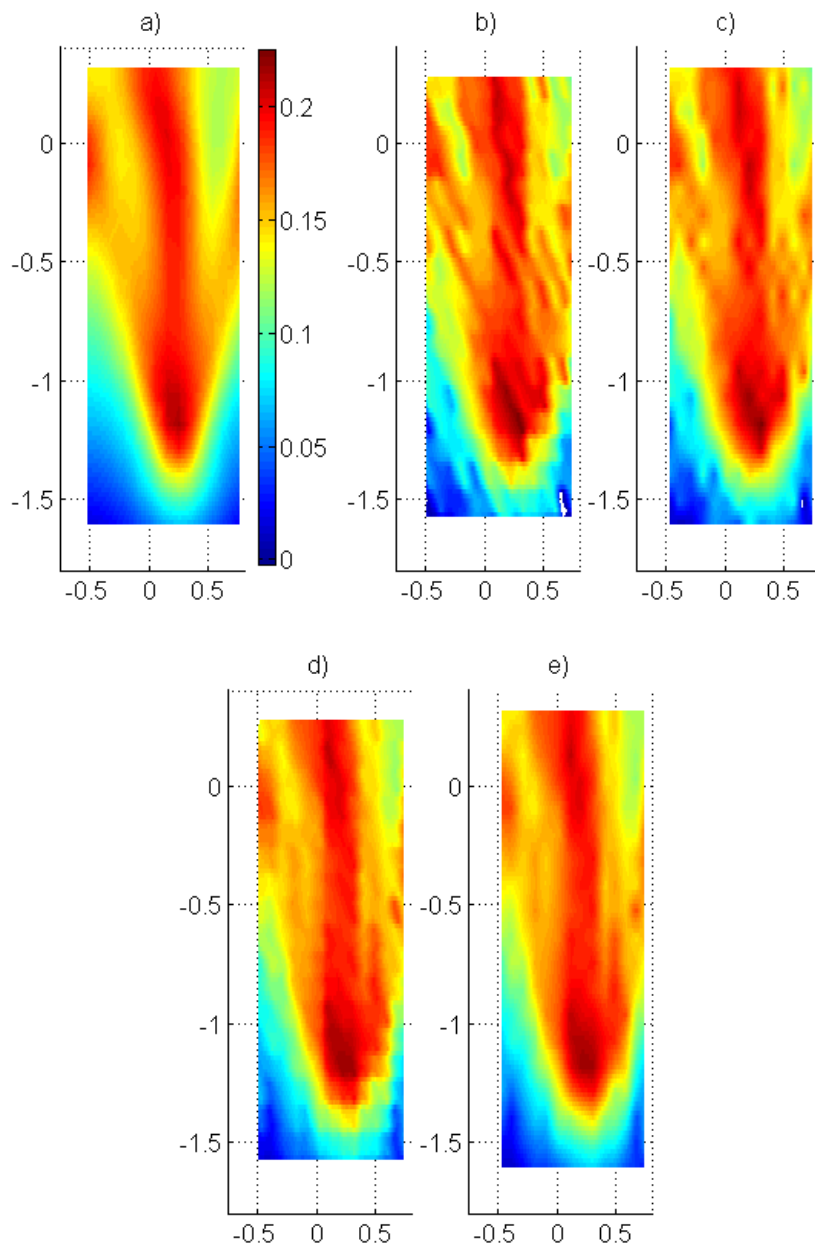


Figure 57 Circumferential strain results (direction shown by arrow) for test 1: a) ANSYS strain; b) and c) reconstruction results; d) and e) image registration results; b) and d) Green strain; c) and e) Local strain.

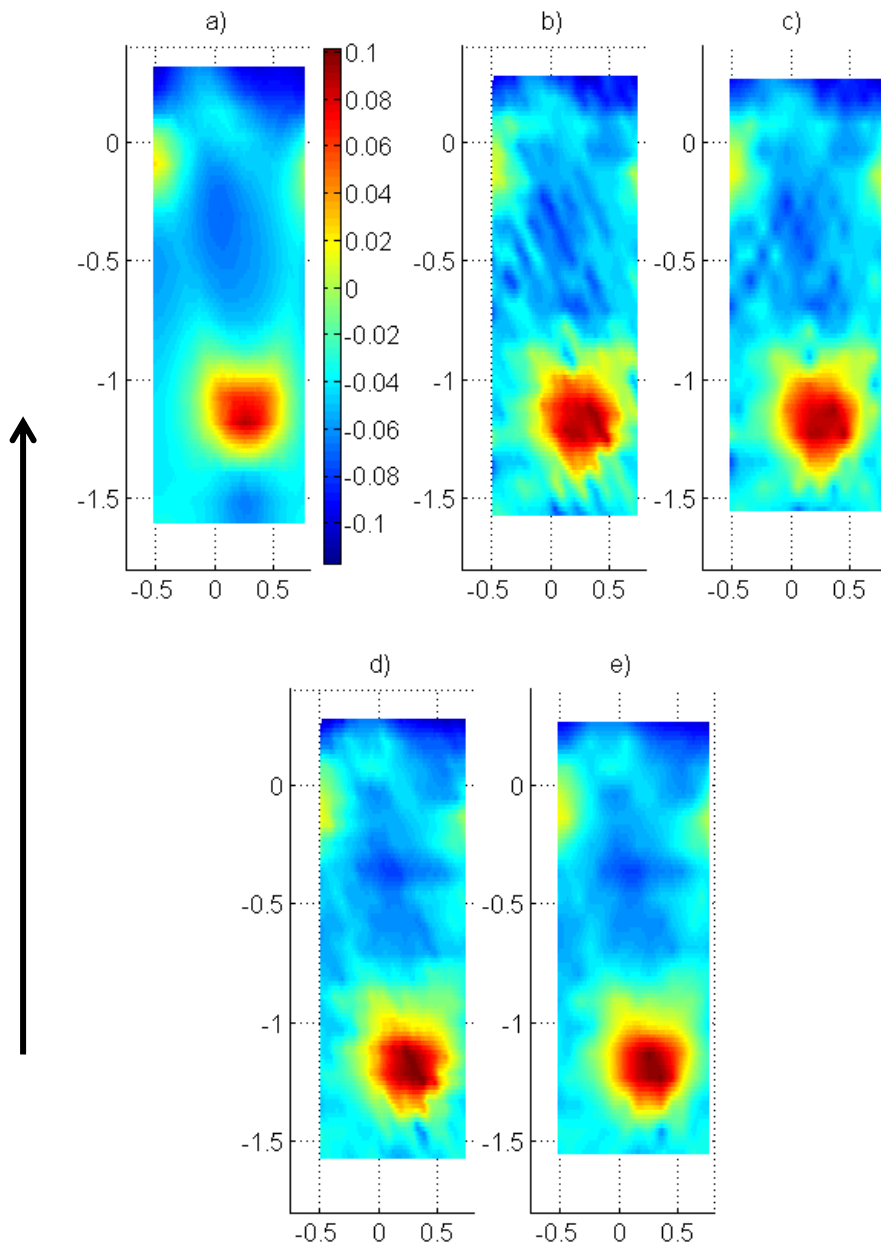


Figure 58 Axial strain results (direction shown by arrow) for test 1: a) ANSYS strain; b) and c) reconstruction results; d) and e) image registration results; b) and d) Green strain; e) and e) Local strain.

As already reported for the Strip and Vessel geometries the size of the contour areas is different for each plot. This is due to the fact that every calculation method employs a different number of points' coordinates to obtain the strain, therefore the covered areas result various. The Global strain approach computes the lowest amount of strain data while the Green strain method produces the highest quantity of strain values.

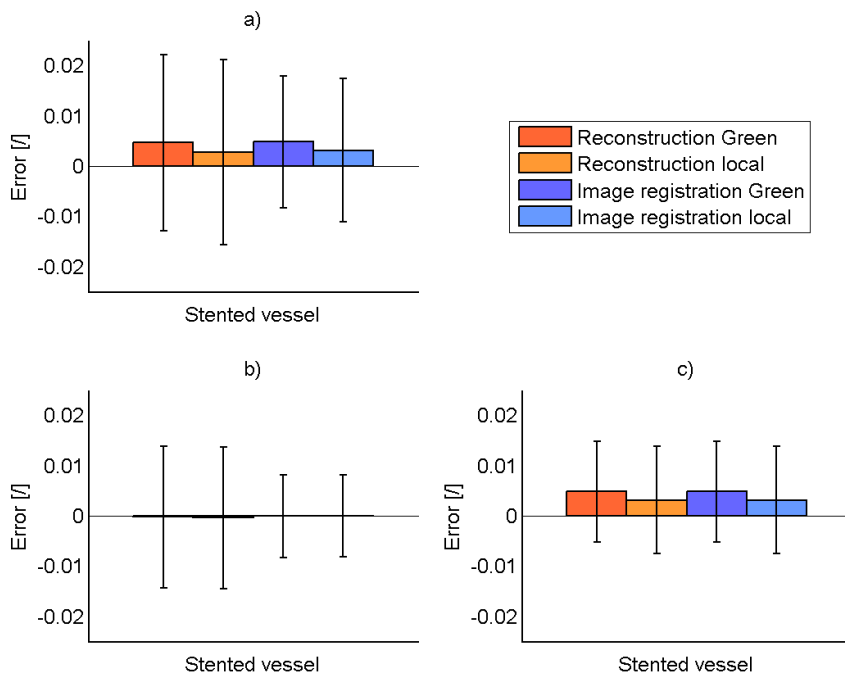
Figure 57 and Figure 58 show that the strain measurement on the Stented vessel is disturbed by noise as underlined also in the previous geometries. In fact the Green and Local measurements report deviations from the expected values and the contour plots are characterised by peaks and vales of strain. The level of noise appears reduced when using the image registration rather than the manual reconstruction to pick the points, confirming the robustness of the semi-automatic acquisition method.

Comparing the circumferential and axial contour plots it is noticeable that the magnitude of strain is different, in fact the maximum hoop strain is more than two times maximum axial strain. Furthermore the circumferential strain is mainly positive which is consistent with the expansion, while the axial strain is symmetrically distributed around zero. This means that during the inflation the vessel is subjected to both tension and compression along its axis. Also the spatial distribution of the strain in the vessel wall is different in the two directions and this is related to the influence of the structure of the stent. The axial strain has a spotted peak surrounded by negative values while the circumferential strain is featured by a stripe of higher measures which gradually decrease to lower values.

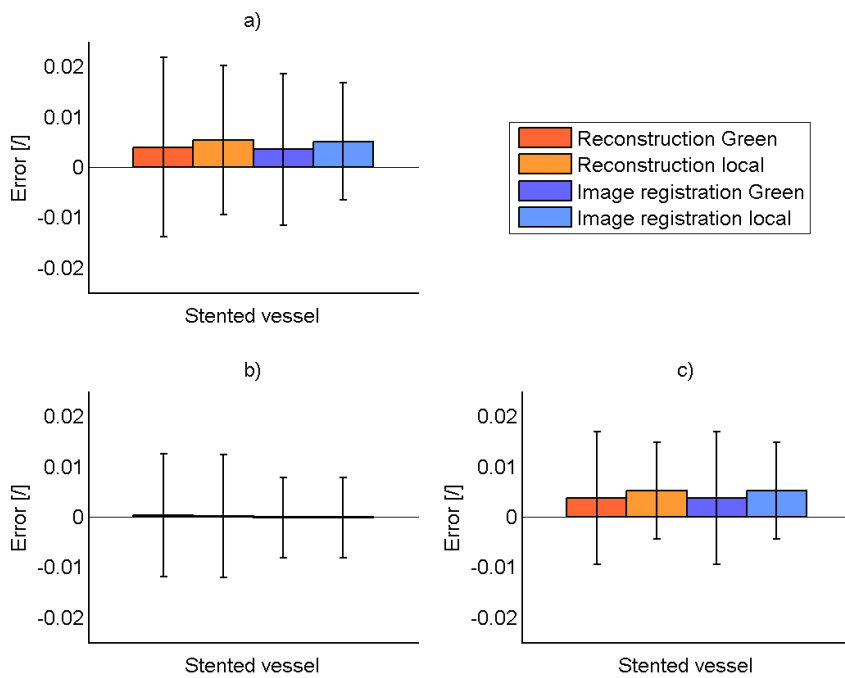
Graph 28 and Graph 29 analyse results over all four tests reporting the mean and standard deviation error respectively for the circumferential and axial strain. For each test three comparisons between strain measures are taken into account:

- a) values obtained with the photogrammetric method (test data) and ANSYS reported strains;
- b) values derived with the photogrammetric method (test data) and the strains calculated from the ANSYS 3D position data using the experimental post-processing (ANSYS derived strains);
- c) ANSYS derived strains and ANSYS reported strains.

The numerical values of the errors on strain are reported in Appendix D1 in Table 54. The errors are computed with the formulas in Appendix A1.



Graph 28 Error on circumferential strain: a) test data vs. ANSYS reported data; b) test data vs. ANSYS derived data; c) ANSYS derived data vs. ANSYS reported data.



Graph 29 Error on axial strain: a) test data vs. ANSYS reported data; b) test data vs. ANSYS derived data; c) ANSYS derived data vs. ANSYS reported data.

Graph 28 and Graph 29 show that the mean error on circumferential and axial strain is generally small and the standard deviation is below 0.020 in most cases. The overall mean error is mainly due to the strain calculation formula as it is possible to deduce analysing the second and third bar plots. In fact the error produced by the comparison between the ANSYS derived and reported values has the same trend of the total error (graph a). Instead the mean error between the ANSYS derived and test data tends to zero and this suggests that both manual reconstruction and image registration do not provide systematic errors. The standard deviations are comparable in all the cases due to the system noise.

In both directions the influence of the Green and Local strain measurement is similar, in fact the mean and standard deviation do not change depending on the calculation approach but more on the direction of interest. The image registration is effective in reducing the standard deviation in most cases, although the improvement is not evident as in the previous tests especially in the axial direction.

Discussion

This section discusses the results presented in the previous chapter. Results are discussed in the context of each individual geometry.

1. Strip

1.1 Noise

Graph 6e, Graph 6f, Graph 6g and Graph 6h show that the error in the transversal strain is higher at the final step than at the middle one. In the longitudinal direction Graph 6a, Graph 6b, Graph 6c and Graph 6d show that deviation between the ANSYS strain and the data with artificial noise remains the same from the middle to the final step.

Referring to Table 33 and Table 34 in Appendix B, the absolute mean error on transversal strain is 0.026 at middle step and 0.040 at final step, with a notable increase in the variation of the deformation. Instead the absolute mean error in the longitudinal directions goes from 0.027 to 0.022. This shows that the error on the position has less influence in the principal direction of deformation as larger strains are generated in the longitudinal direction, in fact an error on position has more influence if the displacement is lower.

It is remarkable that the error obtained with the two different approaches, Local strain and Green relationship, is comparable in both directions which suggests that the two formulas are equally sensitive to errors in the position data.

The strain error shows how the error on the position propagates to derived strain values. With both the strain measurement methods a mean error of 6.20% on the transversal

position results in an error of 52.5% on the Green strain value and of 54.6% (see Table 27) on the Local strain measure at the middle step of deformation. At the final step the percentages decrease becoming respectively 42.04% and 40.32%. This indicates that the percentage error increases about nine times passing from the position to the strain.

In the longitudinal direction a mean position error of 5.50% results in a strain error of 26.05% at the middle step and of 9.58% at the final instant. In this case the increase of the percentage error is about five times in the middle step and doubles at the final step. This confirms that at higher levels of strain the accuracy on the position has a significantly lower impact. The absolute value of strain, at the end of the expansion, in transversal direction is -0.1 and in longitudinal direction is 0.2.

The results reported above demonstrate that the post-processing method is sensitive to the noise on the position, which can result in large errors on the strain, and the degree of error depends on the level of deformation in the specific direction. This test highlights the importance of precise acquisition of the nodal position during the reconstruction phase. This has implications for the results obtained from other analyses where the relative accuracy of each method for the detection of surface points (manual picking vs. image registration) is investigated.

1.2 Resolution test

The plots in Graph 7 illustrate that along the transversal direction the strain values calculated at different levels of resolution are scattered around the expected value given by ANSYS. The level of scattering does not change significantly from the middle to the final step and also the position of the node does not influence the results obtained.

Graph 8 represents the strains in the longitudinal direction at two different steps of deformation and it is notable that the scattering decreases between the middle and final step and also the nodal position appears to have an influence on the deviation of the values. In fact the lateral points are affected by a larger scattering of the data around the expected value which could be due to non-uniform strain along the geometry. It was also visible that the farther a point was from the center of the image, the greater the error given by the manual reconstruction process was. In the longitudinal direction the level of deformation is higher than in the transversal direction and this affects the results.

In all the four plots commented above, the strain values obtained from images acquired at a resolution of 2400 pixels are evidently closer to the expected ANSYS value than the strains

calculated with images at 1020 and 1200 pixels. This is supported by Graph 9 that shows the absolute error in the transversal and longitudinal direction as the mean value plus the standard deviation. In both directions the mean value of error with 2400 pixel is lower than the other means and also the standard deviation decreases. For example at the final step of deformation the standard deviation of the transversal strain error is 0.0103 for the 1020 pixel acquisition and 0.0041 for the 2400 pixel images. Improvement is even higher in the longitudinal direction where the standard deviation changes from 0.0069 for images at 1020 pixels to 0.0016 for 2400 pixel acquisitions. Once more this suggests that the principle direction of strain suffers less of errors due to the accuracy of point reconstruction.

The data in Graph 9 shows little improvement in the strain measurement is observed when image resolution increases from 1020 to 1200 pixels, while when the pixels double from 1200 to 2400 the error is evidently lower. This outcome determines the importance of a good image resolution for the accuracy of strain measurement and therefore the following tests have been performed using square images acquired at 2400 pixel of resolution.

1.3 Global strain

The plot in Figure 39 illustrates the trend of longitudinal strain at different steps of deformation along two separate lines on the strip geometry. It is possible to notice that along line 1 the strain is subjected to a larger variation while on line 2 the deformation remains more uniform, at both levels of deformations. This has an influence on the Global strain measurement since the calculation performs averaging over a set of points and if it is applied in regions of significant local strain variation over-averaging of strain may occur resulting in a loss of information. The number of interpolated points used is also important for this reason.

Observing Graph 10 it is notable that the first and second methods (which use averaging of strain over 3 local points) are less suitable because the scattering (mean plus standard deviation) is significantly higher than those observed the other methods (which use 5 local points). In fact at the final step of deformation the absolute error along line 2 for the first and second method is equal to 0.0031 and 0.0034 while the error on the third and fourth method is respectively of 0.0018 and 0.0026. In fact averaging over three points maintains the magnitude of error noise related with the local strain measure.

Between the third and fourth methods variable results are obtained. At the middle step the standard deviation of the error related to the third procedure is always greater than that obtained with the fourth method and it goes from 0.0017 to 0.0011 for the first line and from 0.0016 to 0.0013 for the second line. At the final level of deformation for line 2 the standard deviation of the errors using the third approach is lower than that obtained using the fourth method (0.0018 against 0.0026). Also the trend of the mean values is not consistent. This means that there is not a substantial difference between the two procedures and the extent of the error is related to the local variation in strain, therefore it is not possible to predict in advance how well the calculation will approximate the values.

However, the fourth method causes a big loss of information because the displacements are averaged over five points in a serial order which results in only five strains over 24 reconstructed points. In comparison the third method provides 20 values of strain over the same 24 reconstructed points.

In general, the error does not vary significantly between the two analysed columns at different steps of deformation. Graph 10 demonstrates that the magnitude of error for each line is comparable over all methods. This suggests that the level of deformation has a low influence on the Global strain procedure.

The best trade-off between smoothing the errors due to the point reconstruction and capturing the strain distribution is obtained using method 3 as this approach gives a low absolute error but provides a higher amount of strain values compared to the method 4 which causes a big loss of information. As a result, method 3 has been used for the calculation of the Global strain in the main strip test.

1.4 Reconstruction and image registration

The strip geometry was implemented to assess the strain errors obtained during reconstruction of a simple 2D configuration. The specimen was fixed on the upper edge and the lower edge was displaced of 5 mm in all the trials. The material property of the strip was changed in the different tests: in the first two cases a linear elastic material was modelled and in the third trial a hyperelastic constitutive law was applied. The fourth study is a zero strain test performed to quantify the influence of the manual picking operation.

1.4.1 Graphical strain distribution

The full-field strain distribution shown in Figure 40 illustrates the transversal strain on the strip geometry detected with the reconstruction and image registration methods for test 1. The maximum and minimum values of compressive strain reached in this test are 0.100 and 0.035. The Green strain distribution (b,e) is affected by significant noise throughout the geometry, in particular on the upper and lower edges. This is possibly due to limitations of the Green formulation to describe the transversal strain in regions where large shear strains are present. This is the case for the strip since the geometry is subjected to a significant shear strain. The Local strain procedure (c,f) is also affected by noise but the strain on the upper and lower areas is better represented. The plot which best approximates the ANSYS data is the Global strain distribution (d,g), in fact the values seem to match the expected data. Nevertheless the evaluated points are less than in the previous cases because of averaging over five points which excludes the lateral edges.

The comparison between the reconstruction and image registration on the transversal strain shows that the second technique causes a lower noise on the measurement. From the plots it is remarkable that the distributions better approach the ANSYS graph, maintaining the issues underlined above. In particular, the value of strain is higher than the expected along some concentrated vertical bars rather than as clusters of random noise.

As regards the transversal strain in tests 2 and 3 the observations are similar to those already reported for the first protocol.

Figure 41 reports the distribution of longitudinal strain in test 1 using different post-processing methods. The strain remains in a range between 0.1534 and 0.1929. In the manual reconstruction case the Green (b) and Local (c) strain seem to be affected by large noise which causes peaks of strain throughout the geometry without any similarity with the ANSYS values. Instead the Global strain (d) presents two areas of higher strain as expected and in general the distribution is well represented. Nevertheless there is a loss of information at the edges of the geometry because the evaluated points are reduced due to the averaging procedure.

In the image registration analysis the distribution of strain in all the three cases is improved due to the reduction of noise in the acquisition method. Noise in the derived strains is still significant in the Green and Local strain while the Global strain seems to best approach the ANSYS reported values. In particular the Green and Local strain present a sand-glass

shape with lower strains in the middle part as expected but not at this magnitude. This behaviour could be due to the image registration technique, in fact preliminary tests showed that this acquisition process begins to fail in regions where the displacements are higher and in this case the observed region corresponds to the greatest values of deformation.

The same observations are valid for the test 2 in the longitudinal direction (Figure 43). This similarity is due to the fact that the two models have the same constitutive law, linear elastic but the Poisson ratio does not change significantly, in fact in the first case is 0.49999 and in the second is 0.49. Since this reason and because of the displacement boundary condition applied, a greater strain variation cannot be detected. As regards the test 3, the transversal strain is comparable to the one analysed for the test 2, while the longitudinal strain presents a different magnitude from those observed above. In fact the ANSYS strain varies from 0.1651 to 0.1883. This difference is due to the material which is hyperelastic isotropic, then the strip deformation is more uniform along the longitudinal direction and there are less strain peaks. The overall strain distribution results more smoothed.

The stereophotogrammetric technique does not seem to improve the measurement accuracy with the variation of the material, in fact the noise distribution on the geometry has the same features than in the previous observations.

Figure 46 and Figure 47 represent the transversal and longitudinal strain in the *zero strain* test. The expected values are zero, since the geometry is subjected to a translation without any deformation. Nevertheless the technique produces noise which results in a fictitious strain of the order of 10^{-3} for the reconstruction and 10^{-4} for the image registration. This demonstrates the improvement introduced by the use of the image registration acquisition.

In both directions the manual reconstruction induces errors which are uniformly distributed along the strip. The Green and Local strains are affected by higher errors while the Global strain presents lower errors due to the smoothing action of the strain averaging. The plots related to the image registration show a decrease in the noise magnitude but in the transversal direction it is possible to notice the same vertical bars seen in the previous tests and in the longitudinal direction two regions of concentrated minimum and maximum strain are observed close to each other in the middle of the strip.

1.4.2 Error plots

Graph 12 and Graph 13 report the absolute error on strain expressed as the mean value plus the standard deviation calculated on the whole population of errors. Every figure contains three plots which show the comparison between strains computed from different sources: a) is obtained between the values of the photogrammetric method and ANSYS data; b) is deduced between the photogrammetric method data and strains calculated from the ANSYS position data; c) is considered between the ANSYS derived strains and ANSYS data. The error reported in (a) represents the total error on the strain measurement, which takes into account all the sources of error. The error reported in (b) indicates the error due only to the technique accuracy as the ANSYS derived strain is calculated with the same post-processing used for the evaluation process so the measures are affected by any assumptions included in the post-processing in the same way. Finally the error reported in (c) is important because the ANSYS derived values have only the inaccuracy due to the assumptions made during post-processing, while the error due to the reconstruction method is not present at all. Comparison of the ANSYS derived values with the ANSYS data shows how the derived values deviate from the finite element solution as a result of the strain post-processing. The first error includes the second and third comparisons and its mean value is the sum of their means.

Graph 12 shows the absolute error on transversal strains is maximum in the first comparison (a). The Green and Local strains demonstrate larger scattering (mean plus standard deviation) than the Global strain in all the cases, especially in the first and second comparisons. The maximum Green strain scattering error in this direction is 0.0087 for the manual reconstruction reducing to 0.0056 in the image registration case; also the Local and Global strain are positively influenced by the IR (0.0080 against 0.0044 and 0.0025 against 0.0013). The non-zero values obtained in the second comparison demonstrate that a component of the error is given by the ability of the technique to accurately reconstruct point positions. The maximum scattering between test and ANSYS derived data is given by the Green and Local strain using manual reconstruction and it is equal to 0.0081. The scattering error introduced by the strain post-processing shown in Graph 12c is in the worst case 0.0037. The comparison between the material models shows that the mean absolute error is affected by variation in properties but the scattering value remains unchanged. The larger mean error is observed in the test 3 (-0.0011), this may suggest that where the strains

are lower, like in this case, the technique struggles to measure them and the result is not as accurate. In fact the first two tests have a lower mean error and their transversal strains are slightly higher (for test 3 the mean strain in transversal direction is -0.0852 instead for test 1 is -0.0878 and for test 2 is -0.0859). The standard deviation does not vary significantly between the different trials (~0.0080) which is consistent with the effect of the random noise introduced by the technique.

The error on the longitudinal strain (Graph 13) reflects the same observation made for the transversal directions with some differences. First of all the decrease of error from the manual reconstruction to the image registration is greater, in fact the scattering error detected in the first comparison decreases by around 0.0030 with change in acquisition technique while the transversal absolute error reduces by around 0.0023. Secondly the absolute scattering is lower than in the transversal direction, in fact the maximum error is detected in the test 3 processed with the Green strain and it is equal to 0.0062. Finally comparing the data presented in Graph 13a, b and c underlines that the error due to the technique inaccuracy is quite low, in fact in the plot the mean values tend to zero: the Green strain error is about 0.0005 in the third comparison and about 0.0001 in the second comparison. This means that in the longitudinal direction the error is principally due to the assumptions in the strain post-processing. The higher standard deviation in the second comparison represents the random noise introduced by the reconstruction approach.

A special case is represented by test 4 where the expected strain values are zero, since the geometry is translated and not stretched. In both directions the third comparison shows that the error due to the formula is null while the entire error is introduced by the inaccuracies due to the reconstruction technique and to the picking point skill of the operator. In fact the order of magnitude of the test 4 error is 10^{-3} as observed in previous tests. The worst absolute scattering error is observed with the Green strain using the manual reconstruction and it is equal to 0.0062 for the longitudinal direction and 0.0060 for the transversal. This indicates that since the expected strain is zero everywhere the influence given by the technique is the same in both directions and there is not a preferential direction for this error. Also in this case the use of Global strain formulation and image registration give a significant improvement to the measurement, decreasing the error from 0.0062 to 0.0012 in the first case and from 0.0062 to 0.0013 in the second observation.

2. Vessel

2.1 Expected values

The thick-wall theory observation was made to control how ANSYS calculates the strain values and the simple vessel geometry offered a convenient configuration to perform this check. The thick-wall cylinder theory was applied to the nodal coordinates given by ANSYS and the material model was specified as isotropic and linear elastic. In the ANSYS simulation the pressure applied to inflate the vessel was a linear function of time as shown in Graph 14a.

Graph 14b and Graph 14c illustrate the radial and circumferential strains with increasing pressure. In both cases it is evident that the values of strain of the ANSYS non-linear simulation start to differ from the other curves after a deformation of about 2% and the final non-linear strain deviates significantly from the linear solutions. The final value of radial strain is -0.0813 for the linear solution and -0.1121 when the non-linearity is taken into account. In the same way the final circumferential strain is 0.0844 in the linear case and 0.1164 for the non-linear response. Not considering these non-linear behaviours means ignoring an important part of the deformation, in the specific case 3% for the radial strain and 3.2% for the circumferential values.

In the present study the non-linear effect must be taken under consideration because of the nature of the problem, in fact the vessels are composed by soft tissues which undergo large deformation and every component of the strain must be included. Therefore non-linearity effects in the ANSYS simulation have been activated in all tests.

As regards the similarity of the ANSYS answer with the expected values Graph 14b, Graph 14c and Graph 14d include the comparison between the computed data and the analytic values. The ANSYS values considered in this case are those related to the linear solution, since the non-linear one has been demonstrated to include the large deformation effects which are excluded from the analytical solution. In fact the thick-wall theory does not give a large strain solution, then it is not possible to generate a comparison for the true strain measure with the ANSYS nonlinear solution.

In the axial direction the expected deformation is null and the computational value reflects this expectation, due to the plane strain boundary conditions. Along the radial and hoop direction the engineering strain provides better agreement with the ANSYS linear solution

than the true strains calculated from the theory. This is due to the fact that when the non-linear effects are turned off ANSYS assumes small deformations and the results are reported as engineering strain. The observation of these plots shows that the analytic strain fits the ANSYS linear solution as expected and this correspondence means that the values given by ANSYS are reasonable when the modelling assumptions are the same (non-linear solution off and engineering strain); therefore the computational method is reliable and comparable with the theoretical formulations.

This conclusion asserts the robustness of the ANSYS solution and the evaluation can be extended for more complex conditions, like the large deformation case or when a stent is expanded within the vessel.

2.2 Mesh sensitivity

The mesh sensitivity plot in Graph 15 shows the effect of a refinement in circumferential and radial direction of the mesh number of elements. The four meshes analysed were chosen to maintain square shape elements. It is visible that the finer the mesh, the closer the strain value tends to a consistent value. The comparison between the ANSYS strain given by the simulation with Mesh D and the other meshes is plotted in the graphs and demonstrates the difference is very low, with a maximum of 0.0005 in the case of Mesh D against Mesh A. If a threshold of 0.005 is assumed accurate enough to capture the variation of strain along the geometry these differences are well below this threshold. After all of these assumptions the coarsest mesh (Mesh A) was chosen.

The mesh was then improved in the axial direction and the plot in Graph 16 and the comparisons between the finer and the other meshes present that there is no solution change among the three set meshes. For this reason, also in this case, the coarsest mesh was chosen.

The mesh used for the following analyses is hence discretised with 40 elements in circumferential direction, 2 in the radial direction and 60 elements in axial direction.

2.3 Reconstruction and image registration

The vessel configuration was analysed to study how the photogrammetric system measures the strain field on a curved geometry and how the accuracy of strain measurement is related to different materials and deformation conditions. Two material models were implemented and each one was expanded first with a pressure of 120 mmHg and then with a displacement of 0.5 mm.

2.3.1 Graphical strain distribution

Figure 49 reports the axial strain along the cylinder calculated by ANSYS (a), with the Green strain formula (b) and with the Local (c) formulation in test 1. The first image refers to the manual reconstruction method and the second is related to the image registration approach. The expected axial strain is equal to zero since the boundary conditions impose a null displacement in this direction. The ANSYS strain has a mean value of $1.1883 \cdot 10^{-14}$ which is considered to be zero. As regards the manual reconstruction the strain varies from a maximum value of 0.0163 to a minimum of -0.0185 both for the Green and Local strain; with the image registration the strain is less variable in fact it goes from -0.0046 to 0.0039. The second technique registers an improvement of one order of magnitude towards the expected value.

The images clearly show local maxima and minima of strain distributed over the geometry in a random way suggesting the presence of noise. In the manual reconstruction this noise is more prominent than in the image reconstruction where the errors seem to be smoothed. There is not a significant difference between the Green and Local strain field and the only visible discrepancy is the shape of the peaks which is more round in the Local strain plot although the order of magnitude is the same.

Since the vessel does not deform axially in any of the four tests all the plots in this direction (Figure 49, Figure 51, Figure 53 and Figure 55) have similar outcomes and the observations made above are valid for every trial (test 2, test 3 and test 4).

In the circumferential direction the test 1 presents images affected by noise which causes the values of Green and Local strain to fluctuate from -0.0042 to 0.0588 in the manual reconstruction case and from 0.0145 to 0.0323 with the image registration technique. The expected value is 0.0249 so the dispersion around it is great; though the reported numbers

refer to the maximum and minimum which include also the outlier values. For a comparison of the mean value see the following chapter (*Error plots*).

Also in this instance the image registration seems to provide an improvement over the manual method. In fact the strain fields reported in Figure 48 are visibly less disturbed by the noise and the deviation from the expected value decreases. The values of strain are distributed as vertical bars along the longitudinal direction of the vessel and this could be linked to the curvature of the geometry.

Test 2 has a computational value of 0.2892 on the hoop strain (Figure 50). The results given by the Green and Local strain range from 0.2727 to 0.3236 for the reconstruction and from 0.2794 to 0.3052 for the image registration. It is possible to see that the range of deviation is not significantly changed in this second test compared to the first one, but the magnitude of the mean strain has increased by one order (0.0262 against 0.2929). The considerations about the strain distribution and the improvement of the image registration are similar to those made for the test 1; nevertheless it is interesting to notice the peak of strain on the right edge of the vessel in the image registration plots (Figure 50) which could indicate an error due to the curvature and strain calculation method.

In the test 3 the properties of the material changed from linear elastic to hyperelastic and the consequence of this choice was that the cylinder deformed much more than in the first trial although the imposed pressure on the internal surface was the same. In fact the ANSYS mean value of circumferential strain (Figure 52) is 0.1488 and this is related to the fact that the hyperelastic material has a lower stiffness, so that at equal load the specimen deforms more. The hoop strain calculated with the Green and Local strain after the reconstruction is between 0.1196 and 0.1694 and the image registration reduces this range of values to 0.1362 - 0.1592. The discussions reported above about the strain distribution are valid also for the plots of the circumferential strain detected in this test with the reconstruction and image registration.

Finally the test 4 shows how the vessel expanded when a displacement was applied on the internal surface in order to simulate an overexpansion. Figure 54 illustrates the circumferential strain at different post-processing relationships and acquisition techniques. The computational value reported on the external surface is 0.2979 and it is constant on the whole geometry. Also in this case the hyperelastic material deformed more than the linear

elastic material at the same boundary conditions and load. The Green and Local strain go from 0.2716 to 0.3131 for the manual reconstruction and from 0.2802 to 0.3033 with the image registration. The discussions made for the test 1 about the strain distribution are similar to those observed for this test.

2.3.2 Error plots

As for the strip geometry every figure contains three plots which show the comparison between strains computed from different sources.

Graph 17 illustrates the three comparisons for the circumferential direction and the reported values are the absolute error on the hoop strain. In particular, the error is expressed as the mean value plus the standard deviation and the sum of these two parameters provides the error scattering. The first comparison shows that the error is larger when the strain increases, in fact the minimum mean error is registered for the test 1 (0.0012) where the expected strain is 0.0249 and it reaches the maximum mean for the test 4 (0.0054) in which the computational strain is equal to 0.2979. These values are absolute and this result does not mean that they have the same influence on the strain measurement, in fact in the first case the error is 5% of the strain value and in the second case it represents 1.8% of the final measure. In this instance the introduction of the image registration does not seem to provide a significant improvement on the mean values in the same test. On the contrary the standard deviations are subjected to a decrease when the IR is used instead of the manual reconstruction. For example in the test 1 the standard deviation on the Local strain goes from 0.0092 to 0.0035 when the image registration is introduced, with a reduction of almost one third. This confirms that the noise error is reduced when the image registration technique is employed.

This trend of the standard deviation is confirmed also in the second comparison where the mean values are lower and most of the scattering is given by the standard deviations. A smaller mean value means that the mean error is principally due to the assumptions in the strain post-processing. The worst mean error is equal to 0.0015 and occurs in the Green strain measurement on the overexpanded vessel. Even in this observation the mean error does not improve significantly when the image registration is used instead of the manual reconstruction, in fact the mean remains constant in the same test. The only test which differs from this comment is the test 3.

Similar to the first comparison the third one shows an increase of the mean error with the magnitude of strain on the vessel. The errors increase from 0.0004 to 0.0064 passing from test 1 to test 4: this could be due to the magnitude of the deformation increasing the error resulting from assumptions in the post-processing methods. This plot demonstrates that the overall error is mainly due to the approximation chosen for the post-processing of the data, in fact the first comparison reflects the trend of the current bar plot. The standard deviations in this case are close to zero (10^{-9}) because the expected strain is constant along the geometry.

Graph 18 illustrates the absolute errors on the axial strain when different components are compared. The first and second plot are substantially the same and this demonstrated that all the error introduced in this direction is due to the technique. The mean value is generally low (0.0002) and the error is given by the standard deviation which is about 0.0060 for the reconstruction and about 0.0015 for the image registration. Also in this case the image registration is confirmed as the better technique for the data acquisition. These values are comparable to those detected for the zero strain test on the strip geometry where the expected strain was also null and there was no dependence of the error from the level of deformation. Therefore this value could be taken as the error due to the operator's ability to manually pick the points on the surface, independently from the magnitude of deformation and the nature of the geometry.

The fact that the main component of the error is represented by the standard deviation means that it is principally due to random noise and there is no systemic error. There is not a significant difference between the four tests, suggesting the error does not depend on the material property, and the Green and Local measurement seem to be affected by a comparable mean error.

The third plot is the comparison between the ANSYS and ANSYS derived data and the values are effectively zero since the standard deviation has order of magnitude 10^{-12} . This result shows that the applied formulas are suitable in this case and do not cause any error on the axial strain.

3. Stented vessel

3.1 Bending problem

The comparison between the ANSYS simulation with the enhanced strain option set and the one with default behaviour highlights that the radial displacement does not change but, on the contrary, the reported hoop strain varies both in distribution and in magnitude of the values. In particular the analysis with default behavior underestimates the minimum value of strain in the vessel. From Graph 19b it's visible how the strain given by the simulation with the enhanced strain option activated is closer to the expected strain value than the other plots. This affirms that, with the bending effects due to the stent expansion in the vessel, the hoop displacement becomes significant and it cannot be neglected in the hoop strain calculation so more accurate results are obtained with the enhanced strain calculation.

3.2 Mesh sensitivity

Graph 20 illustrates the strain results given by ANSYS simulations with different meshes in radial and circumferential directions, maintaining square shaped elements.

As observed with the vessel model, also in this case the finer the mesh, the more the strain value approaches a consistent value. Graph 21 demonstrates how the mean error between gold standard mesh and the others is closer and closer to zero with the increase in mesh density. The difference between the finest mesh, taken as gold standard, with the other three is shown in Graph 22. These comparisons show that discretising the vessel with Mesh B would ensure the results capture most of variations of the strain since the difference is lower than the threshold. Nevertheless the trend of this graph (b) still presents visible deviations so Mesh C was chosen for axial refinement.

Graph 23 shows the comparison between the hoop strain extracted by ANSYS simulations with vessel discretised with incremental number of elements in the axial direction. The analyses between the finest mesh in axial direction with the other two led to use of Mesh C2. Accordingly the vessel was meshed with 80 elements in the circumferential direction, 4 elements in the radial direction and 120 in axial direction.

3.3 Strain distribution

It is observed that the hoop strain, plotted against the theta coordinate, shows a sinusoidal form due to the shape of the stent, composed of five repeated units and that the farther from the middle of the geometry the ring analyzed is, the lower the strain is. Graph 25 shows the strain at different steps of the simulation to understand strain increase during stent expansion.

Rings of uninterest (ring1, ring2 and ring3) have a lower strain than the others because their positions do not correspond to the stent position. This demonstrates that not the whole vessel is affected by high strain after stent implantation. The 3D plot shows how the strain is distributed in the axial direction at the end of the expansion.

Another interesting test considers the symmetry of the strain with respect to the middle of the vessel as a symmetric distribution justifies the analysis of only half the geometry. The plots reported in Graph 27 shows that the results are not perfectly symmetric but the differences are rather small with magnitude of order 0.005. Only the comparison between ring 1 and ring 9 highlights a higher error approaching 0.01. This could be due to the fact that the extreme parts of the stent have slightly different geometry, as presented with red circles in the Figure 12.

3.4 Reconstruction and image registration

The stented vessel configuration was analysed to address the experimental problem of the photogrammetry accuracy and the strain field measurement. This test is related to the experimental reality and the vessel was modelled as an hyperelastic cylinder in which a stent was expanded by a fixed displacement to simulate the clinical conditions.

As shown in Figure 56, the evaluation of the strain distribution was conducted only on a small part of the stented vessel since this was considered to be sufficient to study the photogrammetric method reliability.

3.4.1 Graphical strain distribution

The strain distribution shown in Figure 57 illustrates the circumferential strain on the stented vessel examined respectively with the reconstruction and the image registration methods. The minimum and the maximum value reached are 0.0153 and 0.2145. The image that reports the Green strain distribution data (b) shows that this formula is subject to noise along all the geometry while using the Local strain approach (c) this disturbance is

becomes more smoothed, although in some areas some peaks are detected where actually they are not present in the ANSYS results. The value of strain calculated with the two formula are in generally good agreement with the expected values given by ANSYS.

The comparison between the reconstruction and image registration on the circumferential strain shows that image registration results in lower noise on the measurement in fact the plots look smoothed and the values better approximate the ANSYS results, maintaining the issue previously illustrated.

Figure 58 reports the distribution of the axial strain extracted by position data acquired with two different methods. The value of the strain is included between -0.1086 and 0.0891. As already highlighted from the previous results the Green (b) and the Local (c) strain are affected by noise, although the Local strain measurement gives a most precise strain distribution. As with previously reported results, data acquired with the image registration technique shows a lesser contribution of noise to the strain values calculated. These outcomes are due to improved accuracy of this semi-automatic acquisition method.

3.4.2 Error plots

Graph 28 and Graph 29 report the absolute error on strain expressed as the mean value plus the standard deviation calculated on the whole population of errors. As for the other geometries every figure contains three plots which show the comparison between strains computed from different approaches.

The absolute error on circumferential strain is maximum in the first comparison. The calculation methods used present a large scattering (mean plus standard deviation) in all the cases, especially in the first and second comparisons. Both of the measurement approaches are positively influenced by the image registration technique in fact the maximum Green strain scattering error in this direction is 0.0222 for the manual reconstruction and it becomes 0.0180 in the image registration case while the Local strain improves from a value of 0.0212 to 0.0175.

The second comparison shows that the mean values tend to zero: this means that the error due to the technique inaccuracy is low. In particular, the mean Green strain result is 0.0002 for the manual method and 0.0000 using the image registration. This highlights, as before an improvement thanks to the semi-automatic technique. Though the standard deviation is

higher in the second comparison, this is related to the random noise introduced by the experimental approach.

In circumferential direction the mean error mostly arises from the assumptions in the strain post-processing as shown by the third comparison. The maximum scattering (mean plus standard deviation) error introduced is 0.0149 with Green strain approach because of the presence of a large shear strain in this kind of application, due to the deformation of the cylindrical surface by the stent metal bar.

The same conclusions can be drawn from the plot in Graph 29, as regards the axial direction. The difference in this case is that data calculated with the Green strain formula present lower mean errors than those extracted using the Local strain formulation, 0.0040 and 0.0054 respectively, whilst the maximum scattering reached is higher with the Green strain (0.0218). Image registration again results in improvement in the strain measurement and the error is principally due to assumptions in the post-processing. The maximum mean error due to acquisition technique is in fact 0.0003.

Conclusions

The Strip geometry was implemented and tested to have a measure of the error on a simple 2D configuration. In all the tests the same displacement was imposed to the lower edge of the specimen while the upper edge was fixed and could not move; the difference between the tests was the material property, in fact in the first two cases a linear elastic material was modelled and in the third trial a hyperelastic constitutive law was applied. The aim of changing material properties was to understand how the system reacts to changes in the specimen. Finally a zero strain test was performed to quantify the influence of the reconstruction error.

From the ANSYS strain distributions of the stented vessel geometry shown in the previous chapters (Figure 57 and Figure 58) it is possible to extract two thresholds for the minimum strain resolution which is required to be measured in the actual application. In fact the aim of the photogrammetry is to detect the full-field strain on an object's surface and the resolution of the method is the minimum strain variation that the system can detect. If the accuracy error is higher than the required resolution than the system is not suitable for the application.

In the actual case the resolution required in the transversal and longitudinal direction is 0.01 strain, in fact to distinguish between the central area and the borders of the distribution a resolution of at least 0.01 is necessary.

The manual reconstruction method provides a maximum error, calculated as the mean error plus the standard deviation, of 0.0087 in the transversal direction and 0.0062 in the

longitudinal therefore the results suggest a good agreement with the strip application. However, it is acknowledged that the noise in the central region is still high and it is not possible to discriminate between the strain peak and its surrounding.

An improvement to this problem is provided by the image reconstruction where the maximum errors are 0.0063 in the transversal and 0.0033 in the longitudinal direction. The image registration is more accurate and it is able to determine the variation of the strain distribution with reduction in noise, although the transversal direction is still problematic.

This magnitude of error is related to the Green and Local strain measures but for the Global strain the errors decrease to 0.0028 in the transversal and 0.0019 in the longitudinal direction for the manual reconstruction, with a further improvement for the image registration. The application of this approach would significantly decrease the error on the strain measurement because of its smoothing action. In this work was not applied because of the curvature of the Vessel and transforming the nodal coordinates from a Cartesian to a Cylindrical reference system present a difficulty due to the mismatching of them caused by the calibration procedure.

The zero strain test reports an error of 0.0060 on the transversal and 0.0062 on the longitudinal strain for the manual reconstruction; the use of image registration reduces these errors to 0.0009 in the transversal and 0.0013 in the longitudinal direction. These errors represent the noise introduced by the acquisition method and depend strictly on the ability of the operator to pick points and the image registration to track point displacements. The zero strain error is comparable in both directions and this means that the picking process does not have a critical direction. A comparison between these errors and those observed in the stretched strip shows that in the longitudinal direction the error is similar while in the transversal direction a large component is added. This increase in error in the transversal strain is due to the level of deformation, in fact when the deformations are low the displacement is comparable with the reconstruction error and the effect on the final strain is more significant. On the contrary when the deformation becomes greater the reconstruction error has a lower influence on the strain measurement because the displacements are higher.

The comparison between different materials indicates that when the strain distribution on the geometry is more uniform, like in the hyperelastic case, the technique struggles more to discriminate the different regions because the level of deformation is lower. This can be

seen in the mean value of error which is generally higher. Nevertheless the standard deviation is comparable to the deviation of the linear elastic material and this signals that the effect of noise on the measurement is the same.

The photogrammetry technique has been evaluated for a simple geometry application and the associated error is less than 0.01, therefore the system is suitable for *in-vitro* experiments on linear elastic and hyperelastic materials where this strain resolution is acceptable. Furthermore the virtual system provided a flexible instrument to test several aspects of the system, like the resolution of the images and the interpolated strain measurement.

The Vessel model was developed to study how well the system was able to reconstruct a 3D geometry with curvature to move closer to the experimental configuration of interest. Two materials were used for the cylindrical model and each of them was tested with two separate load conditions: in the first case the vessel was expanded under a pressure at 120 mmHg and in the second case the internal surface was displaced by 0.5 mm.

The ANSYS strain distributions in Figure 48 and Figure 49 show that the circumferential and axial strain is uniform, hence there are no variations of strain which need to be detected by the optical method and the ideal error would be null. Since the system is not perfect and noise is introduced a threshold of 0.01 for the strain error is considered in both direction.

The manual reconstruction is afflicted by a maximum error of 0.0133 in the circumferential and 0.0064 in the axial direction, calculated as the mean value plus the standard deviation. The noise introduced has a random distribution, characterised by local maxima and minima.

The image registration reports a lower error than the other technique: it is equal to 0.0088 on the circumferential strain and 0.0019 on the axial value. The distribution of the strain in the axial direction looks completely casual while the strain plot in the hoop direction (Figure 50) appears with some vertical strips along the geometry which correspond to higher or lower values with respect to the expected strain. These lines could indicate the presence of an error due to the geometry of the vessel, in particular to the curvature.

An observation which underlines the possibility of a geometric issue is the fact that contrary to the results for the strip in the vessel the error on the circumferential strain increases with the level of deformation. The difference between the tests is the material

and the loading and this results in a progressive increase of the expected deformation; correspondingly the mean error increases. This trend is probably due to the shape of the object, in fact the error is mainly due to the calculation method as shown in the *Discussion* section and wherever the cylinder is more expanded the effect of the curvature becomes more significant. The standard deviation of the error decreases when the image registration is used, as observed with the strip.

On the contrary the axial direction is not affected by error due to the post-processing calculations and the associated error for the image registration is comparable to the one extracted for longitudinal strain in the strip geometry. Also the change in the material properties and the different loading do not influence the resulting error and the mean value is low.

The photogrammetry technique applied on the simple vessel has given conflicting results, in fact the accuracy error is higher than 0.01 in the circumferential direction when the points are acquired with the manual reconstruction while all the other values are under the critical threshold and the measurements are accurate enough. Therefore the use of the image registration as a technique to reduce the noise introduced by the manual picking operation is highly recommended to improve strain calculation on the cylindrical surface.

The Stented vessel configuration was implemented and expanded to study the system's robustness in a 3D test which reproduces an experimental condition. An hyperelastic constitutive law was used to simulate the vessel and the stent was expanded by a displacement applied on a rigid surface (balloon). The strains were later calculated with the same post-processing applied for the vessel geometry.

Figure 57 and Figure 58 inform the definition of a threshold of acceptability that allows the reconstruction technique to capture the variation in strain in the vessel wall. The threshold is fixed at 0.02 in the axial direction and 0.03 in the circumferential direction. In this way it is possible to determine the sinusoidal trend of the hoop strain plots against the theta coordinate.

The maximum error between strains extracted from the nodal positions manually reconstructed is 0.0218 in the axial direction and 0.0222 in the circumferential. Using this reconstruction method it is possible to determine strain variations in the circumferential direction within the defined threshold. In the axial direction the trend detected is not too far

from the gold standard data given by ANSYS, as the error only slightly exceeds the defined threshold.

The errors calculated from the results obtained with the nodal coordinates given by image registration technique are both below the defined thresholds. In particular, the error on axial strain is 0.0186 and on circumferential strain the error is 0.0180. As already highlighted in the trials for the other geometries, image registration technique is hence more accurate.

From the second comparison it is visible that the error mostly belongs to the calculation formula used to obtain the hoop strain: in both cases (Green and Local strain), it does not approximate perfectly the values because of the bending of the cylindrical structure and consequently the hoop displacement becomes significant as much as the radial one.

The error on strain of the photogrammetric system has been shown to be under 1% in the 2D geometries and below 3% in the 3D configurations. Therefore the technique is accurate enough to be employed in *in-vitro* experiments regarding the full-field strain measurement on stented vessel surfaces where these thresholds are appropriate.

The optical methods are considered to be a reliable and not invasive technique for the strain measurement and can be employed in many applications. In particular the advantage of using these methods is that they do not directly interact with the object of interest and therefore they do not influence the strain measurement. In case of soft tissues, where even the minimal interaction could potentially change the response of the specimen, this feature is greatly appreciated. Therefore the stereo-photogrammetry has a large field of applications like the *in-vitro* experimentation about the effects of stenting on the vascular wall's deformations or in general the study of large deformation phenomena. Both the academic and industrial research could benefit from the use of these methods. These techniques are still not used in the clinical practice since they require to see the interested part and the surgical operations do not provide the right environment for their employment. The material properties which were varied in the different tests to understand the influence on the strain measurement do not affect significantly the error value. In particular, the mean error is altered by the level of deformation and this latter depends on the constitutive law but it is not the material property itself which influences the measurement. In fact the

standard deviation error remains unchanged among the materials and this shows that it is only an error due to the acquisition technique.

In all the configurations the Green and Local strain measure introduce an error when compared with the ANSYS reported values. This observation suggests that the calculation method is important and the assumptions made to obtain the strains can influence the final measure. As it is possible to see in the strip analysis the Global strain approach can reduce the amount of error on the measure, thanks to the smoothing action performed on the reconstruction error of the single nodes. The image registration technique has been successful in all the trials and it has always improved the accuracy compared to the manual reconstruction system.

The evaluation process shown in the present work has been proved to be a reliable and effective method to predict the accuracy of an optical system in advance. The *in-vitro* experiments require high efforts in terms of funds and equipment and a virtual platform on which preliminary tests of accuracy can be performed is a powerful instrument to save time and funds. In fact stereoscopic strain measurement shows potential as a method for characterising the behaviour of biological materials but its application to small vessels demands high accuracy, and the possibility of testing this feature in advance on an experimental trial is a remarkable potentiality. Also the virtual environment provides a simple and flexible platform on which explore the influence of every single set-up parameters on the final strain measurement. In fact this evaluation process allows to maintain all the aspects of the camera rig consistent and vary only one parameter at a time, then the results can be studied to quantify the effects of this single variation, like it has been done for some system's details during this work. Doing these with a physical system would cost a lot on terms of instrumentation and support, while with the virtual process these investigations can be easily performed.

Potential error sources

The present study has underlined the limitations of the stereoscopic strain measurement thanks to a virtual evaluation process. In particular, during the process several potential sources of error on strain have been detected (Figure 59):

- the complexity of the geometry is linked to the dimensions of the specimen. The 2D configuration (strip) presents a lower error than the 3D geometries (vessel and stent) and their orientation in space influences measurement of the nodal data. Both the object shape and its orientation with respect to the cameras affects the way the surface is viewed and therefore the impact of the perspective. The planar object facing the cameras shows less perspective projection than the vessel, and reference points are easier to detect;
- the resolution of the images affects the number of pixels for every millimeter of the geometry. Hence if the resolution is low an error of few pixels can result in a large error in terms of millimeters, and viceversa a high resolution allows to discriminate smaller features. The strip analysis illustrated this issue;
- the calibration parameters express the intrinsic and extrinsic parameters of the camera set-up. If these parameters are affected by an error they can disturb the reconstruction of the geometry surface, for example if the translation and rotation matrix is not perfectly determined the position measurement can introduce an error which is propagated to the strain measurement. Similar effects can occur if the distortion is poorly estimated and a fictitious strain can be generated;
- the acquisition method is one of the most influential sources of error. In fact if the nodal positions are not well determined the strain measurement is affected by a large error. The acquisition techniques studied in the present work included manual reconstruction and image registration, both introduce some problems. In the manual reconstruction the operator manually picks the points on the object surface and during this phase the error on the position can be great. Whilst image registration reduces the error on the position, the initial grid which is provided to the system comes from a manual process and initial errors in grid position will not provide accurate values of 3d position;
- to extract the strains from the position data different calculation methods can be applied. Each formulation is associated with assumptions made to make the

formula suitable for the application. These approximations can overestimate or underestimate the real strain value, like in the Green and Local strain measurement case. Furthermore it is possible to select a calculation method able to smooth the position error related to the single points as shown with the Global strain measurement.

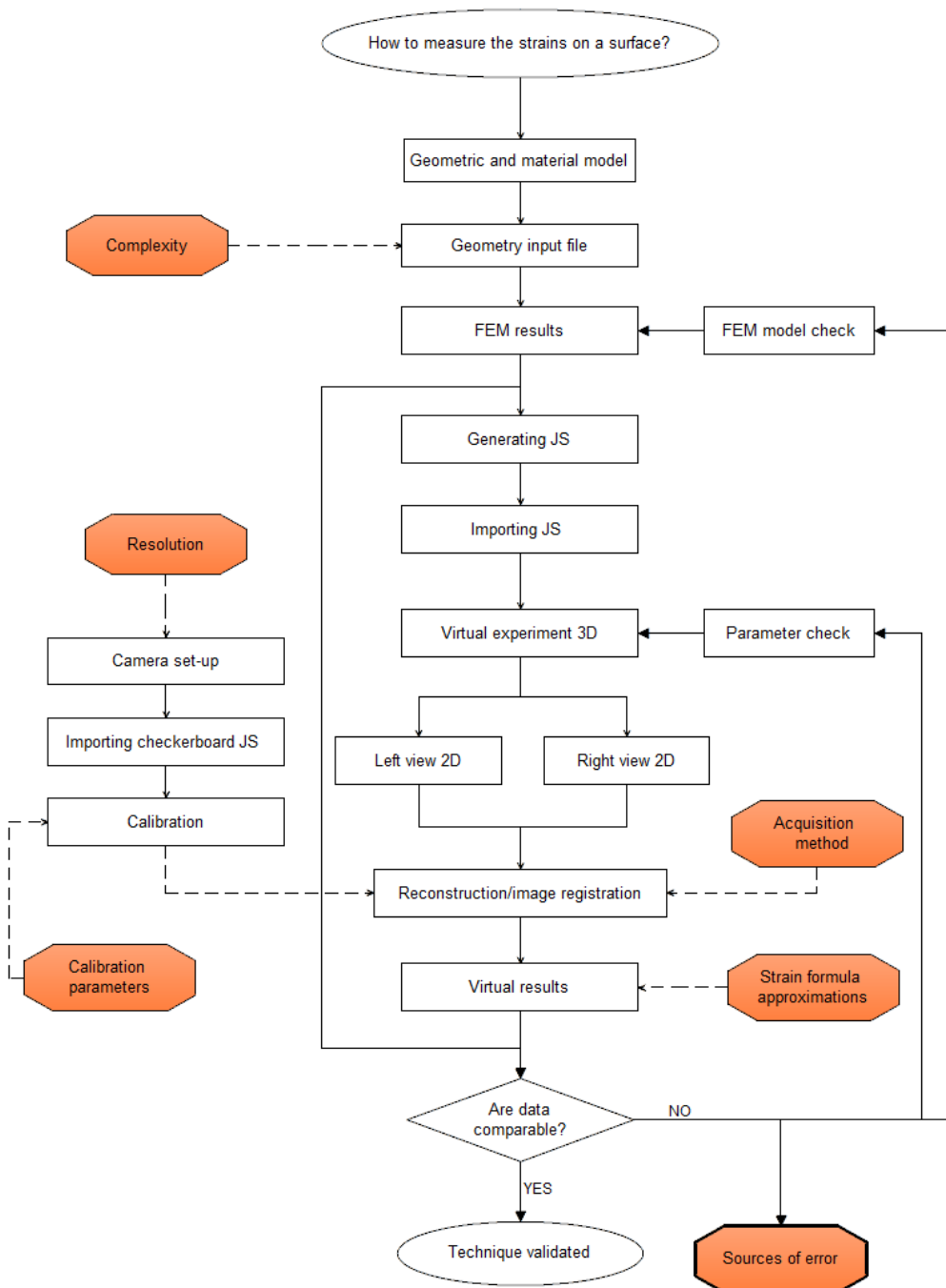


Figure 59 Potential sources of error flowchart

Future work

The present work has explored the characteristics of a stereo-photogrammetric method and it has developed a virtual platform for the estimation of the accuracy error. The results for the 2D geometry are satisfying and the error extracted on the 3D configurations are encouraging. In particular, this system can be used for *in-vitro* experiments on stent expansion within a synthetic or biological vessel or for every other application which requires the use of an optical system to detect the full-field strain of a surface.

Although the results obtained with the present system are promising some improvements can be introduced to reduce the strain error and improve the measurement accuracy. The tests on the reconstruction and image registration have highlighted the effectiveness of the image registration compared to manual picking of points of interest. Image registration is a complex technique which includes parameters associated with the image registration algorithm. An interesting study could be conducted on how such parameters affect the strain measurement and its error. Variation of registration parameters and comparison of the resulting strain with ANSYS data would allow evaluation of the dependency of the final values on system features. Appropriate parameters for testing include the smoothing parameter, the node spacing and the number of steps of deformation.

The Global strain measurement has demonstrated good accuracy and reduced error in all directions of interest. This calculation method has not been applied to the cylindrical

geometry due to some technical issues related mainly to the calibration parameters and the coordinate system. A post-processing method could be developed to obtain an interpolated strain measurement on the curved surface and smooth in this way the errors related to the current local measurements.

The system was evaluated in a static condition, in fact the object was captured in the initial and final steps of deformation and the strains were calculated only at the maximum expansion. The tests also demonstrated that at large deformations the system performed better measurements than at smaller deformations. A development of this work could include evaluation of the photogrammetric system under dynamic conditions, to report geometries which undergo sequential steps of deformation. An interesting application would be the study of a stented vessel subjected to a pulsatile flow: this system would replicate the realistic condition of a vessel after the stenting operation and with physiological boundary conditions. This test could be useful to quantify the accuracy error in a dynamic situation and if the system is able to follow cyclic deformations of small magnitude.

The material models used were taken from previous studies or from literature papers whose aim was to recreate a realistic vessel. The aim of this project was not to develop a realistic coronary artery model but to focus on the virtual platform and the evaluation of the photogrammetric system, so that the constitutive law did not represent the main issue. To address the problem of a realistic simulation and better approximate the experimental reality a more complex material model could be introduced. For example an anisotropic material with fibers to simulate the vessel tissue could be implemented and tested with the evaluation process. This would help to approach the *in-vitro* experiments in which porcine arteries are employed and give a more accurate error evaluation.

Finally, the virtual system could be evaluated in a parallel test with an experimental system. The virtual process provides an effective and flexible instrument to estimate the accuracy of an optical system but the simplifications made by the virtual platforms (ANSYS, Realsoft) can divert the result from the real behaviour. A parallel study with a real system could provide a measure of how close the error given by the virtual evaluation process is to experimental observations. A camera set-up could be set-up in an experimental rig and the same configuration could be implemented in Realsoft, then the

object would be imported in ANSYS and a simulation reproducing the experiment would be run. All reconstruction and post-processing would be applied on both virtual and *in-vitro* tests and the results of the two parallel trials would be compared to determine if the error given by the evaluation is effectively representing the real system.

Appendix A

1. Error values

The absolute deviation between two values of strain derived with different post-processings (e.g. ε_A and ε_B) is calculated with the relationship shown below:

$$\Delta\varepsilon_i = \varepsilon_{A_i} - \varepsilon_{B_i}$$

The index i indicates that the obtained deviation refers to the comparison between two correspondent measurements within a strain data set.

The maximum, mean and standard deviation on the whole delta population is then computed using the following formulas:

$$\Delta\varepsilon_{max} = \max(|\Delta\varepsilon_i|)$$

$$\Delta\varepsilon_{mean} = \frac{1}{n} \sum_{i=1}^n \Delta\varepsilon_i$$

$$\Delta\varepsilon_{std} = \sqrt{\frac{1}{n} \sum_{i=1}^n (\Delta\varepsilon_i - \Delta\varepsilon_{mean})^2}$$

The percentage deviation between two values of strain derived with different methods (e.g. ε_A and ε_B) is calculated with the following relationship, which performed a normalisation of the error on the expected value:

$$\Delta\varepsilon_{i\%} = 100 \frac{(\varepsilon_{A_i} - \varepsilon_{B_i})}{\varepsilon_{B_i}}$$

Finally the percentage maximum value, the mean and the standard deviation on the whole population is subsequently obtained with the formulas below:

$$\Delta\varepsilon_{max\%} = \max(|\Delta\varepsilon_{i\%}|)$$

$$\Delta\varepsilon_{mean\%} = \frac{1}{n} \sum_{i=1}^n \Delta\varepsilon_{i\%}$$

$$\Delta\varepsilon_{std\%} = \sqrt{\frac{1}{n} \sum_{i=1}^n (\Delta\varepsilon_{i\%} - \Delta\varepsilon_{mean\%})^2}$$

Appendix B

1. Noise test

In the tables below the comparison between the derived strains and the ANSYS values is summarised for each one of the five random noise tests. The noised strains were calculated from the noised positions using both the Local and the Green strain methods and the error is here reported as a percentage value. Table 31 refers to the data of the strip at middle step of deformation, while Table 32 is related to the end of the tensile test.

Table 31 Percentage error on strain at middle step of deformation for noise test

Middle step		Transversal		Longitudinal	
		Green	Local	Green	Local
1	Max	101.12	100.60	64.60	63.57
	Mean	38.40	40.78	26.05	25.46
	Std	30.96	30.05	20.40	19.25
2	Max	151.28	147.27	63.72	61.33
	Mean	58.31	66.81	29.82	27.43
	Std	45.20	48.94	16.98	16.61
3	Max	119.06	112.21	69.28	67.83
	Mean	47.22	45.20	24.52	25.26
	Std	41.34	41.28	18.53	20.57
4	Max	133.18	129.30	74.17	74.32
	Mean	61.01	55.91	31.04	31.40
	Std	45.53	42.25	16.31	19.16
5	Max	154.25	154.32	58.03	59.39
	Mean	57.41	64.05	26.75	26.49
	Std	31.12	34.97	18.73	18.25

Table 32 Percentage error on strain at final step of deformation for noise test

Final step		Transversal		Longitudinal	
		Green	Local	Green	Local
1	Max	83.48	85.14	22.88	22.77
	Mean	46.45	46.96	9.58	9.96
	Std	33.64	33.80	7.72	8.53
2	Max	96.14	93.12	29.60	29.60
	Mean	52.71	44.44	12.37	12.69
	Std	34.83	34.48	8.56	8.71
3	Max	82.41	83.11	23.34	23.11
	Mean	45.07	41.63	10.09	8.26
	Std	27.57	28.70	7.27	7.08
4	Max	71.94	77.15	29.16	28.46
	Mean	41.21	44.45	13.02	12.77
	Std	21.18	22.58	9.01	9.77
5	Max	84.91	84.81	32.79	33.82
	Mean	24.75	24.14	12.50	12.16
	Std	27.18	28.25	10.68	10.75

The same data described above were compared and expressed as absolute error. Table 33 below refers to the data on the strip in the middle step of the simulation, while Table 34 is related to the final instant of the tensile test.

Table 33 Absolute error on strain at middle step of deformation for noise test

Middle step		Transversal		Longitudinal	
		Green	Local	Green	Local
1	Max	0.051	0.051	0.064	0.063
	Mean	0.019	0.020	0.023	0.025
	Std	0.016	0.015	0.020	0.019
2	Max	0.076	0.074	0.063	0.061
	Mean	0.029	0.034	0.030	0.027
	Std	0.023	0.025	0.017	0.017
3	Max	0.060	0.056	0.069	0.067
	Mean	0.024	0.023	0.024	0.025
	Std	0.021	0.021	0.018	0.020
4	Max	0.067	0.065	0.074	0.034
	Mean	0.031	0.028	0.031	0.031
	Std	0.023	0.021	0.016	0.019
5	Max	0.077	0.078	0.058	0.059
	Mean	0.029	0.031	0.027	0.026
	Std	0.016	0.018	0.019	0.018

Table 34 Absolute error on strain at final step of deformation for noise test

Final step		Transversal		Longitudinal	
		Green	Local	Green	Local
1	Max	0.080	0.081	0.043	0.043
	Mean	0.044	0.045	0.018	0.020
	Std	0.032	0.032	0.015	0.016
2	Max	0.092	0.090	0.056	0.056
	Mean	0.050	0.042	0.024	0.024
	Std	0.033	0.033	0.016	0.017
3	Max	0.079	0.080	0.044	0.044
	Mean	0.043	0.040	0.019	0.016
	Std	0.026	0.027	0.014	0.013
4	Max	0.069	0.074	0.055	0.054
	Mean	0.039	0.042	0.025	0.024
	Std	0.020	0.022	0.017	0.019
5	Max	0.081	0.081	0.062	0.064
	Mean	0.024	0.023	0.024	0.023
	Std	0.026	0.027	0.020	0.020

2. Resolution test

Table 35 reports the absolute values of maximum, mean and standard deviation error on strain for the resolution test at different steps of deformation (middle and final). The strains were derived using the Local strain measurement and the obtained values were compared with the ANSYS data to calculate the error.

Table 35 Absolute error on strain for resolution test

	Pixels	Transversal		Longitudinal	
		Middle	Final	Middle	Final
Max	1020	0.0173	0.0172	0.0176	0.0102
	1200	0.0170	0.0196	0.0185	0.0134
	2400	0.0062	0.0081	0.0066	0.0025
Mean	1020	-0.0022	-0.0030	-0.0023	-0.0008
	1200	-0.0028	-0.0040	-0.0004	-0.0007
	2400	-0.0016	-0.0007	0.0001	-0.0002
Std	1020	0.0077	0.0073	0.0074	0.0061
	1200	0.0081	0.0085	0.0112	0.0081
	2400	0.0028	0.0034	0.0031	0.0014
Mean + std	1020	0.0099	0.0103	0.0097	0.0069
	1200	0.0109	0.0124	0.0116	0.0088
	2400	0.0044	0.0041	0.0032	0.0016

Table 36 reports the same comparison reported above but with the error expressed as a percentage value of the expected strain.

	Pixels	Transversal		Longitudinal	
		Middle	Final	Middle	Final
Max	1020	25.58	15.28	21.58	5.68
	1200	25.37	17.02	15.74	6.64
	2400	11.09	7.81	7.06	1.32
Mean	1020	2.35	2.57	-2.91	-0.52
	1200	3.31	3.39	-1.56	-0.55
	2400	2.85	0.63	-0.02	-0.11
Std	1020	14.25	7.50	8.37	3.24
	1200	14.05	7.77	11.00	4.31
	2400	5.25	3.44	3.15	0.73

3. Global strain

Table 37 reports the absolute values of maximum, mean and standard deviation error derived from the comparison between the ANSYS data and the strains calculated with the Global strain approach. The longitudinal strain calculated with the four methods focuses on two vertical lines of the Strip geometry at middle and final step of deformation.

Step	Line	Method	Max	Mean	Std	Mean +std
Middle	1	1	0.0068	-0.0002	0.0031	0.0033
		2	0.0068	-0.0001	0.0032	0.0033
		3	0.0031	-0.0004	0.0013	0.0017
		4	0.0014	0.0000	0.0011	0.0011
	2	1	0.0070	-0.0005	0.0029	0.0034
		2	0.0062	-0.0006	0.0027	0.0033
		3	0.0035	-0.0002	0.0014	0.0016
		4	0.0012	-0.0004	0.0009	0.0013
Final	1	1	0.0055	-0.0003	0.0031	0.0035
		2	0.0054	-0.0002	0.0031	0.0033
		3	0.0038	-0.0007	0.0016	0.0023
		4	0.0012	-0.0007	0.0007	0.0014
	2	1	0.0047	-0.0004	0.0027	0.0031
		2	0.0047	-0.0004	0.0029	0.0034
		3	0.0028	-0.0001	0.0017	0.0018
		4	0.0028	-0.0006	0.0020	0.0026

Table 38 shows the same values reported in the previous table but expressed as a percentage of the expected data.

Table 38 Percentage error on longitudinal strain for the Global strain test

Step	Line	Method	Max	Mean	Std
Middle	1	1	6.98	-0.23	3.12
		2	6.98	-0.12	3.20
		3	3.14	-0.36	1.31
		4	1.43	-0.03	1.07
	2	1	7.13	-0.45	2.98
		2	6.27	-0.61	2.74
		3	3.54	-0.19	1.43
		4	1.23	-0.40	0.92
Final	1	1	3.30	-0.19	1.69
		2	2.80	-0.12	1.64
		3	2.13	-0.38	0.85
		4	0.66	-0.36	0.36
	2	1	2.53	-0.23	1.47
		2	2.53	-0.22	1.59
		3	1.51	-0.06	0.90
		4	1.51	-0.31	1.09

4. Reconstruction and image registration

The following tables summarise the results of the analysis on the Strip geometry conducted with the manual reconstruction and image registration technique. Four analyses were undertaken as listed in Table 39.

Table 39 Summary of the tests conducted on the Strip geometry

Test	Geometry	Material	Simulation	Calibration	Element
1	A (Strip)	1 Goude	b (tensile)	14	Plane42
2	A (Strip)	2 Chua	b (tensile)	14	Plane42
3	A (Strip)	3 Wu	b (tensile)	14	Plane182
4	A (Strip)	1	a (zero strain)	14	Plane42

As reported in the *Results* section, strains deriving from different sources were compared to determine the origins of the error on the strain measure. In the following tables the specific comparisons are marked with numbers. In particular, the references are:

- 1) ANSYS derived vs. ANSYS reported data;
- 2) ANSYS reported vs. test data;
- 3) ANSYS derived vs. test data.

Table 40 and Table 41 report the absolute values of maximum, mean, standard deviation and scattering error on the transversal and longitudinal strain for test 1. In the same way Table 42 and Table 43 refer to test 2, Table 44 and Table 45 illustrate the results for test 3 and finally Table 46 and Table 47 are related to the test 4. The scattering is calculated as the sum of mean and standard deviation error on the measurement.

Table 40 Absolute error on transversal strain for test 1

		Transversal					
		Reconstruction			Image registration		
		Green	Local	Global	Green	Local	Global
1	Max	0.0162	0.0085	0.0022	0.0162	0.0085	0.0022
	Mean	0.0001	0.0002	-0.0002	0.0001	0.0002	-0.0002
	Std	0.0035	0.0013	0.0007	0.0035	0.0013	0.0007
	Mean + std	0.0037	0.0015	0.0010	0.0037	0.0015	0.0010
2	Max	0.0205	0.0186	0.0063	0.0198	0.0115	0.0033
	Mean	-0.0006	-0.0006	-0.0008	0.0003	0.0004	-0.0003
	Std	0.0081	0.0074	0.0017	0.0053	0.0040	0.0010
	Mean + std	0.0087	0.0080	0.0025	0.0056	0.0044	0.0013
3	Max	0.0188	0.0187	0.0053	0.0080	0.0082	0.0022
	Mean	-0.0008	-0.0008	-0.0006	0.0002	0.0002	-0.0001
	Std	0.0073	0.0073	0.0016	0.0037	0.0037	0.0008
	Mean + std	0.0081	0.0081	0.0022	0.0039	0.0039	0.0008

Table 41 Absolute error on longitudinal strain for test 1

		Longitudinal					
		Reconstruction			Image registration		
		Green	Local	Global	Green	Local	Global
1	Max	0.0154	0.0036	0.0038	0.0154	0.0036	0.0038
	Mean	0.0003	0.0000	-0.0005	0.0003	0.0000	-0.0005
	Std	0.0020	0.0007	0.0010	0.0020	0.0007	0.0010
	Mean + std	0.0023	0.0007	0.0016	0.0023	0.0007	0.0016
2	Max	0.0261	0.0152	0.0053	0.0139	0.0054	0.0037
	Mean	0.0003	0.0001	-0.0005	0.0004	0.0001	-0.0004
	Std	0.0057	0.0054	0.0014	0.0026	0.0018	0.0012
	Mean + std	0.0060	0.0054	0.0019	0.0029	0.0019	0.0016
3	Max	0.0147	0.0147	0.0035	0.0044	0.0054	0.0020
	Mean	0.0000	0.0001	0.0001	0.0001	0.0001	0.0001
	Std	0.0052	0.0053	0.0011	0.0019	0.0019	0.0008
	Mean + std	0.0053	0.0053	0.0012	0.0020	0.0020	0.0009

Table 42 Absolute error on transversal strain for test 2

		Transversal					
		Reconstruction			Image registration		
		Green	Local	Global	Green	Local	Global
1	Max	0.0159	0.0083	0.0022	0.0159	0.0083	0.0022
	Mean	0.0001	0.0002	-0.0002	0.0001	0.0002	-0.0002
	Std	0.0035	0.0013	0.0007	0.0035	0.0013	0.0007
	Mean + std	0.0036	0.0015	0.0010	0.0036	0.0015	0.0010
2	Max	0.0289	0.0206	0.0051	0.0196	0.0119	0.0031
	Mean	-0.0002	-0.0002	-0.0003	0.0003	0.0004	-0.0002
	Std	0.0075	0.0068	0.0016	0.0060	0.0050	0.0010
	Mean + std	0.0077	0.0070	0.0020	0.0063	0.0054	0.0012
3	Max	0.0203	0.0203	0.0039	0.0092	0.0093	0.0021
	Mean	-0.0003	-0.0004	-0.0001	0.0002	0.0002	0.0001
	Std	0.0067	0.0067	0.0014	0.0047	0.0047	0.0008
	Mean + std	0.0070	0.0071	0.0015	0.0049	0.0049	0.0009

Table 43 Absolute error on longitudinal strain for test 2

		Longitudinal					
		Reconstruction			Image registration		
		Green	Local	Global	Green	Local	Global
1	Max	0.0151	0.0035	0.0037	0.0151	0.0035	0.0037
	Mean	0.0003	0.0000	-0.0005	0.0003	0.0000	-0.0005
	Std	0.0020	0.0007	0.0010	0.0020	0.0007	0.0010
	Mean + std	0.0022	0.0007	0.0015	0.0022	0.0007	0.0015
2	Max	0.0260	0.0176	0.0044	0.0136	0.0050	0.0035
	Mean	0.0003	0.0001	-0.0005	0.0004	0.0001	-0.0004
	Std	0.0056	0.0052	0.0014	0.0025	0.0018	0.0011
	Mean + std	0.0059	0.0053	0.0019	0.0029	0.0019	0.0016
3	Max	0.0190	0.0185	0.0034	0.0041	0.0051	0.0019
	Mean	0.0000	0.0000	0.0000	0.0001	0.0001	0.0001
	Std	0.0052	0.0051	0.0011	0.0018	0.0018	0.0008
	Mean + std	0.0052	0.0052	0.0011	0.0019	0.0019	0.0009

Table 44 Absolute error on transversal strain for test 3

		Transversal					
		Reconstruction			Image registration		
		Green	Local	Global	Green	Local	GlobalS
1	Max	0.0106	0.0055	0.0042	0.0106	0.0055	0.0042
	Mean	-0.0003	-0.0004	-0.0007	-0.0003	-0.0004	-0.0007
	Std	0.0033	0.0008	0.0011	0.0033	0.0008	0.0011
	Mean + std	0.0037	0.0012	0.0018	0.0037	0.0012	0.0018
2	Max	0.0252	0.0194	0.0054	0.0140	0.0099	0.0037
	Mean	-0.0010	-0.0011	-0.0010	-0.0002	-0.0003	-0.0006
	Std	0.0076	0.0071	0.0018	0.0059	0.0048	0.0010
	Mean + std	0.0087	0.0082	0.0028	0.0062	0.0050	0.0017
3	Max	0.0194	0.0195	0.0038	0.0083	0.0096	0.0022
	Mean	-0.0007	-0.0008	-0.0004	0.0001	0.0001	0.0000
	Std	0.0070	0.0071	0.0014	0.0047	0.0047	0.0008
	Mean + std	0.0077	0.0079	0.0017	0.0048	0.0048	0.0008

Table 45 Absolute error on longitudinal strain for test 3

		Longitudinal					
		Reconstruction			Image registration		
		Green	Local	Global	Green	Local	Global
1	Max	0.0186	0.0091	0.0022	0.0186	0.0091	0.0022
	Mean	0.0006	0.0004	-0.0002	0.0006	0.0004	-0.0002
	Std	0.0019	0.0013	0.0006	0.0019	0.0013	0.0006
	Mean + std	0.0025	0.0017	0.0008	0.0025	0.0017	0.0008
2	Max	0.0244	0.0174	0.0043	0.0200	0.0101	0.0024
	Mean	0.0008	0.0006	-0.0002	0.0007	0.0005	-0.0002
	Std	0.0054	0.0052	0.0012	0.0026	0.0020	0.0009
	Mean + std	0.0062	0.0058	0.0014	0.0033	0.0026	0.0011
3	Max	0.0171	0.0170	0.0041	0.0046	0.0048	0.0021
	Mean	0.0002	0.0002	0.0001	0.0001	0.0001	0.0001
	Std	0.0050	0.0050	0.0012	0.0017	0.0017	0.0008
	Mean + std	0.0052	0.0052	0.0013	0.0018	0.0018	0.0008

Table 46 Absolute error on transversal strain for test 4

		Transversal					
		Reconstruction			Image registration		
		Green	Local	Global	Green	Local	Global
1	Max	0.0000	0.0000	0.0000	0.0000	0.0000	0.0000
	Mean	0.0000	0.0000	0.0000	0.0000	0.0000	0.0000
	Std	0.0000	0.0000	0.0000	0.0000	0.0000	0.0000
	Mean + std	0.0000	0.0000	0.0000	0.0000	0.0000	0.0000
2	Max	0.0147	0.0147	0.0033	0.0017	0.0027	0.0006
	Mean	-0.0001	-0.0002	-0.0001	0.0000	0.0000	-0.0001
	Std	0.0059	0.0058	0.0013	0.0009	0.0009	0.0003
	Mean + std	0.0060	0.0060	0.0014	0.0009	0.0009	0.0004
3	Max	0.0147	0.0147	0.0033	0.0017	0.0027	0.0006
	Mean	-0.0001	-0.0002	-0.0001	0.0000	0.0000	-0.0001
	Std	0.0059	0.0058	0.0013	0.0009	0.0009	0.0003
	Mean + std	0.0060	0.0060	0.0014	0.0009	0.0009	0.0004

Table 47 Absolute error on longitudinal strain for test 4

		Longitudinal					
		Reconstruction			Image registration		
		Green	Local	Global	Green	Local	Global
1	Max	0.0000	0.0000	0.0000	0.0000	0.0000	0.0000
	Mean	0.0000	0.0000	0.0000	0.0000	0.0000	0.0000
	Std	0.0000	0.0000	0.0000	0.0000	0.0000	0.0000
	Mean + std	0.0000	0.0000	0.0000	0.0000	0.0000	0.0000
2	Max	0.0198	0.0197	0.0040	0.0043	0.0043	0.0007
	Mean	0.0001	0.0001	0.0001	0.0000	0.0000	0.0000
	Std	0.0061	0.0061	0.0011	0.0013	0.0012	0.0002
	Mean + std	0.0062	0.0061	0.0012	0.0013	0.0012	0.0002
3	Max	0.0198	0.0197	0.0040	0.0043	0.0043	0.0007
	Mean	0.0001	0.0001	0.0001	0.0000	0.0000	0.0000
	Std	0.0061	0.0061	0.0011	0.0013	0.0012	0.0002
	Mean + std	0.0062	0.0061	0.0012	0.0013	0.0012	0.0002

Appendix C

1. Reconstruction and image registration

The following tables reports the results of the analysis on the Vessel geometry conducted with the manual reconstruction and image registration techniques. Four analyses were undertaken as listed in Table 48.

Table 48 Summary of the tests conducted on the Vessel geometry

Test	Geometry	Material	Simulation	Calibration	Element
1	B	2 (Chua)	c (120 mmHg.)	12	SOLID185
2	B	2	d (over)	12	SOLID185
3	B	3 (Wu)	c	12	SOLID185
4	B	3	d	12	SOLID185

As reported above, strains deriving from different sources were compared to determine the origins of the error on the strain measure. In the following tables the specific comparisons are marked with numbers referenced as:

- 1) ANSYS derived vs. ANSYS reported data;
- 2) ANSYS reported vs. test data;
- 3) ANSYS derived vs. test data.

For each object the circumferential and axial strains were derived and compared to quantify the error given by the technique.

Table 49 reports the absolute values of maximum, mean, standard deviation and scattering error on the circumferential and axial strains for test 1. In the same way Table 50 refers to test 2. Table 51 illustrates the results for test 3 and finally Table 52 is related to test 4. The scattering is calculated as the sum of mean and standard deviation error on the measurement.

Table 49 Absolute error on circumferential and axial strain for test 1

		Circumferential				Axial			
		Reconstruction		IR		Reconstruction		IR	
		Green	Local	Green	Local	Green	Local	Green	Local
1	Max	0.0004	0.0004	0.0004	0.0004	0.0000	0.0000	0.0000	0.0000
	Mean	0.0004	0.0004	0.0004	0.0004	0.0000	0.0000	0.0000	0.0000
	Std	0.0000	0.0000	0.0000	0.0000	0.0000	0.0000	0.0000	0.0000
	Mean + std	0.0004	0.0004	0.0004	0.0004	0.0000	0.0000	0.0000	0.0000
2	Max	0.0339	0.0339	0.0074	0.0105	0.0145	0.0149	0.0034	0.0033
	Mean	0.0013	0.0012	0.0012	0.0012	0.0000	0.0000	0.0001	0.0001
	Std	0.0090	0.0092	0.0034	0.0035	0.0055	0.0054	0.0012	0.0012
	Mean + std	0.0103	0.0105	0.0047	0.0047	0.0055	0.0054	0.0013	0.0013
3	Max	0.0335	0.0335	0.0070	0.0109	0.0145	0.0149	0.0034	0.0033
	Mean	0.0009	0.0008	0.0008	0.0008	0.0000	0.0000	0.0001	0.0001
	Std	0.0090	0.0092	0.0034	0.0035	0.0055	0.0054	0.0012	0.0012
	Mean + std	0.0099	0.0101	0.0043	0.0043	0.0055	0.0054	0.0013	0.0013

Table 50 Absolute error on circumferential and axial strain for test 2

		Circumferential				Axial			
		Reconstruction		IR		Reconstruction		IR	
		Green	Local	Green	Local	Green	Local	Green	Local
1	Max	0.0024	0.0024	0.0024	0.0024	0.0000	0.0000	0.0000	0.0000
	Mean	0.0024	0.0024	0.0024	0.0024	0.0000	0.0000	0.0000	0.0000
	Std	0.0000	0.0000	0.0000	0.0000	0.0000	0.0000	0.0000	0.0000
	Mean + std	0.0024	0.0024	0.0024	0.0024	0.0000	0.0000	0.0000	0.0000
2	Max	0.0344	0.0344	0.0160	0.0160	0.0163	0.0164	0.0038	0.0045
	Mean	0.0037	0.0037	0.0039	0.0040	0.0001	0.0001	0.0002	0.0002
	Std	0.0084	0.0083	0.0046	0.0046	0.0063	0.0061	0.0016	0.0016
	Mean + std	0.0121	0.0120	0.0085	0.0085	0.0064	0.0062	0.0019	0.0018
3	Max	0.0320	0.0320	0.0136	0.0136	0.0163	0.0164	0.0038	0.0045
	Mean	0.0013	0.0013	0.0015	0.0015	0.0001	0.0001	0.0002	0.0002
	Std	0.0084	0.0083	0.0046	0.0046	0.0063	0.0061	0.0016	0.0016
	Mean + std	0.0097	0.0096	0.0061	0.0061	0.0064	0.0062	0.0019	0.0018

Table 51 Absolute error on circumferential and axial strain for test 3

		Circumferential				Axial			
		Reconstruction		IR		Reconstruction		IR	
		Green	Local	Green	Local	Green	Local	Green	Local
1	Max	0.0040	0.0040	0.0040	0.0040	0.0000	0.0000	0.0000	0.0000
	Mean	-0.0040	-0.0040	-0.0040	-0.0040	0.0000	0.0000	0.0000	0.0000
	Std	0.0000	0.0000	0.0000	0.0000	0.0000	0.0000	0.0000	0.0000
	Mean + std	0.0040	0.0040	0.0040	0.0040	0.0000	0.0000	0.0000	0.0000
2	Max	0.0293	0.0293	0.0126	0.0126	0.0135	0.0135	0.0039	0.0039
	Mean	-0.0041	-0.0041	-0.0035	-0.0035	0.0000	0.0000	0.0002	0.0002
	Std	0.0082	0.0082	0.0037	0.0037	0.0061	0.0060	0.0013	0.0013
	Mean + std	0.0123	0.0123	0.0072	0.0072	0.0061	0.0060	0.0015	0.0014
3	Max	0.0245	0.0253	0.0081	0.0087	0.0135	0.0135	0.0039	0.0039
	Mean	-0.0002	-0.0002	0.0005	0.0005	0.0000	0.0000	0.0002	0.0002
	Std	0.0082	0.0082	0.0037	0.0037	0.0061	0.0060	0.0013	0.0013
	Mean + std	0.0084	0.0083	0.0042	0.0042	0.0061	0.0060	0.0015	0.0014

Table 52 Absolute error on circumferential and axial strain for test 4

		Circumferential				Axial			
		Reconstruction		IR		Reconstruction		IR	
		Green	Local	Green	Local	Green	Local	Green	Local
1	Max	0.0064	0.0064	0.0064	0.0064	0.0000	0.0000	0.0000	0.0000
	Mean	-0.0064	-0.0064	-0.0064	-0.0064	0.0000	0.0000	0.0000	0.0000
	Std	0.0000	0.0000	0.0000	0.0000	0.0000	0.0000	0.0000	0.0000
	Mean + std	0.0064	0.0064	0.0064	0.0064	0.0000	0.0000	0.0000	0.0000
2	Max	0.0263	0.0263	0.0177	0.0177	0.0186	0.0185	0.0046	0.0046
	Mean	-0.0054	-0.0054	-0.0049	-0.0049	0.0001	0.0001	0.0002	0.0002
	Std	0.0079	0.0078	0.0039	0.0038	0.0060	0.0060	0.0016	0.0015
	Mean + std	0.0133	0.0132	0.0088	0.0088	0.0061	0.0061	0.0018	0.0017
3	Max	0.0216	0.0216	0.0118	0.0118	0.0127	0.0185	0.0036	0.0046
	Mean	0.0010	0.0010	0.0015	0.0015	0.0001	0.0001	0.0002	0.0002
	Std	0.0079	0.0078	0.0039	0.0038	0.0060	0.0060	0.0016	0.0015
	Mean + std	0.0089	0.0088	0.0053	0.0053	0.0061	0.0061	0.0018	0.0017

Appendix D

1. Reconstruction and image registration

Table 54 summarises the results of the analysis on the Stented vessel geometry conducted with the manual reconstruction and image registration methods. One analysis was undertaken as listed in table X below.

Table 53 Protocol code

Geometry	Material	Simulation	Calibration	Element
C	3 (Wu)	f	12	SOLID185

As reported in the previous Appendices, strains obtained from different sources were compared to determine the origins of the error on the strain measure. In the table below the specific comparisons are marked with numbers referenced as:

- 1) ANSYS derived vs. ANSYS reported data;
- 2) ANSYS reported vs. test data;
- 3) ANSYS derived vs. test data.

For the stented vessel the circumferential and axial strains were derived and compared to quantify the error given by the reconstruction and image registration techniques. Table 54 reports the absolute values of maximum, mean, standard deviation and scattering error on the circumferential and axial strains for the test. The scattering is calculated as the sum of mean and standard deviation error on the measurement.

Table 54 Absolute error on circumferential and axial strain for Stented vessel test

		Circumferential				Axial			
		Reconstruction		IR		Reconstruction		IR	
		Green	LS	Green	LS	Green	LS	Green	LS
1	Max	0.0498	0.0498	0.0498	0.0498	0.0970	0.0657	0.0970	0.0657
	Mean	0.0049	0.0032	0.0049	0.0032	0.0037	0.0053	0.0037	0.0053
	Std	0.0100	0.0107	0.0100	0.0107	0.0132	0.0096	0.0132	0.0096
	Mean + std	0.0149	0.0139	0.0149	0.0139	0.0169	0.0148	0.0169	0.0148
2	Max	0.0795	0.0794	0.0629	0.0630	0.0873	0.0566	0.0872	0.0820
	Mean	0.0047	0.0028	0.0048	0.0032	0.0040	0.0054	0.0035	0.0051
	Std	0.0176	0.0184	0.0132	0.0143	0.0178	0.0148	0.0151	0.0117
	Mean + std	0.0222	0.0212	0.0180	0.0175	0.0218	0.0202	0.0186	0.0168
3	Max	0.0492	0.0491	0.0237	0.0238	0.0422	0.0421	0.0360	0.0364
	Mean	-0.0002	-0.0004	0.0000	0.0000	0.0003	0.0002	-0.0002	-0.0002
	Std	0.0141	0.0141	0.0082	0.0081	0.0122	0.0123	0.0080	0.0079
	Mean + std	0.0143	0.0145	0.0082	0.0081	0.0125	0.0124	0.0081	0.0081

Acknowledgements

We would like to thank Prof. Francesco Migliavacca who gave us the wonderful opportunity to spend a semester in Sheffield and to collaborate with a foreign university. Many thanks even for the careful supervision during the work.

We thank also Dr. Andrew James Narracott who introduced us to a different work environment with a different studying approach and provided us a large amount of new knowledge that will be useful in our future. Thanks for having followed us step by step during all these months with his precious suggestions. We are very grateful also for the accurate reviewing of the whole thesis in spite of his always busy schedule.

A special thank to the Medical Physics Group of the Department of Cardiovascular Science of The University of Sheffield, in particular to Prof. Patricia Lawford and Prof Rodney Hose, for the warm welcome from the very beginning and for having "adopted" other two noisy Italian girls.

To our colleagues Dave, Karen, Martin, Norman, Paul and Steve who made the launches in the canteen a bit less frustrating. To Des who entertained our rainy afternoons in the office with his hilarious Irish humor. To Angela, Angeliki, Anna, Chu-Hee, Claudia, Dani, Felix, Giovanna, Gloria, Iwona, Matteo and Susheel who have been not only work colleagues but also and mostly friends with whom sharing happy and sad moments. They made us discovered the beauties of travelling and meeting new amazing people.

Thanks to all the other friends and people we knew in Sheffield for having made our stay special and for all the nice memories.

Cheers

Francesca & Sandra

Ai miei genitori, che mi salutano col sorriso anche quando costa fatica.
A Franci, un infinito *thank you flower!*
A Letizia, la cui amicizia viaggia più veloce degli aerei e al di là dei mari.

Sandra

Grazie alla mia famiglia, ai miei genitori e a mia sorella Elisabetta che mi hanno sempre supportato e soprattutto sopportato, con la speranza che continuino a farlo.
Grazie ad Andrea, Chiara, Daniele, Fabio, Lele, Letizia, Paola, Paolo, Pino, Roberta, Roberto, Simone, Stefano e Valentina che non mi hanno fatto sentire la lontananza da casa.
Grazie alla grande famiglia dell'OM Sacconago, maschile e femminile, per aver rappresentato una valida alternativa allo studio nei weekend e durante la settimana.
Grazie ai compagni di università che hanno condiviso con me questi cinque anni di lezioni ed esami.
Last but not least grazie a Sandra, amica, compagna di studi e di avventure e ultimamente anche coinquilina. Grazie per il divertimento, le feste, le gite, le arrampicate, le camminate e le corse, grazie per non essersi mai stancata di ascoltare i miei lunghi monologhi e naturalmente per il sostegno nei momenti di difficili.

Francesca

Bibliography

- [1] V. Mallika, B.Goswami and M. Rajappa, "Atherosclerosis pathophysiology and the role of novel risk factors: a clinicobiochemical perspective," *Angiology*, vol. 58, pp. 513-522, 2007.
- [2] P. Serruys, M. Kutryk and A. Ong, "Coronary-Artery Stents," *The New England Journal of Medicine*, vol. 95, pp. 354-483, 2006.
- [3] P. Serruys, P. d. Jaegere, F. Kiemeneij, C. Macaya, W. Rutsch, G. Heyndrickx, H. Emanuelsson and J. e. Al., "A comparison of balloon-expandable-stent implantation with balloon angioplasty in patients with coronary artery disease. Benestent Study Group.," *The New England Journal of Medicine*, vol. 495, pp. 331-489, 1994.
- [4] C. Rogers and E. Edelman, "Endovascular stent design dictates experimental restenosis and thrombosis," *American Heart Association*, vol. 91, pp. 2995-3001, 1995.
- [5] C. Lally, F. Dolan and P. Prendergast, "Cardiovascular stent design and vessel stresses: a finite element analysis," *Journal of Biomechanics*, vol. 38, pp. 1574-1581, 2005.
- [6] F. Gijssen, F. Migliavacca, S.Schievano, L. Soggi, L. Petrini, A. Thury, J. Wentzel, A. v. d. Sten, P. Serruys and G.Dubini, "Simulation of stent deployment in a realistic human coronary artery," *BioMedical Engineering OnLine*, pp. 7-23, 2008.
- [7] F. Migliavacca, F. Gervaso, M. Prosi, P. Zunino, S. Minisini, L. Formaggia and G. Dubini, "Expansion and drug elution model of a coronary stent," *Computer Methods in Biomechanics and Biomedical Engineering*, vol. 10, pp. 63-73, 2007.
- [8] C. Rogers, D. Tseng, J. Squire and E. Edelman, "Balloon-artery interactions during stent placement: a finite element analysis approach to pressure, compliance and stent design as contributors to vascular injury," *Circulation Research*, vol. 84, pp. 378-383,

1999.

- [9] I. Zwierzak, J. Fenner and A. Narracott, "Strain measurement in an elastic material under large deformation using optical reconstruction methods," *IFMBE Proceedings*, vol. 36, pp. 120-123, 2011.
- [10] K. Goude, "An evaluation of stereoscopic strain measurement using virtual methods," *University of Sheffield, Medical School Cardiovascular department, Medical physics group*, 2012.
- [12] S. d. Chua and M. H. B.J. MacDonald, "FE simulation of slotted tube stent with the presence of plaque and artery by balloon expansion," *journal of Materials Processing Technology*, Vols. 155-156, pp. 1772-1779, 2004.
- [13] W. Wu, W. Wang, D. Yang and M.Qi, "Stent expansion in a curved vessel and their interactions: a FE analysis," *Journal of Biomechanics*, vol. 40, pp. 2580-2585, 2007.
- [14] E. Edelman and C. Rogers, "Pathobiologic responses to stenting," *American Journal of Cardiology*, vol. 7A, no. 81, pp. 4E-6E, 1998.
- [15] J. Carrozza, S. Hosley, D. Cohen and D. Baim, "In Vivo assessment of stent expansion and recoil in normal porcine coronary arteries: differential outcome by stent design," *Circulation*, vol. 100, pp. 756-760, 1999.
- [16] C. Schulz, R. Herrmann, C. Beilharz and J. Pasquantonio, "Coronary stent symmetry and vascular injury determine experimental restenosis," *Heart*, vol. 83, pp. 462-467, 2000.
- [17] S. Zhou, T. How, R. Black, S. Vallabhaneni, R. McWilliams and J. Brennan, "Measurement of pulsatile haemodynamic forces in a model of a bifurcated stent graft for abdominal aortic aneurysm repair," *Journal of Engineering in Medicine*, vol. 222, pp. 543-549, 2008.
- [18] H. Flora, B. Talei-Faz, L. Ansdell, E. chaloner, A. Sweeny, A. Grass and M. Adiseshiah, "Aneurysm wall stress and tendency to rupture are features of physical

- wall properties: an experimental study,” *Journal of Endovascular Therapy*, vol. 9, pp. 665-675, 2002.
- [19] Y. Wang, H. Yi and Z. Ni, “Experimental research on balloon-expandable endovascular stent expansion,” *Engineering in Medicine and Biology 27th Annual Conference*, pp. 2272-2275, 2006.
- [20] J. Orteu, “3-D computer vision in experimental mechanics,” *Optics and Laser in Engineerin*, vol. 47, pp. 282-291, 2009.
- [21] R. Koch, “3-D Surface reconstruction from stereoscopic image sequences,” *Computer Vision*, pp. 109-114, 1995.
- [22] T. Lujan, S. Lake, B. E. T.A. Plaizier and J. Weiss, “Simultaneous measurement of three dimensional joint kinematics and ligament strain with optical methods,” *Journal of biomechanical Engineering*, vol. 127, pp. 193-197, 2005.
- [23] Z. Gao, S. Pandya, N. Hosein, M. Sacks and N. Hwang, “Bioprosthetic heart valve leaflet motion monitored by dual camera stereo photogrammetry,” *journal of Biomechanics*, vol. 33, pp. 199-207, 200.
- [24] A. Narracott, D. Hore, P. Lawford and J. Gunn, “Measurement of symmetry of in vitro stent expansion: a stereophotogrammetric approach,” *Journal of Medical Engineering & Technology*, vol. 27, pp. 59-70, 2003.
- [25] M. Sutton, “Determination of displacements using an improved digital correlation method,” *Image and Vision Computing*, vol. 1, 1983.
- [26] B. Zitova and J. Flusser, “Image registration methods: a survey,” *Image and Vision Computing*, vol. 21, pp. 977-1000, 2003.
- [28] P. Lava, S. Coppieters, Y. Wang, P. V. Houtte and D. Debruyne, “Error estimation in a measuring strain fields with DIC on planar sheet metal specimens with a non-perpendicular camera alignment,” *Optics and Lasers in Engineering*, vol. 49, pp. 57-65, 2011.

- [31] A. Morton, N. Arnold, D. Crossman and J. Gunn, "Response of very small porcine coronary arteries to balloon angioplasty and stent implantation," *Heart*, vol. 90, pp. 324-327, 2004.
- [32] M. Garcia, "Technical Report, Hyperelastic material modeling," 2005.
- [33] P. Kelly, "Lecture Notes in Solid Mechanics. Part IV: material models in continuum solid mechanics," Department of Engineering Science, University of Auckland.
- [34] B. House and K. Nickels, "Increased automation in stereo camera calibration techniques," *Journal of Systemics Cybernetics and Informatics*, vol. 4, pp. 48-51, 2006.
- [35] J. Hughes, "Are static strains measured in phantom aneurysms in 3T MRI comparable to those measured optically?," *University of Leeds, Academic Unit of Medical Physics*, 2007.
- [36] D. Barber, "Sheffield Image Registration Toolkit (ShIRT) report," University of Sheffield.
- [37] K. Genovese, Y. Lee and J. Humphrey, "Novel optical system for in vitro quantification of full surface strain fields in small arteries: I. Theory and design," *Computer Methods in Biomechanics and Biomedical Engineering*, vol. 14, pp. 213-225, 2011.
- [39] B. Smith, M. Li and W. Tong, "Error assessment for strain mapping by digital image correlation," *Experimental Techniques*, vol. 22, pp. 19-21, 1998.
- [40] M. Sutton, X. Ke, S. Lessner, M. Goldbach, M. Yost, F. Zhao and H. Schreier, "Strain field measurements on mouse carotid arteries using microscopic three-dimensional digital image correlation," *Journal of Biomedical Materials Research Part A*, vol. 84A, pp. 178-190, 2008.